

Revealing hidden structures in the Zone of Avoidance – a blind MeerKAT H I Survey of the Vela Supercluster

Sambatriniaina H. A. Rajohnson¹, Renée C. Kraan-Korteweg¹, Bradley S. Frank^{2,3,4,1}, Hao Chen^{1,5}, Lister Staveley-Smith⁶, Paolo Serra⁷, Nadia Steyn^{1,6}, Sushma Kurapati¹, D. J. Pisano¹, Sharmila Goedhart^{4,8}

¹Department of Astronomy, University of Cape Town, Private Bag X3, Rondebosch 7701, South Africa

²UK Astronomy Technology Centre, Royal Observatory Edinburgh, Blackford Hill, Edinburgh EH9 3HJ, UK

³South African Radio Astronomy Observatory (SARAO), 2 Fir Street, Observatory, 7925, South Africa

⁴The Inter-University Institute for Data Intensive Astronomy (IDIA), and University of Cape Town, Private Bag X3, Rondebosch, 7701, South Africa

⁵Research Center for Intelligent Computing Platforms, Zhejiang Laboratory, Hangzhou 311100, China

⁶International Centre for Radio Astronomy Research (ICRAR), The University of Western Australia, 35 Stirling Highway, Australia

⁷INAF – Osservatorio Astronomico di Cagliari, Via della Scienza 5, 09047, Selargius, CA, Italy

⁸SKAO, 2 Fir Street, Black River Park, Second Floor, Block A, Cape Town, 7925

Accepted 2024 November 09. Received 2024 November 07; in original form 2024 September 07

ABSTRACT

We conducted the MeerKAT Vela Supercluster survey, named Vela–H I, to bridge the gap between the Vela SARAO MeerKAT Galactic Plane Survey (Vela–SMGPS, $-2^\circ \leq b \leq 1^\circ$), and optical and near-infrared spectroscopic observations of the Vela Supercluster (hereafter Vela–OPT/NIR) at $|b| \gtrsim 7^\circ$. Covering coordinates from $263^\circ \leq \ell \leq 284^\circ$ and $1^\circ \leq b \leq 6.2^\circ$ above, and $-6.7^\circ \leq b \leq -2^\circ$ below the Galactic Plane (GP), we sampled 667 fields spread across an area of ~ 242 deg 2 . With a beam size of $\sim 38'' \times 31''$, Vela–H I achieved a sensitivity of $\langle \text{rms} \rangle = 0.74$ mJy beam $^{-1}$ at 44.3 km s $^{-1}$ velocity resolution over ~ 67 hours of observations. We cataloged 719 galaxies, with only 211 (29%) previously documented in the literature, primarily through the HIZOA, 2MASX, and WISE databases. Among these known galaxies, only 66 had optical spectroscopic redshift information. We found marginal differences of less than one channel resolution for all galaxies in common between HIZOA and Vela–SMGPS, and a mean difference of 70 ± 15 km s $^{-1}$ between optical and H I velocities. Combining data from Vela–SMGPS, Vela–H I, and Vela–OPT/NIR confirmed the connection of the Hydra/Antlia filament across the GP and revealed a previously unknown diagonal wall at a heliocentric velocity range of 6500 – 8000 km s $^{-1}$. Vela–H I reinforces the connection between the first wall at 18500 – 20000 km s $^{-1}$ and the inner ZOA. The second wall seems to traverse the GP at $270^\circ \leq \ell \leq 279^\circ$, where it appears that both walls intersect, jointly covering the velocity range 18500 – 21500 km s $^{-1}$.

Key words: catalogues – surveys – cosmology: large-scale structure of Universe – galaxies: distances and redshifts – radio lines: galaxies

1 INTRODUCTION

The recently discovered Vela Supercluster (hereafter VSCL) is of particular interest among the large-scale structures (LSS) bisected by the ZOA because of its close alignment with the apex of the residual bulk flow, which is expected to originate from distances beyond $cz \geq 16000$ km s $^{-1}$ (Springob et al. 2016; Scrimgeour et al. 2016), and even outside 20000 km s $^{-1}$ ($200 h^{-1}$ Mpc, Carrick et al. 2015; Boubel et al. 2024). As part of a wide-area campaign aiming to explore LSS along the entire 360 $^\circ$ circle of the ZOA and learn more about the overall bulk flow, Kraan-Korteweg et al. 2017 (KK2017) pursued spectroscopic observations encompassing the region that contains the VSCL. The ~ 4200 new redshifts revealed it as an extended massive overdensity with multibranching filaments

(Einasto et al. 2011a). Its mass excess was estimated to contribute to ~ 50 km s $^{-1}$ to the motion of the Local Group (LG). However, optical (OPT) and near-infrared (NIR) data provide hardly any data that allow the detailed mapping of its overdensity and surmised walls because of dust obscuration and high star density at latitudes below $|b| < 5^\circ$. However, independent analyses using kinematic models have hinted at the presence of the dense core of VSCL deep within the ZOA (Sorce et al. 2017; Courtois et al. 2019).

The results of a first extensive exploration of the VSCL using H I data from the Vela-SARAO MeerKAT Galactic Plane survey (Vela–SMGPS) has proven to be highly successful (Rajohnson et al. 2024). The survey spans a region of 90 deg 2 along a 3 $^\circ$ latitude strip centered on $\ell \sim 275^\circ$. In total, 843 heavily obscured galaxies were identified. Following that project, we conducted a blind systematic interferometric survey referred to as the MeerKAT Vela Supercluster

* E-mail: aychasam@gmail.com

survey or Vela–H_I that will close the gap between Vela–SMGPS and OPT and NIR spectroscopic surveys. It covers an area of $263^\circ \leq \ell \leq 284^\circ$, $|b| \leq 6.7^\circ$, with its 667 pointings distributed both above and below the GP. The large survey area of $\sim 242 \text{ deg}^2$ aims to achieve the following three main objectives:

(i) To cover the area that bridges the gap between Vela–SMGPS (Rajohnson et al. 2024), and ancillary data in the more transparent surroundings at latitudes $|b| \gtrsim 7^\circ$, where data availability is less scarce. These OPT and NIR data include published data from KK2017 (AAOmega+2dF+SALT), along with additional redshift data provided by OPTOPUS and 6dF in the Hydra/Antlia region that remain unpublished (Kraan-Korteweg, priv. comm). These data will henceforth be referred to as the Vela–OPT/NIR dataset.

(ii) To combine the results obtained from Vela–H_I with those from Vela–SMGPS, encompassing various structures out to 25000 km s⁻¹, to get a better census of the missing part of the VSCL walls at higher latitudes of the ZOA and to obtain an improved view of the extent of the VSCL and its morphology.

(iii) In addition, the Vela–H_I will provide insight into nearby structures that were previously incompletely mapped or unknown.

The paper is organized as follows. We present the observing strategy of Vela–H_I in Section 2. Section 3 delves into the techniques and steps employed for H_I data processing, such as data reduction, mosaic generation, and source identification. The results are presented in Section 4, accompanied by an assessment of the reliability of the extracted H_I galaxies and a comparison of properties with cross-matched data from other surveys, both H_I or multi-wavelength data. In Section 5, we explore the alignment of the newly discovered galaxies with known LSS and analyze the identified structures in combination with the Vela–SMGPS detections and galaxies adjacent to the Vela–H_I survey region. A comprehensive summary of our findings is then provided in Section 6.

Throughout this work, all velocities are in the heliocentric optical convention ($V_{\text{hel}} = cz$). We adopt a standard cosmological model with $H_0 = 70 \text{ km s}^{-1} \text{ Mpc}^{-1}$, $\Omega_m = 0.3$, and $\Omega_\Lambda = 0.7$.

2 SURVEY DESIGN AND OBSERVATION STRATEGY

Vela–H_I was observed using the full MeerKAT array (Jonas & MeerKAT Team 2016) in eight sessions between August 15 and October 30, 2021 (MeerKAT Open-Time Proposal ID: SCI-20210212-SR-01). The observations were carried out with an array of 60 to 63 antennas using the 4k spectral line correlator mode in L-band (856 – 1712 MHz bandwidth), with visibilities recorded every 8 seconds. We used the coarse channel spacing of 209 kHz, which corresponds to a rest-frame velocity resolution of $\sim 44 \text{ km s}^{-1}$ at $z = 0$. This setup has been found to be sufficient for detecting and extracting H_I-signatures of normal spiral galaxies with typical linewidths of $w_{50} > 150 \text{ km s}^{-1}$ (see our results from the full SMGPS, Kurapati et al. 2024; Rajohnson et al. 2024; Steyn et al. 2024).

Vela–H_I covers two strips spanning approximately $\Delta l \times \Delta b \sim 21^\circ \times 6^\circ$ on either side of the GP. With the MeerKAT Primary Beam Full Width Half Maximum (FWHM) of $\sim 1.02^\circ$ at 1.4 GHz, the survey consists of 352 and 315 fields for the strips above and below the GP, respectively, as illustrated in Fig. 1. The area between $-2^\circ \leq b \leq 1^\circ$ was already surveyed by Vela–SMGPS. To ensure uniform sensitivity across the survey area, we used a Nyquist sampling configuration with a spacing of $r = 0.671^\circ$.

The observations were divided into 8 sessions, referred to as

‘blocks’, each having been observed between 7.6 to 9 hours. While the majority of the data collection occurred at night, some data in each block were observed during the day. The data captured during daylight hours were susceptible to solar radio-frequency interference (RFI) and required special flagging strategies (see Appendix A2).

The strip above the GP was observed in four blocks, denoted by suffix 1, with field prefixes ranging from A to D in increasing longitudes. Each block consists of 88 fields. The strip below the GP was observed in another set of four blocks, labeled with the suffix 2. These blocks contained 80 fields each, except for block D2 (lower left), which consisted of 75 fields. Within a block, each target field was visited twice during a cycle of observation, with each scan lasting 150 seconds. Bandpass and flux calibrators were observed for 3 minutes at the beginning, after the first cycle, and at the end of each run. Gain calibrators were observed for 2 minutes every 25 minutes, repeated in general after 10 fields had been observed. The complete survey was performed in approximately 56 hours of on-source time, with a total of 67.44 hours including overhead. Details of the observations for each block, listed in ascending order of the observed area, are provided in Table 1.

3 H_I DATA PROCESSING

We closely followed the strategy of Vela–SMGPS (Rajohnson et al. 2024) for data transfer, reduction procedures, software usage, imaging and H_I source finding. Modifications were tailored to suit the specific requirements of the Vela–H_I dataset, as detailed in the upcoming sections.

3.1 Data reduction

As in Vela–SMGPS, we only retrieved the frequency range of 1308 – 1430 MHz with their parallel-hand polarizations (XX, YY) for each observation from the SARAO archive¹ for transfer to the ILIFU cloud computing facility². This frequency range was selected for its flat, mostly RFI-free band, excluding bandpass roll-offs, and its high-redshift end corresponding to $z \approx 0.08$ ($cz \sim 25000 \text{ km s}^{-1}$) over the full extent of VSCL. The Containerised Automated Radio Astronomical Calibration CARACal (Józsa et al. 2020) was used for reducing the Vela–H_I observations. The pipeline that was executed on each dataset, involved several steps such as automatic flagging, cross-calibration, self-calibration, Doppler-tracking correction to the barycentric frame, continuum subtraction, imaging, and mosaicking. Unlike Vela–SMGPS, where a single ILIFU node processed a block, handling an entire block of 88 fields in Vela–H_I is computationally expensive, and will take weeks to complete. To speed up the process, we used ten nodes for parallel processing the data, each managing eight fields, reducing the processing time to around three to four days per block.

Following cross-calibration, the pipeline generated diagnostic plots of the calibrators and target using SHADEMS (Smirnov et al. 2022). This enabled a swift assessment of the quality of calibrated visibilities and helped identify any remaining RFI for flagging. We encountered two distinct issues during the inspection of cross-calibrated visibilities’ diagnostic plots: short-track bugs and solar interference (see Appendices A1 and A2, respectively). Despite setting SUNBLOCKER³ to TRUE during the imaging step, the latter issue

¹ <https://archive.sarao.ac.za/>

² www.ilifu.ac.za

³ <https://github.com/gigjozsa/sunblocker>

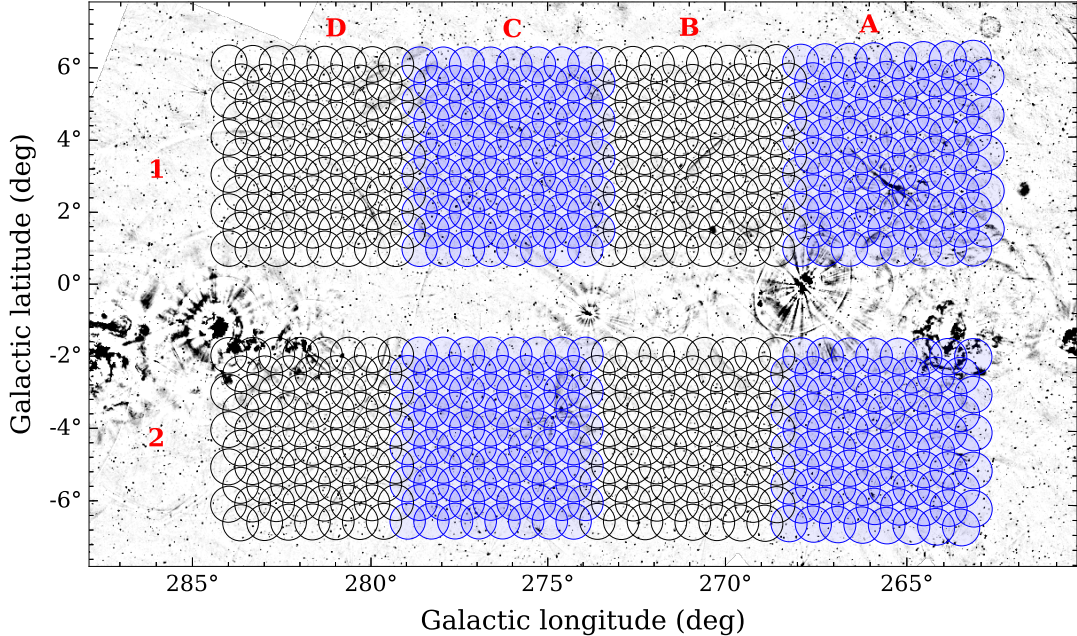


Figure 1. The 242 deg² area covered by the MeerKAT Vela Supercluster Survey, overlayed on a grayscale continuum map at 843 MHz from SUMSS (the Sydney University Molonglo Sky Survey, Bock et al. 1999). The 667 individual pointings are distributed into 8 observing blocks (A1, A2, B1, B2, C1, C2, D1, and D2) above and below the GP. The gap between the two sets of pointings has been covered by the Vela–SMGPS survey (Rajahson et al. 2024).

Table 1. Vela–H_I observing blocks overview

Obs Date (UT start)	Block ID	ℓ (deg)	b (deg)	Fields	Track (h)	N _{ant}	Primary calibrators (gaincal)	Secondary calibrators (fluxcal, bpcal, delaycal)	Notes
2021-08-22	1629602495 (A1)	$263^\circ \leq \ell \leq 269^\circ$	$1^\circ \leq b \leq 6.2^\circ$	88	8.88	61	J0828-3731	J0408-6545	a
2021-10-01	1633050310 (B1)	$269^\circ \leq \ell \leq 274^\circ$	$1^\circ \leq b \leq 6.2^\circ$	88	8.84	61	J0825-5010	J0408-6545	a
2021-10-30	1635552081 (C1)	$274^\circ \leq \ell \leq 279^\circ$	$1^\circ \leq b \leq 6.2^\circ$	88	8.93	61	J0825-5010	J0408-6545, J1939-6342	a
2021-09-04	1630723298 (D1)	$279^\circ \leq \ell \leq 284^\circ$	$1^\circ \leq b \leq 6.2^\circ$	88	8.94	61	J0825-5010, J0906-6829	J0408-6545, J1939-6342	a, b
2021-08-15	1628997934 (A2)	$263^\circ \leq \ell \leq 269^\circ$	$-6.7^\circ \leq b \leq -2^\circ$	80	8.11	60	J0828-3731	J0408-6545	a
2021-10-24	1635037887 (B2)	$269^\circ \leq \ell \leq 274^\circ$	$-6.7^\circ \leq b \leq -2^\circ$	80	8.06	63	J0825-5010	J0408-6545, J1939-6342	a
2021-10-02	1633134084 (C2)	$274^\circ \leq \ell \leq 279^\circ$	$-6.7^\circ \leq b \leq -2^\circ$	80	8.09	61	J0825-5010	J0408-6545	a
2021-09-12	1631417493 (D2)	$279^\circ \leq \ell \leq 284^\circ$	$-6.7^\circ \leq b \leq -2^\circ$	75	7.59	61	J0906-6829	J0408-6545	a, c

^a This data dataset is affected by the short track bug (see Appendix A1).

^b M039 (V-pol) shows dips in its power spectrum and will likely need to be flagged. During the last scan, the M058 data were flagged since it did not lock on target.

^c There was a wind stow event at the end of the observation.

persisted. This led us to incorporate an additional manual flagging step (see residual RFI flagging procedures in Appendix A) prior to the automatic flagging procedure in the pipeline, which however required a complete re-run of the reduction process.

3.2 Imaging and mosaicking

We employed WSCLEAN for imaging, with a pixel size of 3'', Briggs $r = 0$, and a UV-taper of 15''. This produced a total of 667 H_I cubes, each composed of 570 channels (ranging from 1309 MHz to 1428.49 MHz), with a width of 210 kHz after Doppler correction. This setup was made to ensure that the cubes have the same zero-point velocity as those for Vela–SMGPS, corresponding to a rest-frame velocity resolution of 44.3 km s⁻¹ at $z = 0$ and 46.9 km s⁻¹ at the VSCL distance (i.e., $cz \sim 18000$ km s⁻¹). After some adjustments, including primary beam (PB) correction and resizing the radii of the H_I cubes to a normalized PB sensitivity cut-off of 0.2 (equivalent to 0.8°), the partially overlapping H_I cubes were prepared for mosaicking.

The H_I cubes were extracted per pointing. The eight observing blocks of 80 to 88 cubes, were divided into four mosaics labeled A to D. Above the GP, mosaics were constructed of 27 contiguous H_I cubes. For the blocks below the GP, the initial two mosaics (with suffixes A and B) were composed of 22 cubes, while the remaining two (C and D) contained 27 cubes each. This arrangement resulted in an on-sky coverage of approximately 3.5° × 4° or 3.5° × 3.5° per mosaic, with an overlap of $\Delta\ell = \Delta b \sim 1.5^\circ$ (except $\Delta\ell \sim 2^\circ$ for D2) for mosaics within the same block, and $\Delta\ell \sim 0.75^\circ$ overlap between two mosaics from two adjacent blocks. These overlapping regions were essential for capturing extended sources that might be detected at the edge of the mosaic and were used at the same time for conducting an internal data quality assessment based on the properties of detected galaxies in these regions (see Section 4.2). The overall mosaic layout is illustrated in Fig. 2.

In total, 32 mosaics were produced, comprising 16 consecutive ones above and below the GP, respectively. These mosaics were

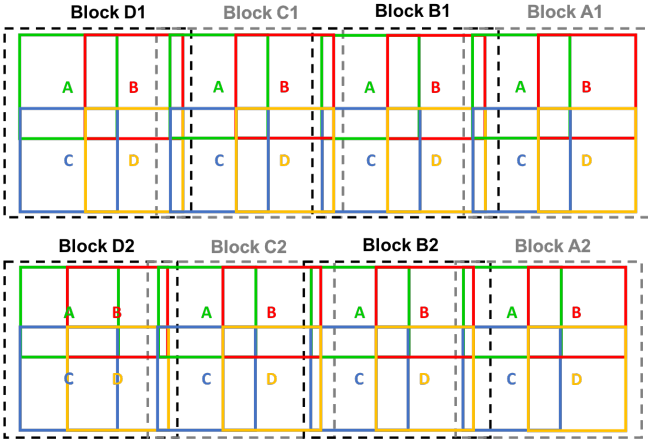


Figure 2. Mosaicking configuration of Vela–HI. Each block, indicated by black or grey dashed rectangles, is subdivided into four partially overlapping tiles labeled A to D.

generated from individual fields with rms values ranging from 0.88 to 2.57 mJy beam $^{-1}$. The Nyquist sampling setup of the survey has provided us with a nearly uniform central region covering approximately $3^\circ \times 3.5^\circ$ and $3^\circ \times 3^\circ$ (utilized for source finding regions). Additionally, it also facilitated a twofold increase in sensitivity after mosaicking compared to an individual field, as illustrated in Fig. A4 of Appendix A. The figure showcases three subfigures presenting the rms variations per field before solar RFI removal, after solar RFI removal, and after mosaicking, respectively.

The spectral baselines of the central regions of the mosaics generally remain flat with rms noise ranging from 0.68 to 1.24 mJy beam $^{-1}$, as displayed in Fig. 3. Only for a few cases do we observe increased noise levels towards the edge of the mosaic’s spectral axis ($cz > 24000 \text{ km s}^{-1}$). Additionally, residual RFI spikes from Global Positioning Satellites (GPS), i.e., around 1375–1387 MHz ($\sim 8500 \text{ km s}^{-1}$) appear in only 9 out of 32 mosaics. This leaves a nearly uniform noise variation with no significant noise peaks when considering the remaining 23 mosaics, indicating that RFI has minimal effects on the data, which will not impact the interpretation of LSS in Section 5. We excluded the high-noise region from mosaic A2B from the subsequent assessment and analysis of the survey. This region shows nearly double the noise compared to other mosaics (see the brown line in Fig. 3) which may be due to the presence of the Vela Supernova remnant ($\ell \sim 263.93^\circ$, $b \sim -3.36^\circ$, Green 2009). Exclusion of the A2B mosaic results in an average noise value of 0.74 mJy beam $^{-1}$ for the Vela–HI survey. For a source detected at 5σ and with 200 km s^{-1} linewidth, this translates to an HI mass limit of $5 \times 10^9 \text{ M}_\odot$ and $7.1 \times 10^9 \text{ M}_\odot$ at $cz \sim 17500 \text{ km s}^{-1}$ (Wall 1) and $\sim 21000 \text{ km s}^{-1}$ (Wall 2), respectively.

The mosaic beam size is determined as the median value from the individual beams of each input cube. Compared to this median mosaic beam area, we observe a scatter of approximately 11% in the beam areas per channel and per cube. An average beam size of $38'' \times 31''$ is derived for Vela–HI, slightly larger than for SMGPs. This corresponds to a spatial resolution of about $47 \times 39 \text{ kpc}$ at the VSCL distance ($cz \sim 18000 \text{ km s}^{-1}$), adequate for our scientific objectives. For comparison, the mosaicking parameters for the two systematic HI surveys, Vela–SMGPs and Vela–HI, are provided in Table 2.

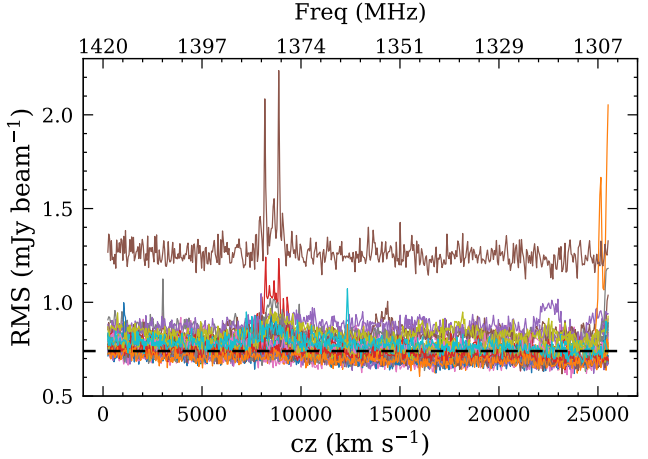


Figure 3. Rms versus velocity in km s^{-1} as measured through the centers of the 32 mosaics. Interference from Global Positioning Satellites can be seen in the frequency band 1375–1387 MHz ($\sim 8500 \text{ km s}^{-1}$). The average rms noise of $0.74 \text{ mJy beam}^{-1}$ is shown by the horizontal dashed lines when excluding the high noise from the mosaic A2B (brown line), which is considerably higher than other mosaics and shows stronger fluctuations as well.

Table 2. Survey parameters’ comparison of Vela–HI and Vela–SMGPs

Parameter	Vela–HI	Vela–SMGPs
Date of observations	Aug – Oct 2021	Dec 2018 – Nov 2019
Sky coverage	$\sim 242 \text{ deg}^2$	$\sim 90 \text{ deg}^2$
Effective area (ℓ)	$263^\circ \leq \ell \leq 284^\circ$	$260^\circ \leq \ell \leq 290^\circ$
Effective area (b)	$1^\circ \leq b \leq 6.2^\circ$, $-6.7^\circ \leq b \leq -2^\circ$	$-2^\circ \leq b \leq 1^\circ$
Number of Mosaics	32	10
Integration time ^a	$\sim 300 \text{ s}$	$\sim 3600 \text{ s}$
Velocity resolution ^b	44.3 km s^{-1}	44.3 km s^{-1}
Velocity range ^c	$< 25000 \text{ km s}^{-1}$	$< 25000 \text{ km s}^{-1}$
Beam size	$38'' \times 31'' (\pm 3'')$	$30'' \times 26'' (\pm 1'')$
Measured rms	$0.68\text{--}1.24 \text{ mJy beam}^{-1}$	$0.29\text{--}0.56 \text{ mJy beam}^{-1}$
Mean rms	$0.74 \text{ mJy beam}^{-1}$	$0.39 \text{ mJy beam}^{-1}$

^a Integration time per pointing. ^b at $z = 0$.

^c HI source finding velocity range .

3.3 HI detections

In large surveys like Vela–HI, visually identifying sources becomes impractical due to the size of each mosaic, approximately 55 GB with $\sim 5150 \text{ pix} \times 5000 \text{ pix} \times 526 \text{ chans}$ voxels. Applying automated source-finding methods is therefore crucial. Following the approach used in Vela–SMGPs, we employed the SoFiA-2 algorithm (Serra et al. 2015; Westmeier et al. 2021) to search for HI sources. This process was applied to all mosaics for the velocity range $250 < cz < 25000 \text{ km s}^{-1}$. Two different source-finding regions were defined. The first box encompasses $3600 \text{ pix} \times 4200 \text{ pix} \times 517 \text{ chans}$ ($\sim 3.5^\circ \times 3^\circ$) for the mosaics above the GP and half of the mosaics below the GP. For the remaining half below the GP, we defined mosaics of $3600 \text{ pix} \times 3600 \text{ pix} \times 517 \text{ chans}$ ($\sim 3^\circ \times 3^\circ$). The source-finding regions are outlined by white rectangles in Fig. 4, and defined to maximize sensitivity in the central part while avoiding lower sensitivity at the edges of the mosaics. Some overlap between adjacent mosaics is ensured.

Apart from noise normalization through the weighting by noise cubes, we performed an additional continuum subtraction step using a polynomial of order $n = 1$ with a threshold of 2σ to eliminate

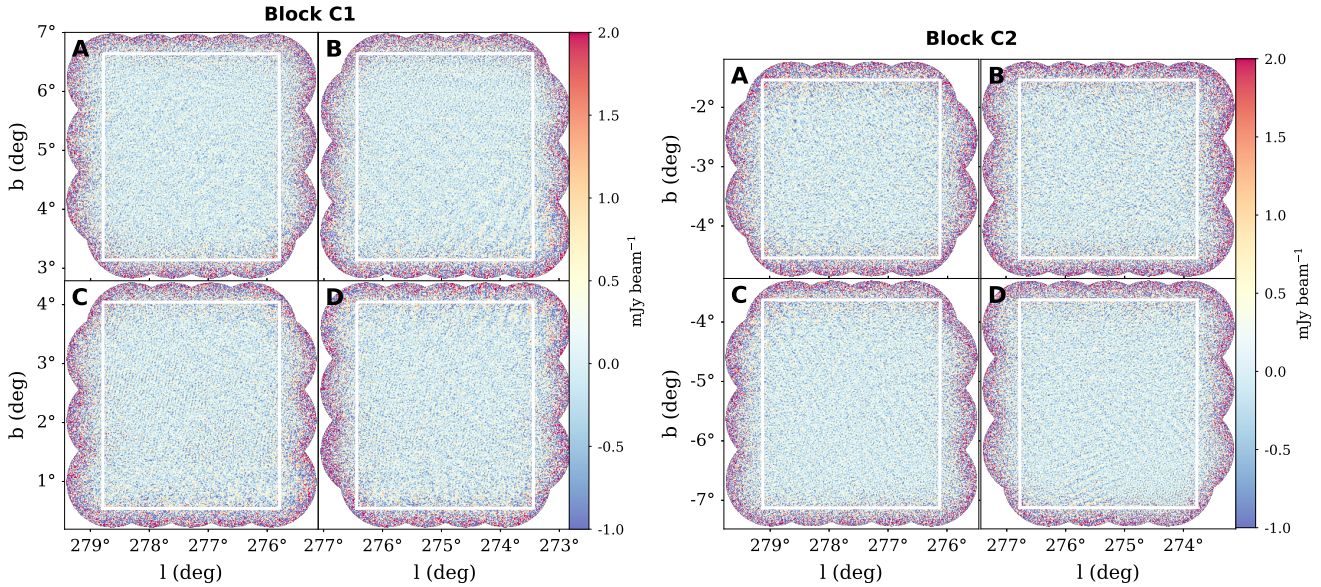


Figure 4. Example of source finding regions for the different mosaic configurations. The top panel illustrates regions of $\sim 3.5^\circ \times 3^\circ$ for a block of four mosaics located above the GP (e.g., block C1). The bottom panel shows two mosaics with $\sim 3^\circ \times 3^\circ$ regions (top), and the other two with $\sim 3.5^\circ \times 3^\circ$ (bottom) for a block located below the GP (e.g., block C2). The white rectangles outline the source finding regions.

residual low-level continuum emission. Subsequently, we applied SoFiA’s default source-finding algorithm ‘Smooth and Clip (S+C)’. In comparison to Vela–SMGPS, we introduced two additional spatial smoothing kernels of 20 and 30 pixels, equivalent to $60''$ and $90''$ angular resolution smoothing, to account for the larger beam size in our survey. However, the spectral kernels and the two-run thresholds of 3.5 and 4σ remained consistent with Vela–SMGPS. We then merged all detected pixels with a minimum linking size of 14 pixels (slightly larger than one beam) to obtain coherent sources.

For source validation, each SoFiA run produced a catalog of detected sources, including both genuine detections and false positives. To ensure accuracy, three team members independently adjudicated the sources. Each team member carefully reviewed each potential H_I source in the catalog by visually inspecting their moment maps and global H_I profiles. A ‘solid’ detection shows a clearly defined H_I disc in the mom-0 maps, clear rotation across two or more channels in the mom-1 maps, and a distinct peak over a flat baseline in the spectrum. Detections are classified as ‘possible’ if they meet some, but not all, of these criteria; for example, if they exhibit a low-velocity gradient or lack clear emission due to wiggly baselines. Additionally, faint sources smaller than 1.5 times the beam size with a signal-to-noise ratio (SNR) ≤ 6 were conservatively classified as ‘possible’. Sources that did not meet these criteria, such as those with rotation over more than 20 channels or high-redshift dwarfs, were removed from the catalog. Additional details on this adjudication process can be found in Rajohnson et al. (2024). The final results of the panels describing the source (i.e., mom-0, mom-1, global H_I profile) are presented in a galaxy atlas available in the following Zenodo repository: <https://doi.org/10.5281/zenodo.12522807>.

For source parameterization, SoFiA automatically generates H_I parameters in default units of the mosaic, including the central position in Galactic coordinates, central frequencies in Hz, integrated fluxes in Jy Hz, and linewidths in Hz. We applied the rest-frame velocity convention, which was the necessary conversion to obtain the systemic heliocentric velocity in km s⁻¹, integrated flux in Jy km s⁻¹, and linewidths in km s⁻¹, enabling us to derive the H_I masses. The

uncertainties in the fluxes were calculated by averaging the standard deviations of the integrated fluxes measured from four emission-free regions, each the same size as the source mask and located around the H_I source. For full details of the parameterization and error estimation, please refer to Section 3.3 of Rajohnson et al. (2024).

4 RESULTS

We identified a total of 719 H_I sources. The complete catalog, along with their derived H_I parameters, is available in Table B1 of Appendix B. In this section, we present the findings and comparative assessment of H_I sources in the Vela–H_I survey. This includes their overall distributions on a wedge diagram, an evaluation of the quality of H_I data, and a comparative analysis of parameters with prior H_I surveys in the ZOA. Furthermore, we conclude with a search for multi-wavelength counterparts and an examination of the H_I properties distribution in Vela–H_I.

4.1 General redshift wedge

Among the 719 detections, 432 galaxies are detected above the GP, while 287 are situated below. Their distribution in latitude (left) and longitude (right) redshift slice diagrams across the full velocity range of the Vela–H_I ($cz < 24000$ km s⁻¹) is illustrated in Fig. 5 where dark blue points indicate those above the GP and cyan triangles those below the GP. There are clear overdensities and distinct structures apparent in both panels. For instance, in the longitude wedge diagram, some structures are prominent only below the GP (e.g., cyan triangles at ~ 10000 km s⁻¹), while others overlap, suggestive of potential connections across the ZOA (e.g., at ~ 8000 km s⁻¹). Further details regarding the LSS observed in the wedges will be discussed in Section 5.

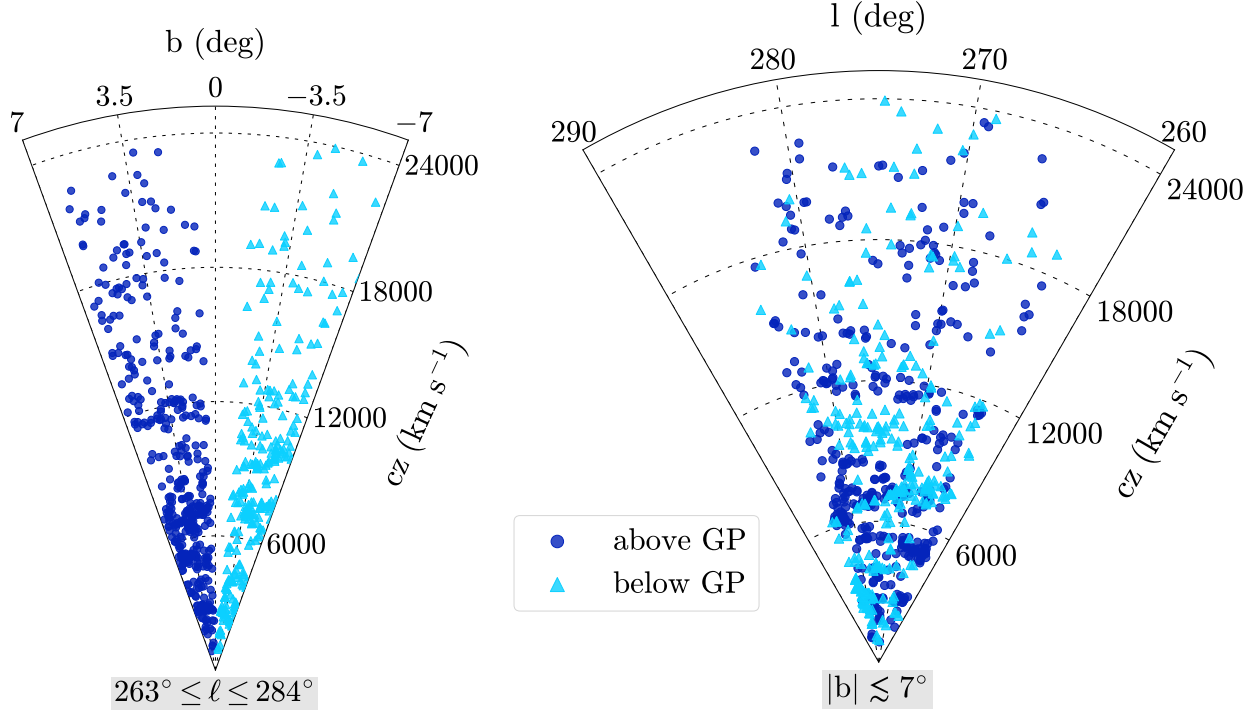


Figure 5. Latitude and longitude redshift wedge plots of detected galaxies in Vela–HI represented by dark blue dots for those above the GP and cyan triangles for those below.

4.2 Internal quality assessment

Thanks to the presence of overlapping regions within the mosaics described in Section 3.2, we conducted an independent assessment of the H_I data quality. A total of 163 detections were found in one or more adjacent mosaics. The heliocentric velocities and 50% linewidths of these sources exhibited only small median differences of $6.5 \pm 9.9 \text{ km s}^{-1}$ and $11.8 \pm 30.2 \text{ km s}^{-1}$, respectively, measuring less than half a channel width ($\Delta v = 44.3 \text{ km s}^{-1}$ at $z = 0$). The median integrated flux difference was found to be $0.3 \pm 0.8 \text{ Jy km s}^{-1}$, lower in most cases than the integrated flux errors of the individual detections. The high level of consistency in the H_I parameters from overlapping regions confirms the robustness of the derivation of these properties.

We also used the duplicates to assess the positional accuracy of the survey. In Fig. 6, the respective offsets are displayed. By measuring the differences in Galactic coordinates of each duplicate, we achieved an average coordinate precision of $6.04''$, with a 1σ standard deviation of $7.23''$. This value is close to three times larger than that of Vela–SMGPs, which can be attributed to the larger beam size of Vela–HI. We did not distinguish between solid and possible detections as only two of the duplicates are classified as possible detections. The estimate of positional accuracy is an important parameter in our search for multi-wavelength counterparts (see Section 4.4).

4.3 Comparison with other H_I surveys

We now explore any potential systematics in the measured H_I parameters of our survey compared to other H_I surveys that have some overlapping footprint with Vela–HI, such as HIZOA and the Vela–SMGPs.

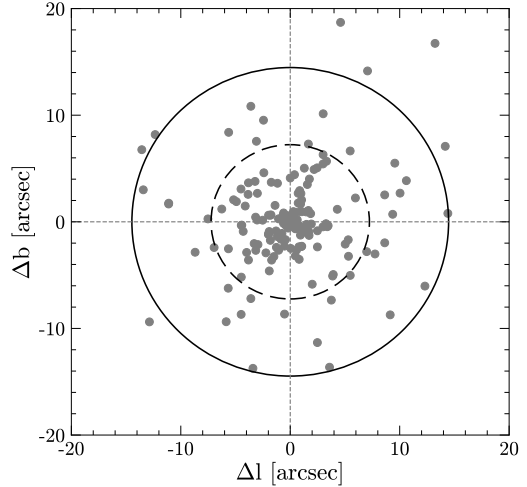


Figure 6. Galactic coordinates separations between Vela–HI detections found in the overlapping regions of the mosaics. The black dashed and solid circles mark the 1σ and 2σ of the coordinate separations.

4.3.1 Comparison with Vela–SMGPs

In comparing Vela–HI with Vela–SMGPs, we identified 15 galaxies in common that have separations below $10''$ and velocity offsets limited to 75 km s^{-1} . The mean separation of these counterparts was $5.4'' \pm 2.7''$, well within the coordinate precisions of both surveys. However, 3 of these detections were situated in strong continuum regions at the edge of Vela–HI, and 6 others had very low integrated signal-to-noise ratio ($\text{SNR} < 6$) in Vela–HI, making their fluxes unreliable for comparison. We therefore limited our comparison to the remaining 6 galaxies with $\text{SNR} > 9$.

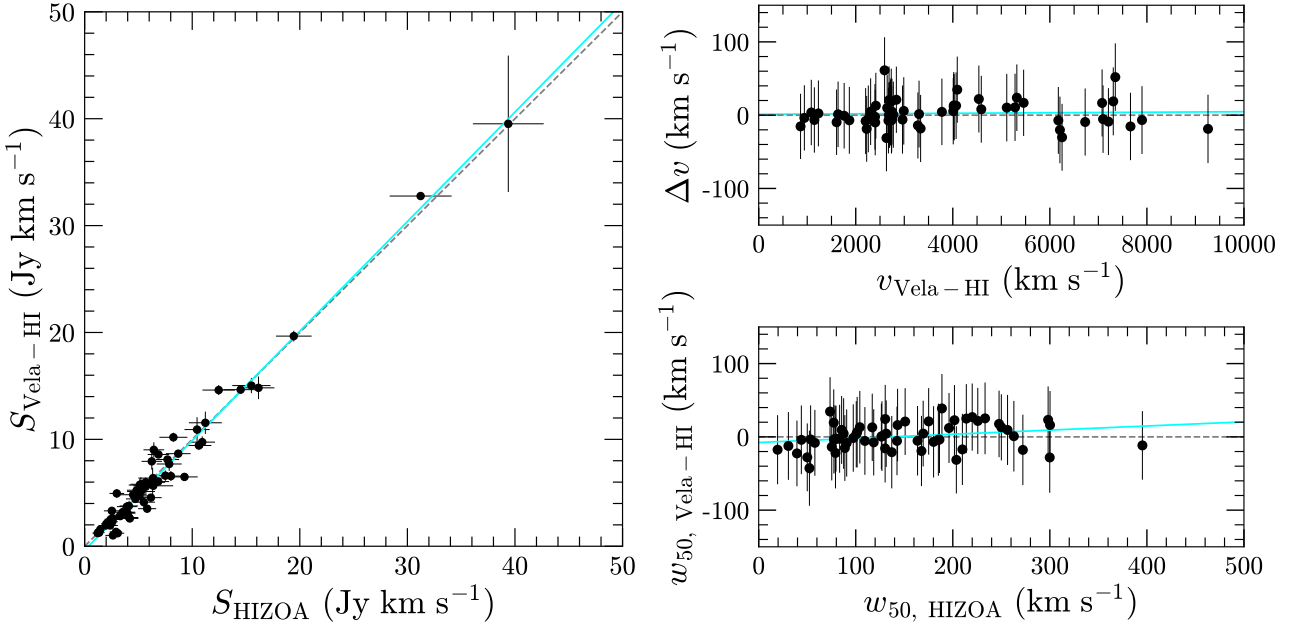


Figure 7. In the left panel, the integrated fluxes of Vela–H_I detections with known counterparts from HIZOA are compared. The one-to-one relation is represented by the black dashed line, and the best linear fit is indicated by the cyan solid line. In the right panels, the differences in systemic velocities (top panel) and H_I linewidth (bottom panel) between Vela–H_I and HIZOA are illustrated. The cyan lines in both panels depict the outcomes of the best-fit linear regressions, with the dashed black zero-difference line serving as a reference for comparison.

Upon examining differences in velocities c_z , and linewidths w_{50} , we noted that Vela–H_I galaxies exhibit slightly higher velocities compared to those in Vela–SMGPS, showing an offset of 9.6 ± 5.1 km s\$^{-1}\$ and 9.1 ± 5.7 km s\$^{-1}\$ in linewidth, respectively. The systemic velocity difference slightly increases with redshift, while the linewidth difference is smaller for larger linewidths, except for cases with low SNR and large w_{50} , where the emission peaks are easily hidden by noise. Despite these variations, all values fall within the one-channel resolution of both surveys and lie within the expected error margin.

In terms of fluxes, the linear regression fit found for the 6 galaxies in common follows a near one-to-one relation with a slope of 0.982 ± 0.298 , an intercept of -0.886 ± 1.938 , and an R^2 value of 0.93. No statistically significant (3σ) systematic effects are noticeable for this small sample of galaxies with high SNR.

To further assess the reliability and completeness of our survey, we investigated the Vela–H_I detections not found in Vela–SMGPS, and vice versa. The three Vela–H_I galaxies not cataloged in Vela–SMGPS had a low SNR < 5 with a Flag of 2 (i.e., they were designated as possible detections). They were all positioned at the noisy edge of the Vela–SMGPS mosaics which could have led to them being missed by SoFiA.

Conversely, 49 Vela–SMGPS galaxies (28 above and 21 below the GP) were not detected by Vela–H_I. This is not surprising given the higher sensitivity of Vela–SMGPS, with a mean rms of 0.39 mJy beam\$^{-1}\$ compared to 0.74 mJy beam\$^{-1}\$. Galaxies undetected in Vela–H_I revealed a median SNR of 8, median integrated fluxes of 0.45 Jy km s\$^{-1}\$, median velocities around 11500 km s\$^{-1}\$, and a median w_{50} of 145 km s\$^{-1}\$ in Vela–SMGPS. Those with SNR > 8 but undetected in Vela–H_I typically had local rms values below the average noise, indicating they were close to the detection limit threshold and located in low rms areas of Vela–SMGPS, hence too faint for

our survey. Only galaxies with high SNR and relatively nearby were therefore likely to be detected in common by both surveys.

4.3.2 Comparison with HIZOA

We identified 87 HIZOA detections out of the 90 present within our surveyed area. Three sources – J0932-44, J0916-55, and J0933-58 – remained undetected. The absence of J0932-44 and J0916-55 in our Vela–H_I data can be attributed to their narrow w_{50} linewidths in HIZOA (87 and 140 km s\$^{-1}\$, respectively). No w_{20} information is also available in the HIZOA catalog, which could be part of the reason why they were overlooked given our coarse resolution. As for J0933-58, it was not recovered by SoFiA, likely due to (i) its location in an area strongly affected by residual solar RFI and (ii) its proximity to the edge of the source-finding region. Among the 87 HIZOA detections, 5 were resolved into multiple counterparts in the Vela–H_I survey. These sources resolved into several counterparts were excluded from the comparison. To ensure a robust comparison, we also excluded sources with a low SNR (SNR < 10) in Vela–H_I, and those affected by residual solar RFI, leading to poor baselines. This filtering process led to 61 galaxies for comparison.

The remaining detections displayed a mean coordinate precision of $1.9' \pm 1.6'$. The flux fit regression, illustrated in Fig. 7, reveals a slope close to unity (1.024 ± 0.042), an intercept of -0.358 ± 0.405 , with $R^2 = 0.98$. The right panels of Fig. 7 display the differences in systemic velocities and linewidths. The systemic velocity plot (top right panel) yields a mean absolute difference of $\Delta v \sim 12.2$ km s\$^{-1}\$ with a standard deviation of 11.1 km s\$^{-1}\$, which is insignificant given the errors. The linewidth difference (bottom right panel) has a slight offset of 13.2 ± 10.3 km s\$^{-1}\$. Given that linewidths have been corrected for instrumental resolution, and the coarse resolution (~ 44 km s\$^{-1}\$), neither this offset nor the trend (cyan line) is significant. The linewidths compared to HIZOA are consistent with each other;

on a one-to-one basis, we find a slope close to unity (1.009 ± 0.058) and an intercept of -0.836 ± 9.682 , with $R^2 = 0.95$.

4.4 Multi-wavelength counterparts

The Vela-HI survey uniquely connects the Vela-SMGPS to the higher latitudes where deep optical and NIR surveys like Vela-OPT/NIR, 2MRS, etc., become successful in unveiling LSS. Compared to SMGPS, this increases the likelihood of finding multi-wavelength counterparts.

We initiated a comprehensive search for multi-wavelength counterparts for our Vela-HI detections using online databases such as the NASA/IPAC Extragalactic Database (NED)⁴ and the Vizier Catalogue access tool (Ochsenbein et al. 2000). Data retrieval (e.g., tables) employed remote web querying forms facilitated by the Python module Astroquery (Ginsburg et al. 2019). The search radii were determined by the quadrature of the positional accuracy of the two cross-matched surveys. For instance, the search radius for HI surveys like HIPASS (Meyer et al. 2004) and HIZOA (Staveley-Smith et al. 2016) typically spans a few arcminutes, while OPT and NIR catalogs have accuracies of a few arcseconds (e.g., 2MASX, has a positional accuracy of approximately 1'', as detailed in Jarrett et al. 2000). There can also be offsets between the center of stellar and neutral hydrogen structures of a galaxy. We therefore applied a search radius of 15'', considering the positional accuracy of Vela-HI of $\sim 6''$, and took into account sources classified as ‘G’ or Galaxy in NED for star-galaxy separation. This approach resulted in a list of potential counterparts and redshifts where available. To assist in identifying the most likely counterpart, an examination of a $2' \times 2'$ image stamp from the Digitized Sky Survey (DSS), 2MASS-K band, and WISE-1 band ($3.4 \mu\text{m}$) was examined (using SKYVIEW, a package in ASTROQUERY).

Figure 8 illustrates the distribution of Vela-HI detections and their potential multi-wavelength counterparts. Those with available optical spectroscopic redshifts are marked as red diamonds and those without redshift data with blue open squares. Below $|b| \lesssim 5^\circ$, the availability of redshift information diminishes due to increasing foreground extinction. This is shown by the extinction contour in grey representing the dust extinction limit in the optical of $A_B \simeq 3.0$ mag, derived from the Diffuse Infrared Background Experiment (DIRBE) maps (Schlegel et al. 1998; Schlafly & Finkbeiner 2011; Schröder et al. 2021). Out of the 719 HI detections, we identified 211 (~29%) probable counterparts. Their mean separation is minimal, measuring only $5.6'' \pm 3.4''$, less than the positional accuracy of Vela-HI. 110 galaxies (~52% of 211) have redshift information, with 66 (~31% of 211) originating from optical spectroscopy, and 27 (~13% of 211) having HI redshifts only (HIZOA and HIPASS). Photometric redshifts were not used for comparison given their huge uncertainties. For Vela-HI galaxies with velocities exceeding 16000 km s^{-1} , i.e., at the VSCL distance, 19 have likely counterparts, but only 5 have available spectroscopic redshift data.

The histograms in Fig. 9 compare the distribution in velocity and HI mass for the Vela-HI detections (light-blue with dotted patterns) with their likely counterparts (hatched blue). Counterparts with spectroscopic redshift information are depicted in red. In the left panels, we observe a decrease in the number of counterparts as velocities

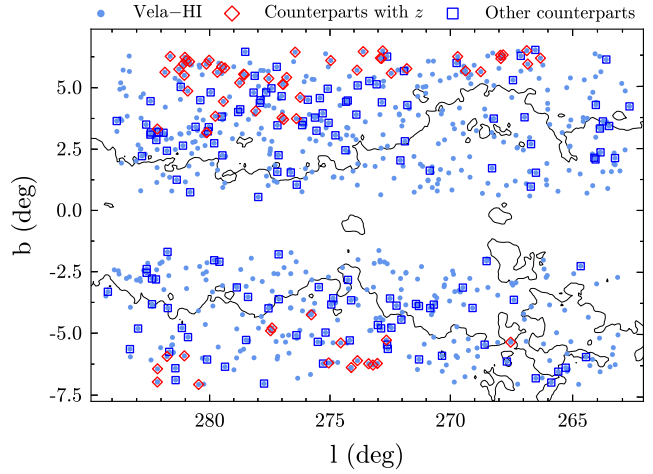


Figure 8. On-sky distribution of Vela-HI detections (light blue dots). Red open diamond symbols represent multi-wavelength counterparts with spectroscopic redshifts, while blue open squares have no redshift information. Black contour lines delimit the Galactic foreground extinction at $A_B \simeq 3.0$ mag.

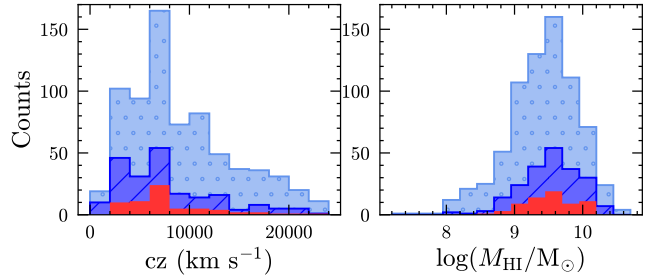


Figure 9. Histograms comparing Vela-HI detections (light-blue with dotted patterns) and their likely counterparts as a function of velocity (left panel) and HI mass (right panel). Galaxies with counterparts are depicted by the blue-hatched histograms, and counterparts with spectroscopic redshifts are represented by red-shaded histograms.

increase. The peaks in counterpart distributions align with overdensities in Vela-HI (see Section 5.2). In the right panel, galaxies with low HI masses $\log(M_{\text{HI}} / M_\odot) < 8.4$ have few matches. They are likely blue low surface brightness dwarfs, therefore difficult to see through extinction layers. There is a slight increase in the number of cross-identified HI detections with increasing HI masses, which are generally large spirals that are prominent in optical as well. They peak at the same point as the HI mass distributions of Vela-HI. The results from Figs. 8 and 9 suggest that the likelihood of an HI source having a potential counterpart increases with HI mass but decreases as foreground extinction rises at lower latitudes. Moreover, there are no systematic surveys in the ZOA that cover higher redshifts. The only systematic survey is 2MASS, but it is also incomplete with increasing redshift, brightness-limited, and affected mostly by stellar crowding at lower latitudes, making massive and nearby galaxies likely to have more counterparts than dwarfs and high- z galaxies.

We will now investigate the correspondence between spectroscopic and HI redshifts. A one-to-one comparison results in a slope close to unity (0.997 ± 0.004) with an $R^2 = 0.999$ and an intercept of 17.7 ± 36.2 . These findings demonstrate a high level of consistency. A more detailed analysis, examining the difference between HI and optical velocities ($\Delta v = v_{\text{Vela-HI}} - v_{\text{opt}}$) as illustrated in Fig. 10

⁴ <http://ned.ipac.caltech.edu>

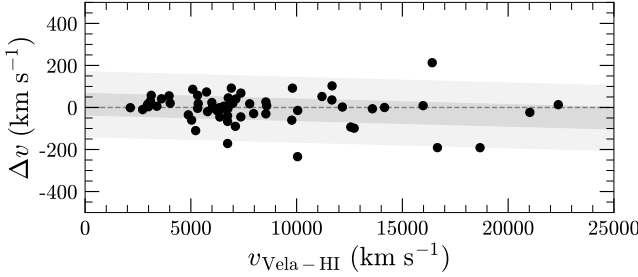


Figure 10. Heliocentric optical velocity comparison between Vela–H_I galaxies and counterparts with spectroscopic redshifts ($\Delta v = v_{\text{Vela–HI}} - v_{\text{OPT/NIR}}$). The dark-shaded regions delineate the 1σ and 3σ standard deviations, respectively.

reveals an average difference of $70 \pm 51 \text{ km s}^{-1}$. The best-fitting parameters of the velocity differences have a slope and intercept of -0.003 ± 0.004 and 15.6 ± 36.4 , respectively, showing no significant difference with increasing velocities. In Section 4.3.2, the comparison with HIZOA of the Vela–H_I velocities found uncertainties to be of the order of $13.2 \pm 10.3 \text{ km s}^{-1}$. Errors compared to the optical velocities, generated from multi-object spectroscopy such as AAOmega, have uncertainties on the order of $\sim 100 \text{ km s}^{-1}$ (Baldry et al. 2014). The determined offsets between optical and Vela–H_I velocities range from 0.14 km s^{-1} to 234 km s^{-1} .

In summary, of the 211 identified galaxies, 146 (70%) are associated with 2MASS/2MASX counterparts (Jarrett et al. 2000; Skrutskie et al. 2006), 140 (66%) have WISE counterparts (Wright et al. 2010; Cutri et al. 2021), 92 (44%) are associated with HIZOA detections (Staveley-Smith et al. 2016), 49 (23%) have IRSF counterparts (Williams et al. 2014; Said et al. 2016), 38 (18%) have IRAS counterparts (Helou & Walker 1988), and 35 (17%) are linked to HIPASS counterparts (Meyer et al. 2004). Of the 92 Vela–H_I detections with likely HIZOA counterparts, 27 have probable WISE counterparts. A noteworthy aspect of Vela–H_I is its partial overlap with the Vela–OPT/NIR survey. More than half (121 out of 211) of the identified counterparts originate from the overlap between Vela–H_I and Vela–OPT/NIR. These are labeled with prefixes ‘HyA’ and ‘Vel’ in the last column of the galaxy catalog (see online supplementary material).

4.5 H_I properties distributions

As a next step, we explore the overall distribution of the global H_I properties between Vela–H_I and Vela–SMGPS such as the recessional velocities (Fig. 11), the linewidths (w_{50}) and H_I masses (Fig. 12).

The heliocentric velocity distributions of Vela–H_I and Vela–SMGPS are shown in Fig. 11. The hatched blue histogram indicates galaxies above the GP, the orange histogram with the dotted pattern shows galaxies in Vela–SMGPS, and the cyan histogram shows galaxies below the GP. Because of the lower sensitivity of Vela–H_I, the median velocity is lower (7700 km s^{-1}) compared to that of Vela–SMGPS ($\sim 11600 \text{ km s}^{-1}$). However, both surveys uncover galaxies out to the redshift limit of the surveys (24000 km s^{-1}). Several prominent peaks are discernible across regions above, within, and below the GP, suggesting a continuity of LSS. While the significance of these peaks will be discussed in detail in Section 5, we identify and highlight some of them here.

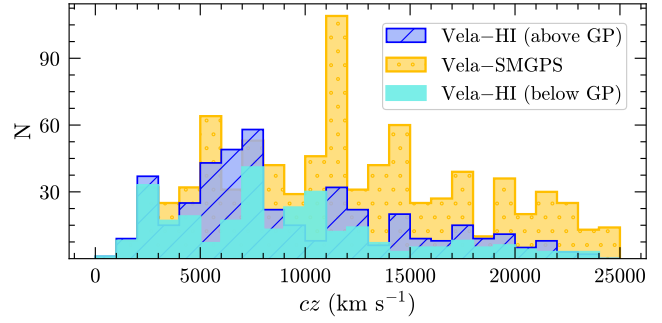


Figure 11. Histograms showing the heliocentric velocity distributions of the galaxies in Vela–H_I above the Plane (hatched blue), Vela–SMGPS (orange with dotted patterns), and Vela–H_I galaxies below the GP (cyan), respectively.

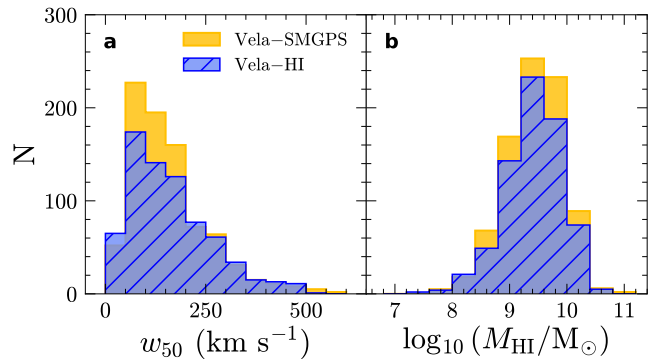


Figure 12. Histograms of the H_I parameters from the systematic blind H_I surveys Vela–H_I (719 galaxies, hatched blue) and Vela–SMGPS (843 galaxies, orange). Left panel (a) displays the linewidths (w_{50}) and right panel (b) shows the H_I mass distribution of detected galaxies.

Four peaks stand out in Fig. 11 at $2000-3000 \text{ km s}^{-1}$, $5000-8000 \text{ km s}^{-1}$, $11000-12000 \text{ km s}^{-1}$, and $14000-15000 \text{ km s}^{-1}$. The first peak is observed in both surveys. The second peak is broad, with its higher velocity range ($7000-8000 \text{ km s}^{-1}$) present both above and below the GP in Vela–H_I. The third peak has its origin entirely from the narrow filament unexpectedly discovered at $11000-12000 \text{ km s}^{-1}$ in Vela–SMGPS. Finally, the fourth peak is prominently seen in Vela–SMGPS, with a hint also observed above the GP in Vela–H_I.

Despite Vela–H_I covering a larger area with an rms nearly twice that of Vela–SMGPS, the distributions of linewidth and H_I mass in both surveys (Fig. 12) exhibit similar patterns. The average linewidths of 162 and 158 km s^{-1} are practically the same for Vela–H_I and Vela–SMGPS, respectively, given the coarse velocity channel width. Both show peaks between 50 and 100 km s^{-1} linewidth bin, with Vela–SMGPS showing more narrow linewidth galaxies between 50 to 200 km s^{-1} . They both follow the skewed pattern typical of blind systematic H_I surveys (cf. HIZOA, Staveley-Smith et al. 2016; the EBHIS Zone of Avoidance survey or EZOA, Schröder et al. 2019). This contrasts to optically or NIR-selected H_I surveys, which follow a more Gaussian distribution with a rise towards larger linewidths ($w_{50} > 200 \text{ km s}^{-1}$) because these tend to miss the bluer, low surface brightness dwarf population, as exemplified by Kraan-Korteweg et al. (2018).

The distribution of H_I masses (panel b) reveals about three orders of magnitudes in $\log(M_{\text{HI}}/\text{M}_\odot)$, 7.3 to 10.6 in Vela–H_I and 7.8

to 10.9 in Vela–SMGPS. They both peak between $9.2 - 9.6$, and have the same mean at $\log(M_{\text{HI}}/\text{M}_{\odot}) = 9.4$, despite Vela–SMGPS having a slightly higher number of galaxies per bin.

5 LARGE-SCALE STRUCTURES

5.1 Observational data in the Vela region

In this section, we discuss connections between previously identified and newly revealed LSS. As a starting point, we present Fig. 13 to visually guide the interpretation of these structures. It combines MeerKAT data from heavily obscured galaxies acquired through Vela–SMGPS and Vela–H α (purple and green boxes), along with ancillary datasets near the ZOA. These include galaxies with known redshifts from Vela–OPT/NIR (cyan circles), MeerKAT16 H α observations of the surrounding of the galaxy cluster VC04 ($272.25^\circ, -9^\circ, 18000 \text{ km s}^{-1}$, Hatamkhani et al. 2023), embedded in Wall 1 of the VSCL (Steyn 2023; light purple circles). Those at higher latitudes ($5^\circ \leq |b| \leq 15^\circ$) have redshifts from the 2MASS Redshift Survey (Huchra et al. 2012; Macri et al. 2019) and the HyperLEDA database (Makarov et al. 2014), represented by small crosses. Recent detections from the WALLABY-Vela field (Murugesan et al. 2024) are shown as open square symbols within the orange diamond shape above the GP. Different data point colors correspond to velocity ranges in intervals of 4500 km s^{-1} . The top panel displays three nearby velocity intervals, spanning from 2000 to 15500 km s^{-1} , which is the range probed by most surveys. The bottom panel presents the high-velocity range from 15500 to 24500 km s^{-1} , highlighting our new coverage with MeerKAT. The prominence of light and dark blue dots is already noticeable, with light blue indicating the distance range of Wall 1 and dark blue for Wall 2.

The region of high extinction, where optical and NIR galaxy counts become highly incomplete, is delineated by the white extinction contour. Caution is therefore advised when interpreting this on-sky plot and later LSS plots, as the presence of gaps around this contour does not necessarily indicate an area of underdensity.

The ZOA has now been quite thoroughly surveyed for the longitudinal range of $263^\circ < \ell < 284^\circ$. The new Vela–H α detections, with its sensitivity of $0.74 \text{ mJy beam}^{-1}$ extend out to 24000 km s^{-1} . Due to the difference in rms, the coverage in Vela–H α is approximately 3 galaxies per square degree compared to Vela–SMGPS with 9 galaxies per square degree. Both surveys highlight the effectiveness of systematic interferometric H α surveys in mapping LSS across the most obscured part of the ZOA, representing a significant step toward understanding the continuity of LSS.

5.2 Sensitivity curve and comparison with simulations

As an initial step in understanding how the overdensities within the inner ZOA align with known LSS, we analyze the velocity distribution and sensitivity curve of Vela–H α detections across the survey volume (see Fig. 14). Similar to the simulation S45 presented in Vela–SMGPS (see Rajohnson et al. 2024), which assumes constant H α mass and velocity width functions across redshifts to model a uniform galaxy distribution, we overlaid our H α detections on a simulation that matches the sensitivity ($0.75 \text{ mJy beam}^{-1}$) of Vela–H α . We focused on the survey area where it is complete (193 deg^2) after removing the high-noise regions toward the outermost edges and the mosaic A2B region. This simulation, hereafter referred to as S75, predicts 769 galaxies for Vela–H α .

The prediction from the S75 velocity distribution, representative

of a more uniform distribution, is shown by the cyan solid line. It reveals numerous over- and underdensities that are inconsistent with the uniformity (cyan line), clustering around $\sim 2500 \text{ km s}^{-1}$, 7000 km s^{-1} , $17000 - 18000 \text{ km s}^{-1}$ and $19000 - 20000 \text{ km s}^{-1}$. The last two peaks coincide with the redshift range of W1 and show an elongated distribution with H α mass. A hint of a broader but more shallow overdensity at $21000 - 24000 \text{ km s}^{-1}$ is also noticeable. Towards the line-of-sight of VSCL, an underdensity from $13000 - 17000 \text{ km s}^{-1}$ is observed.

5.3 Discussion of overdensities in the Vela region

In this section, we examine the on-sky distributions across varied redshift intervals, each for an interval of $\Delta v = 4500 \text{ km s}^{-1}$ increment range, with the aim of locating and identifying the distinct peaks more clearly. The redshifts in each 4500 km s^{-1} panel are subdivided into three increasing intervals of $\Delta v = 1500 \text{ km s}^{-1}$, from cyan, green, to blue color symbols, respectively.

We first focus on nearby structures within the velocity range $2000 < cz \leq 15500 \text{ km s}^{-1}$ (see Fig. 15), followed by galaxies at the distance range that encloses VSCL ($cz > 15500 \text{ km s}^{-1}$; Fig. 16). A zoom of the on-sky plots ($256^\circ \leq \ell \leq 294^\circ, |b| < 15^\circ$) is presented in the right-hand panel of Figs. 15 and 16. We additionally present redshift wedges out to $cz < 25000 \text{ km s}^{-1}$ in Fig. 17, which include galaxies that lie beyond the ZOA. These data are represented by blue and orange dots for those above (left panel) and below (right panel) the GP, respectively.

5.3.1 Nearby Structures: $cz \leq 15500 \text{ km s}^{-1}$

$2000 < cz \leq 6500 \text{ km s}^{-1}$: A substantial filament extends from the Hydra ($270^\circ, +27^\circ, 3400 \text{ km s}^{-1}$) and Antlia ($273^\circ, +19^\circ, 2600 \text{ km s}^{-1}$) clusters, often referred to as the Hydra Wall across the GP (Kraan-Korteweg et al. 1994, 1995; Fairall et al. 1998; Kraan-Korteweg 2000; Kraan-Korteweg et al. 2002). Cyan and green points from the Vela–H α together with the Vela–SMGPS data (Rajohnson et al. 2024) trace the Hydra wall for the first time as a contiguous structure across the ZOA. The alignment of blue and orange points in the wedge slices (both panels in Fig. 17) further confirms these results. Also recognized as the Hydra–Antlia extension (Kraan-Korteweg et al. 1995; Kraan-Korteweg 2000), the zoomed plot in the right panel reveals two branching structures crossing the GP at $\ell \sim 278^\circ$ and 282° at $2000 - 3500 \text{ km s}^{-1}$ and $\ell \sim 280^\circ$ at $3500 - 5000 \text{ km s}^{-1}$, concluding with a group of galaxies at $(\ell, b) \sim (281^\circ, -7^\circ)$. This feature is also evident as a prominent peak at $2000 - 3000 \text{ km s}^{-1}$ in the sensitivity curve plot in Fig. 14.

In the higher velocity range of $5000 - 6500 \text{ km s}^{-1}$, The alignment of blue dots in the wedge suggests the presence of a significant structure above the GP connecting to the Vela cluster AS639 ($280^\circ, +6^\circ, \sim 6000 \text{ km s}^{-1}$; Stein 1996), possibly originating from $\ell \sim 265^\circ, cz \sim 5500 \text{ km s}^{-1}$.

$6500 < cz \leq 11000 \text{ km s}^{-1}$: The inclusion of new Vela–H α data reveals previously undiscovered wall-like interconnecting structures (cyan dots) that cross the ZOA. The first hint of this structure was observed as a probable filament within the GP in Rajohnson et al. (2024) at $\ell \sim 260^\circ - 277^\circ$ and velocity ranges around $7000 - 9000 \text{ km s}^{-1}$. In the on-sky plots, this is observed as a diagonal structure of cyan dots ($6500 - 8000 \text{ km s}^{-1}$) crossing the inner GP within the longitudinal range of $266^\circ \leq \ell \leq 275^\circ$. It is reflected as the highest peak in the velocity histogram in Fig. 14. This structure

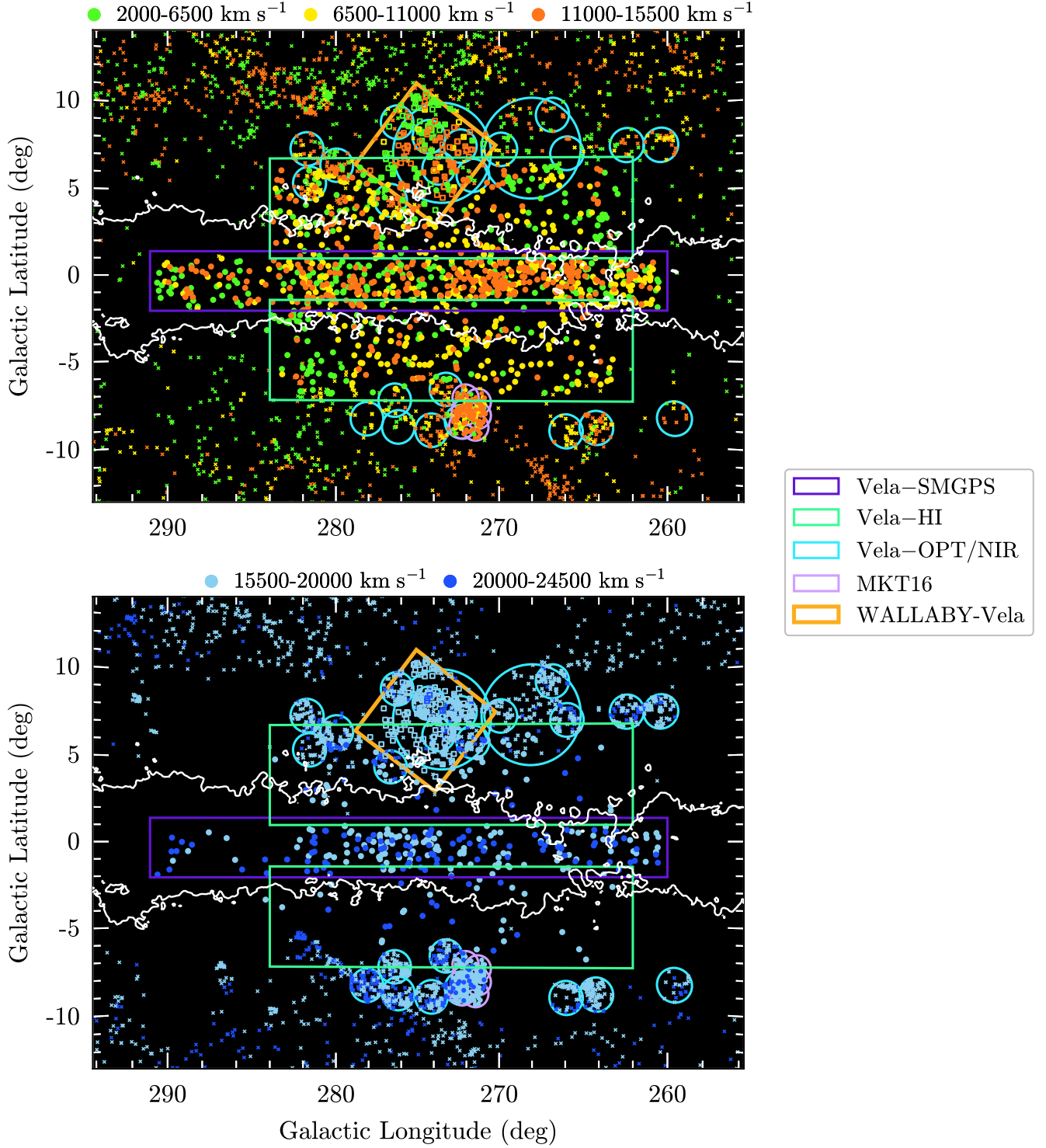


Figure 13. Spatial distributions in Galactic coordinates of galaxies surveyed across the wider Vela region ($256^\circ < \ell < 294^\circ$, $|b| < 15^\circ$) with velocities reaching out to 24500 km s^{-1} from prior optical and H_I redshift surveys, combined with the systematic MeerKAT H_I surveys Vela-H_I and Vela-SMGPS. The top panel shows nearby velocity ranges at $2000 - 6500 \text{ km s}^{-1}$ (light green), $6500 - 11000 \text{ km s}^{-1}$ (yellow), and $11000 - 15500 \text{ km s}^{-1}$ (orange), while the bottom panel covers the higher velocity range near the VSCL distance: $15500 - 20000 \text{ km s}^{-1}$ (light blue), and $20000 - 24500 \text{ km s}^{-1}$ (dark blue). Large dots within the green and purple rectangles represent newly identified H_I-detected galaxies from Vela-H_I ($N = 719$), and previously detected H_I galaxies from Vela-SMGPS ($N = 843$) in the inner ZOA. Small crosses within cyan circles mark galaxies with redshifts obtained from Vela-OPT/NIR ($N = 3013$), while small crosses outside the circles encompass all other compiled redshifts from various surveys (HyperLEDA and 2MRS). MeerKAT16 survey detections ($N = 156$) appear as small dots within the six light purple circles around $b = -7^\circ$ (Steyn 2023). WALLABY-Vela detections (Murugesan et al. 2024, $N = 143$) are represented by open square symbols within the orange diamond-shaped region. The white contour outlines corrected dust extinction at $A_B \simeq 3.0$ mag based on the DIRBE maps (Schlegel et al. 1998; Schlafly & Finkbeiner 2011).

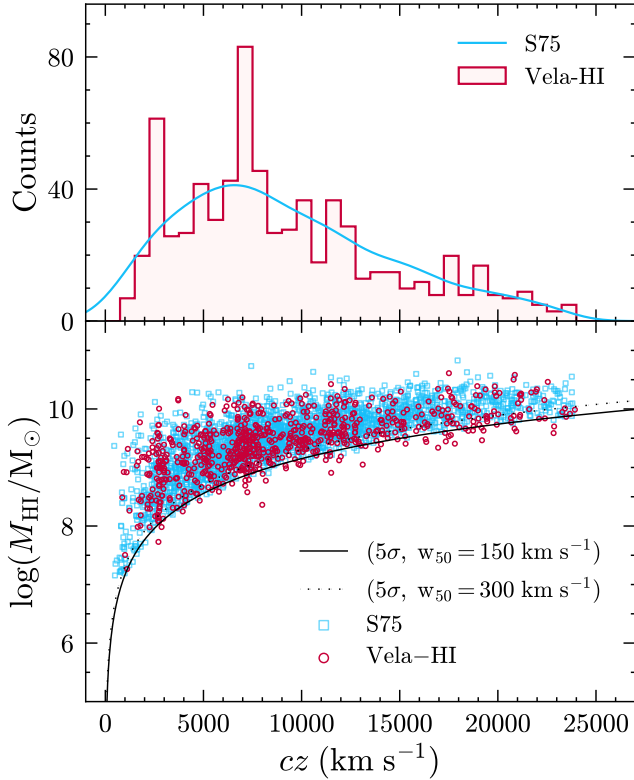


Figure 14. The top panel presents the histogram distribution of heliocentric velocities in light red. The cyan solid line corresponds to simulated galaxies for the full SMGPs (528 deg^2) with an rms of $0.75 \text{ mJy beam}^{-1}$ (S75) when scaled to the Vela-HI survey area (193 deg^2). The bottom panel shows a sensitivity curve illustrating the correlation between H I masses and heliocentric velocities for Vela-HI detections (depicted as red dots), accompanied by the simulated galaxies in S75 (cyan squares). The solid and dashed lines represent the 5σ detection limits for w_{50} values of 150 km s^{-1} and 300 km s^{-1} , respectively.

not only extends spatially below the GP but also appears to be connected to AS639 and higher velocity structures below the Plane (see orange dots in the velocity wedges). It then reaches the blue dots within $9500 - 11000 \text{ km s}^{-1}$ at $276^\circ \leq \ell \leq 280^\circ, b \sim -6^\circ$, which also appear to originate from the alignment of blue dots that cross the GP at $\ell \sim 281^\circ$. This crossing results in a distinctive void of approximately 10 Mpc in size at $\ell \sim 279^\circ, b \sim 0^\circ$ (see magenta circles in Fig. 15 and Fig. 17, labeled V1).

$11000 \leq cz \leq 15500 \text{ km s}^{-1}$: Despite the lower density of data points for Vela-HI compared to Vela-SMGPS, the continuation of green dots ($12500 - 14000 \text{ km s}^{-1}$) suggests potential branching of three structures of the narrow filaments discovered in Rajohnson et al. (2024). These structures cross the GP near longitudes of $\ell \sim 270^\circ, 276^\circ$, and 279° . However, due to the limited number of Vela-HI detections, it is uncertain whether the first two potential crossings of the filaments extend above the GP (see thinner dashed purple lines).

5.3.2 Higher- z Structures: $cz > 15500 \text{ km s}^{-1}$

Figure 16 presents the higher redshift ranges, which are directly relevant to our investigation of VSCL. The panels are divided into two segments ($15500 - 20000 \text{ km s}^{-1}$ and $20000 - 24500 \text{ km s}^{-1}$) to provide insights into both VSCL walls. Due to the lower sensitivity,

the links are not as clearly depicted compared to the lower redshift ranges.

$15500 \leq cz \leq 20000 \text{ km s}^{-1}$: galaxies marked by the continuation of green points ($17000 - 18500 \text{ km s}^{-1}$) implies the presence of Wall 1 (W1). This structure appears to originate from a dense clump at $(\ell, b) \sim (272.5^\circ, 6^\circ)$, intersecting the ZOA at least at around $\ell \sim 275^\circ \pm 1^\circ$, and reaching another concentration below the GP at $(\ell, b) \sim (276.5^\circ, -7^\circ)$. The alignment of blue dots at $18500 - 20000 \text{ km s}^{-1}$, on the other hand, seems to cross at least two locations in the GP (see purple-shaded circle). One branch likely merges in the inner GP at $\ell \sim 277^\circ$, while another filament of blue dots, originating from above the GP, crosses at $\ell \sim 272.5^\circ$, reaching the clustering below the Plane at $(\ell, b) \sim (272.5^\circ, -8^\circ)$. The velocity distribution of Vela-HI shown in Fig. 14 further supports these findings, displaying two peaks indicating overdensities at $17000 - 18000 \text{ km s}^{-1}$ and $19000 - 20000 \text{ km s}^{-1}$, although with lower significance than in Vela-SMGPS distribution (see Fig. 11).

A notable observation in this panel is the connection from the cluster A3391 ($262.37^\circ, -25.16^\circ, 15919 \text{ km s}^{-1}$), where cyan and green dots ($15500 - 18500 \text{ km s}^{-1}$) extend to the clustering of blue dots ($18500 - 20000 \text{ km s}^{-1}$) below the GP. This connection aligns with two X-ray clusters (CIZA J0812.5-5714 and CIZA J0820.9-5704; Ebeling et al. 2002), at approximately the same redshift (18587 and 18287 km s^{-1} , respectively). The structure then continues as a dense filamentary structure containing clusters and groups above the GP. This might explain why the two peaks at $17000 - 18000 \text{ km s}^{-1}$ and $19000 - 20000 \text{ km s}^{-1}$ are prominently observed above the Plane for Vela-HI (cf. Fig. 11). We propose that the underdensity visible above the GP at $\ell \sim 273^\circ, b \sim 15^\circ$, around 15500 km s^{-1} , just before the redshift of the first wall, is a genuine void (designated as V2) due to the low number of galaxies shown by the sensitivity curve in Fig. 14. Moreover, the wedge diagram in the left panel of Fig. 17 shows hardly any galaxies in the region above the GP, out to $0^\circ < b < 20^\circ$. The overall arrangement of the two walls in this velocity range appears to be part of a multi-branching structure that coincidentally intersects within the longitude range of $270^\circ \leq \ell \leq 279^\circ$ and around $b \sim 0^\circ$.

$20000 \leq cz \leq 24500 \text{ km s}^{-1}$: Despite the low number of detections due to sensitivity drop, a hint of a broad overdensity around $20000 - 21500 \text{ km s}^{-1}$ (cyan dots) and $21500 - 23000 \text{ km s}^{-1}$ (green dots) is observed within the range $270^\circ \leq \ell \leq 279^\circ$. It is slightly broader than suggested from the suspected Vela-SMGPS data. The structure seems to align with the X-ray cluster CIZA J0745.1-5404/ESO 163-IG015 ($266.84^\circ, -14.36^\circ, 22185 \text{ km s}^{-1}$; Kocevski et al. 2007). It reinforces the findings from Vela-SMGPS that the crossing seems to occur in the inner GP around velocities of $18500 - 21500 \text{ km s}^{-1}$. This potential intersection corresponds to the rough estimate that places the center of mass overdensity of the VSCL at the lowest latitudes around approximately $\sim 272^\circ$ (also see the cyan circle in the wedge diagram). This location was suggested from the examination of the region near Vela-OPT/NIR in KK2017. The result also aligns with the general direction of the core of a significant overdensity, as suggested from independent density and velocity field reconstructions by Sorce et al. (2017) and Courtois et al. (2019). This was recently strengthened by results from the linear density field reconstruction of the WALLABY-Vela (Mould et al. 2024). They place the core of the VSCL close to the center of mass overdensity predicted by KK2017 with a 4σ significance.

The wedge diagrams in Fig. 17 furthermore reveal distinguishable features between the walls traced by H I detections and those traced by OPT/NIR detections, suggestive of possible offsets between

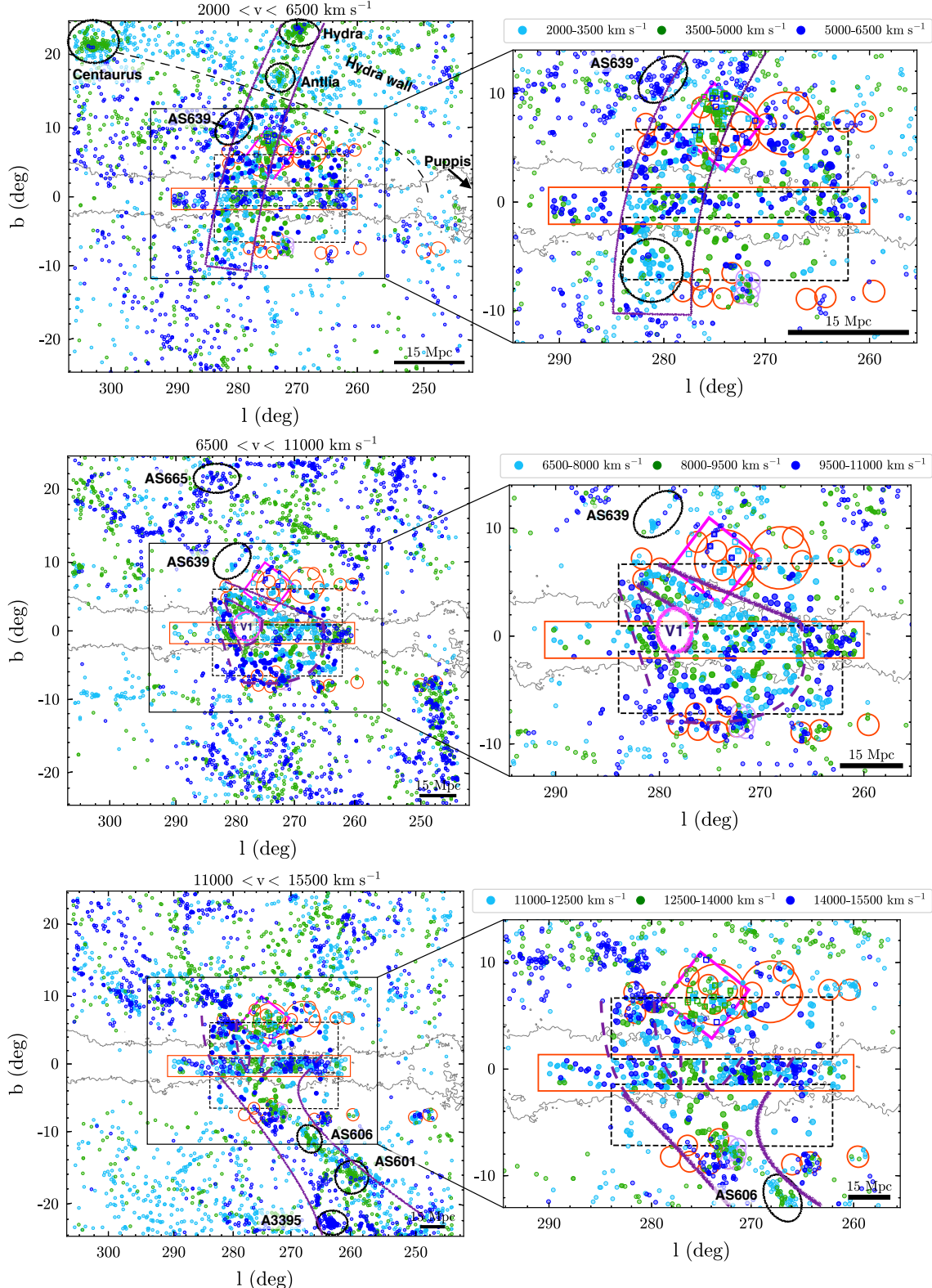


Figure 15. Annotated 2D on-sky distributions of galaxies in the Vela region and its surroundings ($244^\circ < \ell < 306^\circ, |b| < 25^\circ$). The figure displays three panels out to 15500 km s^{-1} , each representing a redshift interval with a $\Delta v = 4500 \text{ km s}^{-1}$ from 2000 km s^{-1} . The color codes within each panel mark increasing velocity bins of $\Delta v = 1500 \text{ km s}^{-1}$, from cyan, green, to blue. The newly discovered H_I galaxies in Vela-H_I are outlined by black dashed boxes, and Vela-SMGPS lie within the orange rectangle. Vela-OPT/NIR and MKT16 observations are denoted by orange and light purple open circles, respectively, while the WALLABY-Vela detections are represented by the open square symbols within the magenta diamond-shaped footprint. The dust extinction contour at $A_B \approx 3.0 \text{ mag}$ is represented by a solid grey line. Each panel includes a zoomed-in section within $256^\circ \leq \ell \leq 294^\circ, |b| < 15^\circ$ and a 15 Mpc scale bar positioned at its lower right side.

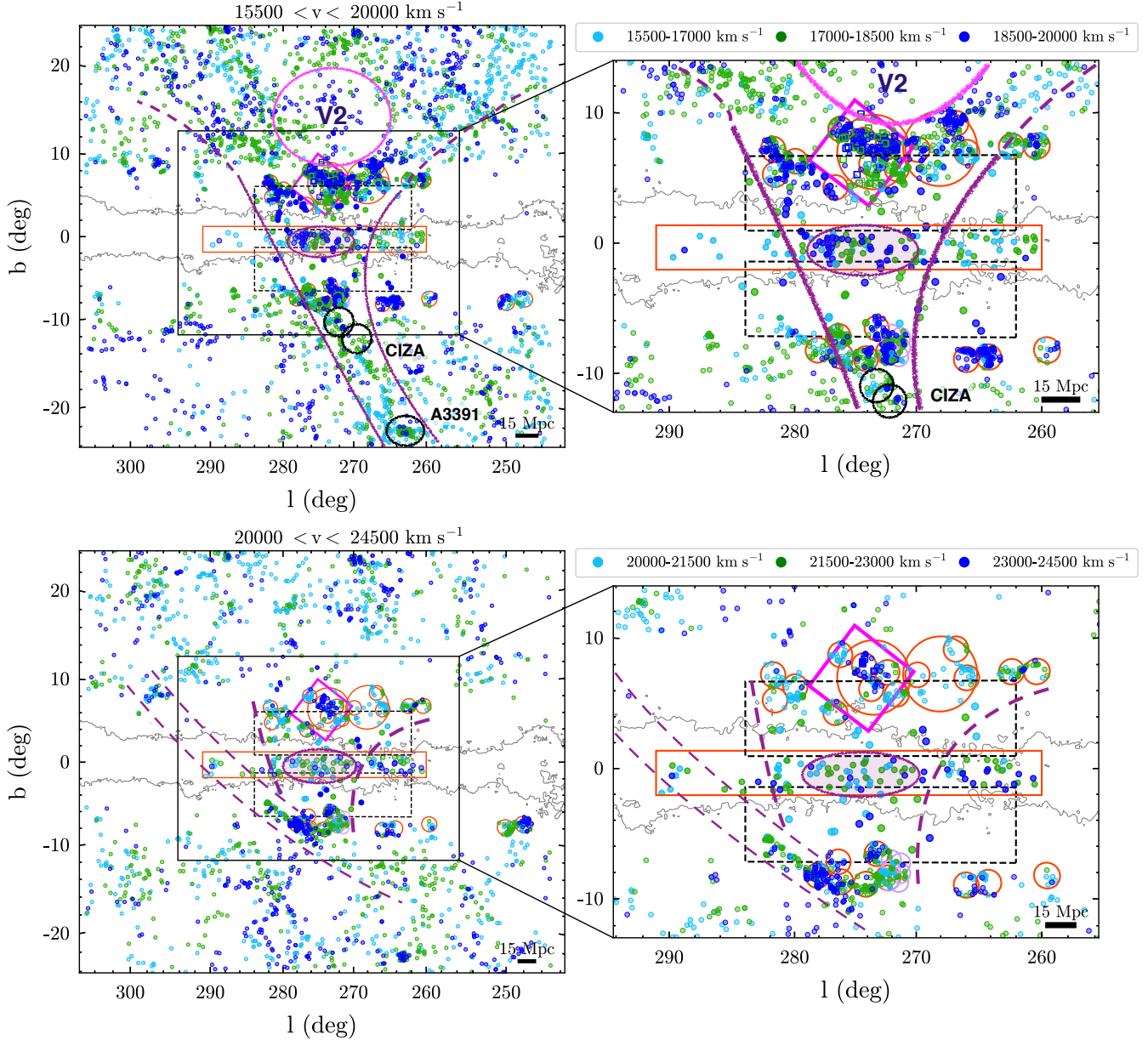


Figure 16. Similar to Fig. 15, but featuring two panels for the high-redshift velocity range, specifically $15500 < cz < 24500 \text{ km s}^{-1}$.

them. The shift of the H α detections with respect to OPT/NIR walls could indicate an ongoing collapse of the H α -rich galaxies towards the walls of the VSCL. Galaxies from the surrounding cosmic web could be gravitationally attracted and falling towards these walls, making those located at the periphery more H α -rich. Alternatively, interactions and pre-processing in the filaments may have stripped gas from the OPT/NIR wall (e.g., Sarron et al. 2019).

The less pronounced supercluster signature in Vela–H α compared to Vela–SMGPs may not only be due to its lower sensitivity. It is plausible that the relatively high number of detections concentrated in Vela–SMGPs is caused by the signature of the walls crossing at these lowest latitudes, raising – nearly doubling – the galaxy counts. While Vela–H α , with its $0.75 \text{ mJy beam}^{-1}$ sensitivity, is ‘only’ revealing the most H α -massive galaxies in Vela, they do trace the walls, but because of their lower density, the walls may overall contain fewer

very rich H α galaxies as they stream towards VSCL. This interpretation aligns with KK2017, proposing that the VSCL is a supercluster in formation, characterized by two merging wall-like structures. This hypothesis would also bolster the expectation suggested in Einasto et al. (2007) that high-density clusters are connected by lower-density filaments. In combination with the lower density, this could explain the low number of detections along the walls of VSCL. The spatial arrangement of galaxies evident in both the on-sky plot and wedge diagrams strongly suggests that the VSCL possesses the characteristic morphology of a rich supercluster. This morphology is characterized by an elongated, wall-like structure and the presence of multi-branching filaments, as proposed by (Einasto et al. 2011b). To get further insight into the crossing, a deeper H α survey targeting the suggested core location of the VSCL is deemed essential for further validation. Alternatively, running the DisPerSE filament finder (Sousbie 2011) might also help identify persistent structures quanti-

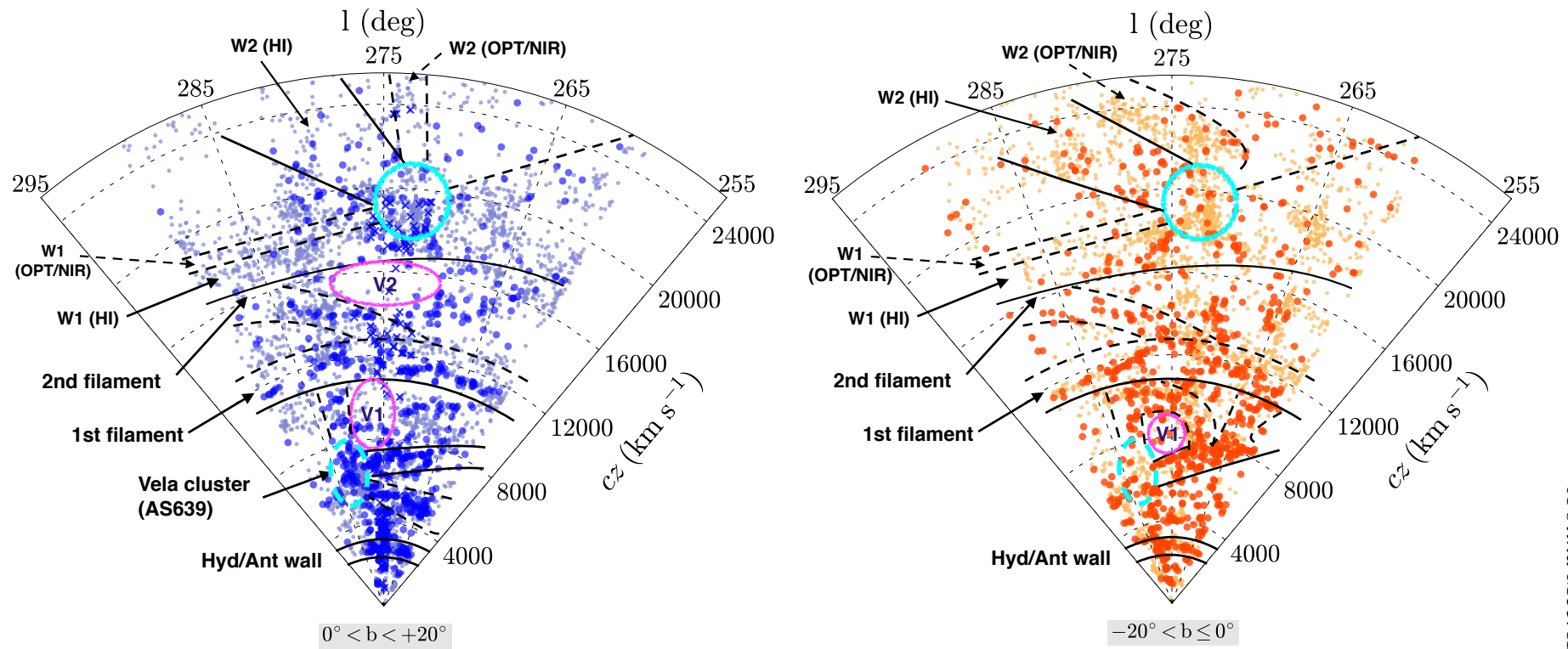


Figure 17. Annotated redshift wedge diagrams illustrating galaxies located above the Plane in blue (left panel) and below the Plane in orange (right panel), covering the Galactic latitude range of $-20^\circ < b < +20^\circ$ and Galactic longitude range $260^\circ \leq \ell \leq 290^\circ$, with $c_z < 25000 \text{ km s}^{-1}$. The smaller, lighter points represent ancillary data from OPT and NIR surveys surrounding the surveyed area, while the larger dots exclusively denote H α detections from Vela-SMGPS and Vela-H α . Recent H α detections from WALLABY-Vela are marked by blue crossed symbols in the left panel.

tatively.

6 CONCLUSIONS

In our quest to unravel the morphology and characteristics of the Vela Supercluster, concealed within the ZOA, we conducted a blind $\text{H}\alpha$ systematic MeerKAT Vela Supercluster survey, denoted as Vela– $\text{H}\alpha$. This survey was strategically positioned to address the formerly unexplored patches at $1^\circ \leq b \leq 6.2^\circ$ and $-6.7^\circ \leq b \leq -2^\circ$ in the Vela region. The survey design aims to establish connections between Vela–SMGPS ($-2^\circ \leq b \leq 1^\circ$, Rajohnson et al. 2024), and deep OPT/NIR observations at the outer edges of the ZOA in the general VSCL direction ($5^\circ \leq |b| \leq 10^\circ$, KK2017). Over approximately 67 hours, 667 MeerKAT pointings were collected, each lasting 5 minutes, covering an extensive area ($\sim 242 \text{ deg}^2$) both above and below the GP at $263^\circ \leq \ell \leq 284^\circ$. The dataset was analyzed and reduced, encompassing a velocity range up to $cz \sim 25000 \text{ km s}^{-1}$.

The Nyquist sampling configuration reduced the initial rms during data acquisition ($0.88\text{--}9.27 \text{ mJy beam}^{-1}$) to a final noise level of $0.68\text{--}1.24 \text{ mJy beam}^{-1}$ after solar RFI flagging and mosaicking were conducted.

In total, 719 $\text{H}\alpha$ sources in Vela– $\text{H}\alpha$ were detected and parameterized, revealing 508 previously unknown galaxies. Only 211 of these detections were previously recorded in the literature. Among them, only 66 have available redshift information with just five over $cz > 16000 \text{ km s}^{-1}$. These figures underscore the efficacy of blind $\text{H}\alpha$ surveys in identifying obscured galaxies within the ZOA. Obtaining the redshifts of these galaxies would be arduous or nearly impossible in optical, particularly at higher redshifts (VSCL distance). The Vela– $\text{H}\alpha$ parameters and positions demonstrate high quality: the measured integrated fluxes, linewidths, and systemic velocities are highly consistent with the previous Vela–SMGPS and HIZOA surveys.

The majority of OPT/NIR cross-matches lie within $5.6'' \pm 3.4''$ of the $\text{H}\alpha$ positions. Considering that Vela– $\text{H}\alpha$'s internal coordinate precision is approximately $6''$, this demonstrates excellent positional accuracy. The observed difference of $70 \pm 51 \text{ km s}^{-1}$ between the optical and $\text{H}\alpha$ velocities is also within the uncertainty of the optical velocities, which is on the order of 100 km s^{-1} .

The inclusion of 719 new redshift measurements significantly solidifies our understanding of the overall picture of the LSS when linking previously known structures at much higher latitudes in the Vela region. It clearly confirms the continuation of the Hydra/Antlia extension across the GP. Additionally, we have uncovered previously unknown LSS, including a diagonally structured wall possibly linked to AS639 and a void with a diameter of approximately 10 Mpc. At the distance of the VSCL, the distribution, connected to known clusters, reinforces the multi-branching morphology of the supercluster and affirms the existence of two potentially merging walls. This is further supported by recent independent reconstructions. When looking at the wedge diagrams, apparent offsets between the $\text{H}\alpha$ and OPT/NIR walls are observed, which seems to support the notion that VSCL is a supercluster in formation.

To conclude, combining data from Vela– $\text{H}\alpha$ and Vela–SMGPS has provided a clearer picture of the extent of the VSCL and improved our understanding of LSS in the Vela region out to 25000 km s^{-1} . The presence of this previously hidden core, supported by

$\text{H}\alpha$ observations prominent both above and below the GP, is a first significant step toward assessing its effect on the cosmic flow fields. However, quantifying the core and its impact requires more extensive studies beyond the scope of a single paper. We are addressing this in an upcoming paper, where we aim to measure the potential overdensity at the core of the VSCL using $\text{H}\alpha$ mass functions, and we have signs of a clear quantitative overdensity. With adequate photometry, the data quality and statistics should also enable us to determine peculiar velocities and potentially obtain velocity field distributions in the Vela region in the future.

ACKNOWLEDGEMENTS

The MeerKAT telescope is operated by the South African Radio Astronomy Observatory, which is a facility of the National Research Foundation, an agency of the Department of Science and Innovation. We acknowledge the use of the ilifu cloud computing facility – www.ilifu.ac.za, a partnership between the University of Cape Town, the University of the Western Cape, the University of Stellenbosch, Sol Plaatje University, the Cape Peninsula University of Technology and the South African Radio Astronomy Observatory. The ilifu facility is supported by contributions from the Inter-University Institute for Data Intensive Astronomy (IDIA – a partnership between the University of Cape Town, the University of Pretoria, the University of the Western Cape and the South African Radio astronomy Observatory), the Computational Biology division at UCT and the Data Intensive Research Initiative of South Africa (DIRISA). This work made use of the CARTA (Cube Analysis and Rendering Tool for Astronomy) software (DOI 10.5281/zenodo.3377984 – <https://cartavis.github.io>).

This paper makes use of the MeerKAT data with Project ID: SCI-20210212-SR-01. (Part of) the data published here have been reduced using the CARACal pipeline, partially supported by ERC Starting grant number 679629 “FORNAX”, MAECI Grant Number ZA18GR02, DST-NRF Grant Number 113121 as part of the ISARP Joint Research Scheme, and BMBF project 05A17PC2 for D-MeerkAT, and partially supported by the South African Research Chairs Initiative of the Department of Science and Technology and National Research Foundation. Information about CARACal can be obtained online under the URL: <https://caracal.readthedocs.io/en/latest/>.

SHAR, RCKK, HC, NS, SK, and DJP are supported by the South African Research Chairs Initiative of the Department of Science and Technology and National Research Foundation.

We acknowledge the usage of the HyperLeda database (<http://leda.univ-lyon1.fr>). This research has made use of: the NASA/IPAC Extragalactic Database (NED), which is operated by the Jet Propulsion Laboratory, California Institute of Technology, under contract with the National Aeronautics and Space Administration; the NASA's Astrophysics Data System Bibliographic Services; the VizieR catalogue access tool, CDS, Strasbourg, France (DOI:10.26093/cds/vizier). The original description of the VizieR service was published in 2000, A&AS 143, 23. This publication makes use of data products from: the Two Micron All Sky Survey, which is a joint project of the University of Massachusetts and the Infrared Processing and Analysis Center/California Institute of Technology, funded by the National Aeronautics and Space Administration and the National Science Foundation; the Wide-field Infrared Survey Explorer, which is a joint project of the University of California, Los Angeles, and the Jet Propulsion Laboratory/California Institute of Technology, funded by the National Aeronautics and Space

Administration. This research made use of [Astropy](#), a community-developed core Python package for Astronomy ([Astropy Collaboration et al. 2013, 2018](#)).

DATA AVAILABILITY

The full Vela-H I catalog and atlas can now be accessed online. The former is available as supplementary ASCII material, while the latter can be found in the Zenodo repository at <https://doi.org/10.5281/zenodo.12522807>. The raw MeerKAT Open Time data should now be publicly accessible at <https://archive.sarao.ac.za>, and the author can provide reduced H I cubes and/or mosaics upon request.

REFERENCES

- Astropy Collaboration et al., 2013, [A&A](#), **558**, A33
 Astropy Collaboration et al., 2018, [AJ](#), **156**, 123
 Baldry I. K., et al., 2014, [MNRAS](#), **441**, 2440
 Bock D. C. J., Large M. I., Sadler E. M., 1999, [AJ](#), **117**, 1578
 Boubel P., Colless M., Said K., Staveley-Smith L., 2024, [MNRAS](#), **531**, 84
 CASA Team et al., 2022, [PASP](#), **134**, 114501
 Carrick J., Turnbull S. J., Lavaux G., Hudson M. J., 2015, [MNRAS](#), **450**, 317
 Courtois H. M., Kraan-Korteweg R. C., Dupuy A., Graziani R., Libeskind N. I., 2019, [MNRAS](#), **490**, L57
 Cutri R. M., et al., 2021, VizieR Online Data Catalog, p. II/328
 Ebeling H., Mullis C. R., Tully R. B., 2002, [ApJ](#), **580**, 774
 Einasto M., et al., 2007, [A&A](#), **476**, 697
 Einasto M., Liivamägi L. J., Tago E., Saar E., Tempel E., Einasto J., Martínez V. J., Heinämäki P., 2011a, [A&A](#), **532**, A5
 Einasto M., et al., 2011b, [ApJ](#), **736**, 51
 Fairall A. P., Woudt P. A., Kraan-Korteweg R. C., 1998, [A&AS](#), **127**, 463
 Ginsburg A., et al., 2019, [AJ](#), **157**, 98
 Green D. A., 2009, [Bulletin of the Astronomical Society of India](#), **37**, 45
 Hatamkhani N., Kraan-Korteweg R. C., Blyth S. L., Said K., Elagali A., 2023, [MNRAS](#), **522**, 2223
 Helou G., Walker D. W., 1988, in Infrared astronomical satellite (IRAS) catalogs and atlases. Volume 7.
 Huchra J. P., et al., 2012, [ApJS](#), **199**, 26
 Jarrett T. H., Chester T., Cutri R., Schneider S., Skrutskie M., Huchra J. P., 2000, [AJ](#), **119**, 2498
 Jonas J., MeerKAT Team 2016, in MeerKAT Science: On the Pathway to the SKA. p. 1, doi:[10.22323/1.277.0001](https://doi.org/10.22323/1.277.0001)
 Józsa G. I. G., et al., 2020, CARACal: Containerized Automated Radio Astronomy Calibration pipeline (ascl:2006.014)
 Kocevski D. D., Ebeling H., Mullis C. R., Tully R. B., 2007, [ApJ](#), **662**, 224
 Kraan-Korteweg R. C., 2000, [A&AS](#), **141**, 123
 Kraan-Korteweg R. C., Cayette V., Balkowski C., Fairall A. P., Henning P. A., 1994, in Balkowski C., Kraan-Korteweg R. C., eds, Astronomical Society of the Pacific Conference Series Vol. 67, Unveiling Large-Scale Structures Behind the Milky Way. p. 99
 Kraan-Korteweg R. C., Fairall A. P., Balkowski C., 1995, [A&A](#), **297**, 617
 Kraan-Korteweg R. C., Henning P. A., Schröder A. C., 2002, [A&A](#), **391**, 887
 Kraan-Korteweg R. C., Cluver M. E., Bilicki M., Jarrett T. H., Colless M., Elagali A., Böhringer H., Chon G., 2017, [MNRAS](#), **466**, L29
 Kraan-Korteweg R. C., van Driel W., Schröder A. C., Ramatsoku M., Henning P. A., 2018, [MNRAS](#), **481**, 1262
 Kurapati S., et al., 2024, [MNRAS](#), **528**, 542
 Macri L. M., et al., 2019, [ApJS](#), **245**, 6
 Makarov D., Prugniel P., Terekhova N., Courtois H., Vauglin I., 2014, [A&A](#), **570**, A13
 Meyer M. J., et al., 2004, [MNRAS](#), **350**, 1195
 Mould J., et al., 2024, [MNRAS](#),
 Murugeshan C., et al., 2024, arXiv e-prints, p. arXiv:2409.13130
 Ochsenbein F., Bauer P., Marcout J., 2000, [A&AS](#), **143**, 23
 Rajohnson S. H. A., et al., 2024, [MNRAS](#), **531**, 3486
 Said K., Kraan-Korteweg R. C., Jarrett T. H., Staveley-Smith L., Williams W. L., 2016, [MNRAS](#), **462**, 3386
 Sarron F., Adami C., Durret F., Laigle C., 2019, [A&A](#), **632**, A49
 Schlafly E. F., Finkbeiner D. P., 2011, [ApJ](#), **737**, 103
 Schlegel D. J., Finkbeiner D. P., Davis M., 1998, [ApJ](#), **500**, 525
 Schröder A. C., Flöer L., Winkel B., Kerp J., 2019, [MNRAS](#), **489**, 2907
 Schröder A. C., van Driel W., Kraan-Korteweg R. C., 2021, [MNRAS](#), **503**, 5351
 Scrimgeour M. I., et al., 2016, [MNRAS](#), **455**, 386
 Serra P., et al., 2015, [MNRAS](#), **448**, 1922
 Skrutskie M. F., et al., 2006, [AJ](#), **131**, 1163
 Smirnov O. M., Heywood I., Perkins S. J., van Rooyen R., 2022, in Ruiz J. E., Pierfederici F., Teuben P., eds, Astronomical Society of the Pacific Conference Series Vol. 532, Astronomical Data Analysis Software and Systems XXX. p. 385
 Sorce J. G., Colless M., Kraan-Korteweg R. C., Gottlöber S., 2017, [MNRAS](#), **471**, 3087
 Sousbie T., 2011, [MNRAS](#), **414**, 350
 Springob C. M., et al., 2016, [MNRAS](#), **456**, 1886
 Staveley-Smith L., Kraan-Korteweg R. C., Schröder A. C., Henning P. A., Koribalski B. S., Stewart I. M., Heald G., 2016, [AJ](#), **151**, 52
 Stein P., 1996, [A&AS](#), **116**, 203
 Steyn N., 2023, First MeerKAT H I survey results mapping large scale structures hidden behind the Milky Way out to $z = 0.08$, <http://hdl.handle.net/11427/38045>
 Steyn N., et al., 2024, [MNRAS](#), **529**, L88
 Westmeier T., et al., 2021, [MNRAS](#), **506**, 3962
 Williams W. L., Kraan-Korteweg R. C., Woudt P. A., 2014, [MNRAS](#), **443**, 41
 Wright E. L., et al., 2010, [AJ](#), **140**, 1868

APPENDIX A: RESIDUAL RFI

This appendix explains the method employed to address short-track bugs and solar RFI observed in the Vela–HI datasets before executing the CARACal pipeline.

A1 Short track bugs

The short track bug occurs during telescope slewing, where the initial two or three integrations from this motion are erroneously recorded as a track lasting eight seconds or less when the telescope moves to a new field. In Fig. A1, we have highlighted these short tracks in yellow. They are visibly shorter (see the column TIMERANGE (UTC)), containing fewer rows of data compared to an actual track. If left unflagged, the short track bug can cause emission from the previous field to erroneously appear in the subsequent field as faint ‘ghost’ images. While CARACal automatically identifies and flags this bug, it can also be manually addressed in CASA (CASA Team et al. 2022) by carefully noting the affected scans and flagging them before calibration.

MeasurementSet Name: /stimela_mount/msdir/1633134084_sdp_10.ms MS Version 2							
Observer: Sambatriniaina Rajohnson Project: 20210331-0021							
Observation: MeerKAT							
Data records: 24791010 Total elapsed time = 29137.7 seconds							
Observed from 02-Oct-2021/00:24:34.8 to 02-Oct-2021/08:30:12.5 (UTC)							
ObservationID = 0	ArrayID = 0						
Date	Timerange (UTC)	Scan	FldId	FieldName	nRows	SpwIds	Average Interval(s) ScanIntent
02-Oct-2021/00:24:34.8 – 00:24:42.8		1	0	J0408-6545	7320	[0] [2]	[CALIBRATE_BANDPASS,CALIBRATE_FLUX]
00:24:42.8 – 00:27:48.7		2	0	J0408-6545	170190	[0] [2]	[CALIBRATE_BANDPASS,CALIBRATE_FLUX]
00:28:26.7 – 00:30:24.6		3	1	J0825-5010	107970	[0] [2]	[CALIBRATE_AMPLI,CALIBRATE_PHASE]
00:30:24.6 – 00:30:28.6		4	2	B11L16	3660	[0] [2]	[TARGET]
00:30:44.6 – 00:33:12.6		5	2	B11L16	135420	[0] [2]	[TARGET]
00:33:12.6 – 00:33:16.6		6	3	B11L17	3660	[0] [2]	[TARGET]
00:33:24.6 – 00:35:52.5		7	3	B11L17	135420	[0] [2]	[TARGET]
00:35:52.5 – 00:35:56.5		8	4	B11L18	3660	[0] [2]	[TARGET]
00:36:04.5 – 00:38:32.4		9	4	B11L18	135420	[0] [2]	[TARGET]
00:38:32.4 – 00:38:36.4		10	5	B11L19	3660	[0] [2]	[TARGET]
00:38:44.4 – 00:41:12.4		11	5	B11L19	135420	[0] [2]	[TARGET]

Figure A1. An example of a CASA ‘listobs’ file summarizing the observation information for the measurement set of block C2. Short-track bugs, which require flagging, have been highlighted in yellow.

A2 Solar RFI and 1380 MHz spike

Initially, our blocks of observations all started during nighttime. However, due to the extensive duration (8 – 9 hrs) of each session and a large number of targets, roughly 69% of our data was acquired during the daytime. This distribution is summarized in Table A1, where blocks A1 and A2 have collected more than 80% of their data during daytime. This had significant implications, particularly for short baselines directed toward the Sun during sunrise and sunset, which were susceptible to picking up solar interference.

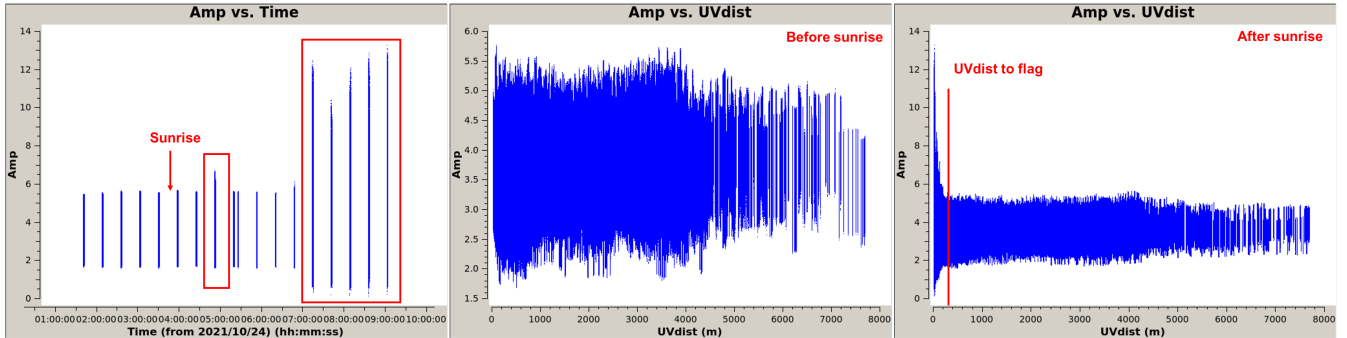
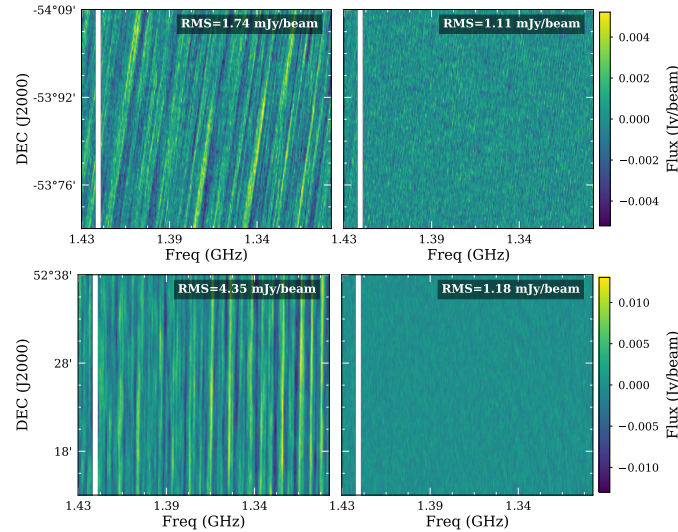
Upon inspecting the data, we observe a sudden fluctuation in amplitude (see left panel of Fig. A2). The observed deviation, occurring immediately after sunrise, is attributed to solar RFI. The latter translates into peculiar ripples discernible in both the spatial and spectral axes when generating the HI cubes, as demonstrated in the left panels of Fig. A3.

As shown in the middle panel of Fig. A2, the variation of amplitude as a function of UV distance remains stable before sunrise. However, after sunrise, a significant variation is observed, particularly for UV distances below 300 m. When this occurs, it is crucial to flag affected daytime visibilities. It is important to emphasize that not all daytime data requires flagging. Specifically, flagging is necessary during the interference duration and for the affected baselines only. The baselines primarily affected are those with the shortest projected lengths when aligned with the rising or setting Sun’s path. The most severely affected baselines are listed in the MeerKAT Users portal documentation⁵. Our measurements, detailed in Table A1, indicate that baseline lengths shorter than 315 m ($\sim 1.5 \text{ k}\lambda$) should be flagged for blocks A2, B2, C2, D1, and D2. For A1 and B1, this threshold is 210 m ($\sim 1 \text{ k}\lambda$). The flagged data and the total number of affected baselines together comprise less than 8.1% of the total baselines and data, resulting in a relatively low impact on sensitivity.

⁵ <https://skaafrica.atlassian.net/wiki/spaces/ESDKB/pages/336232568/Known+issues> (status 28/08/2024, 14:05 UTC)

Table A1. Overview of flagged Solar RFI in Vela–H_I data, including the percentage of daytime data and the affected baseline length that requires flagging

Block ID	Daytime data (%)	Affected baseline length (m)	Flagged data (%)
A1	81.4	210	7.9
A2	89.2	315	12.0
B1	64.9	210	5.7
B2	69.1	315	6.1
C1	64.5	210	6.2
C2	40.9	315	6.1
D1	75.2	315	10.7
D2	71.9	315	10.4


Figure A2. Example of diagnostic plots for the gain calibrator J0825-5010 prior cross-calibration. The left panel displays the amplitude variation over time during the observations, with the sunrise (03:46 UTC) indicated by a red arrow. Scans impacted by solar RFI are marked by red boxes. The middle and right panels showcase the amplitude variation with UV distance, both pre and post-sunrise, respectively. In the right panel, the maximum UV distance for flagging ($UVdist < 1.5 k\lambda$ or 315m) after sunrise, specifically for the affected baselines, is denoted by the red vertical line.

Figure A3. Example of PV-slice of H_I cubes from two target fields. The left panel demonstrates the presence of ripple artifacts, which are effectively removed in the right panel following the solar RFI flagging process.

After flagging (right panel of Fig. A3), a substantial reduction or complete elimination of the ripple effect in the position-velocity (PV) slice of the H_I cubes is observed, leading to a significant improvement in sensitivity. This noise improvement in the H_I cubes is further illustrated in the first two panels of Fig. A4. The measured rms prior to solar RFI flagging ranges from 0.88 to 9.27 mJy beam⁻¹. Cubes previously highlighted in dark red (with $rms > 2$ mJy beam⁻¹) in the top panel, are now shaded in orange and yellow (i.e., $rms \sim 1$ mJy beam⁻¹), marking a twofold increase in sensitivity after solar RFI flagging, with rms values now ranging from 0.88 – 2.57 mJy beam⁻¹. This noise improvement continues to be remarkable after mosaicking (see Section 3.2), achieving an rms noise spanning from 0.68 to 1.24 mJy beam⁻¹ in the bottom panel of Fig. A4. However, we note that the color coding in the bottom panel does not account for the spatial variation of the noise within each mosaic. It only represents the mean noise in the mosaic, so all fields belonging to the same mosaic (as shown in Fig. 2) are assigned the same

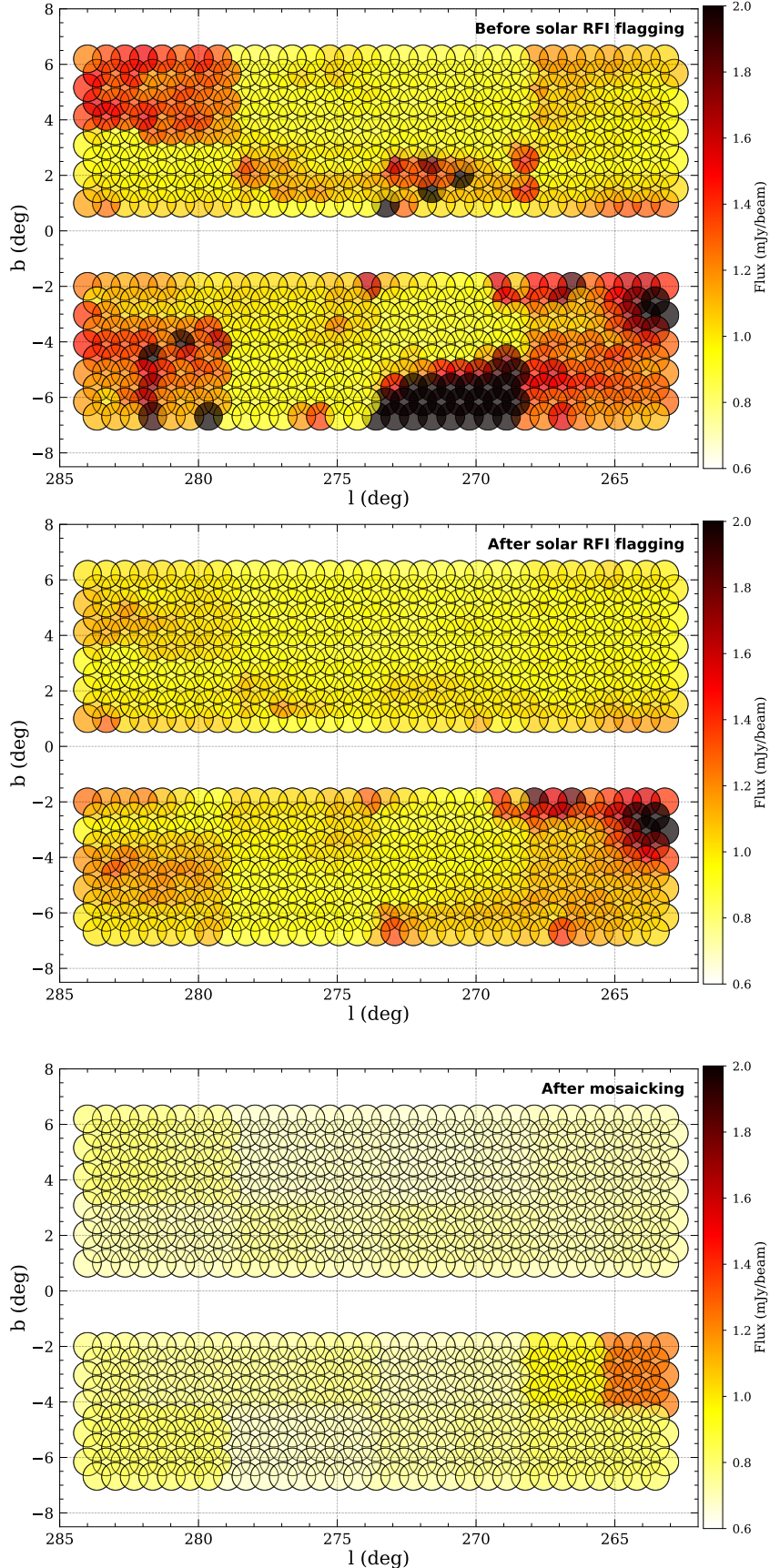


Figure A4. Rms variations and improvements per field before and after RFI flagging and mosaicking. In the bottom panel, all fields in the same mosaic share the same color code, indicating the mean noise of that mosaic.

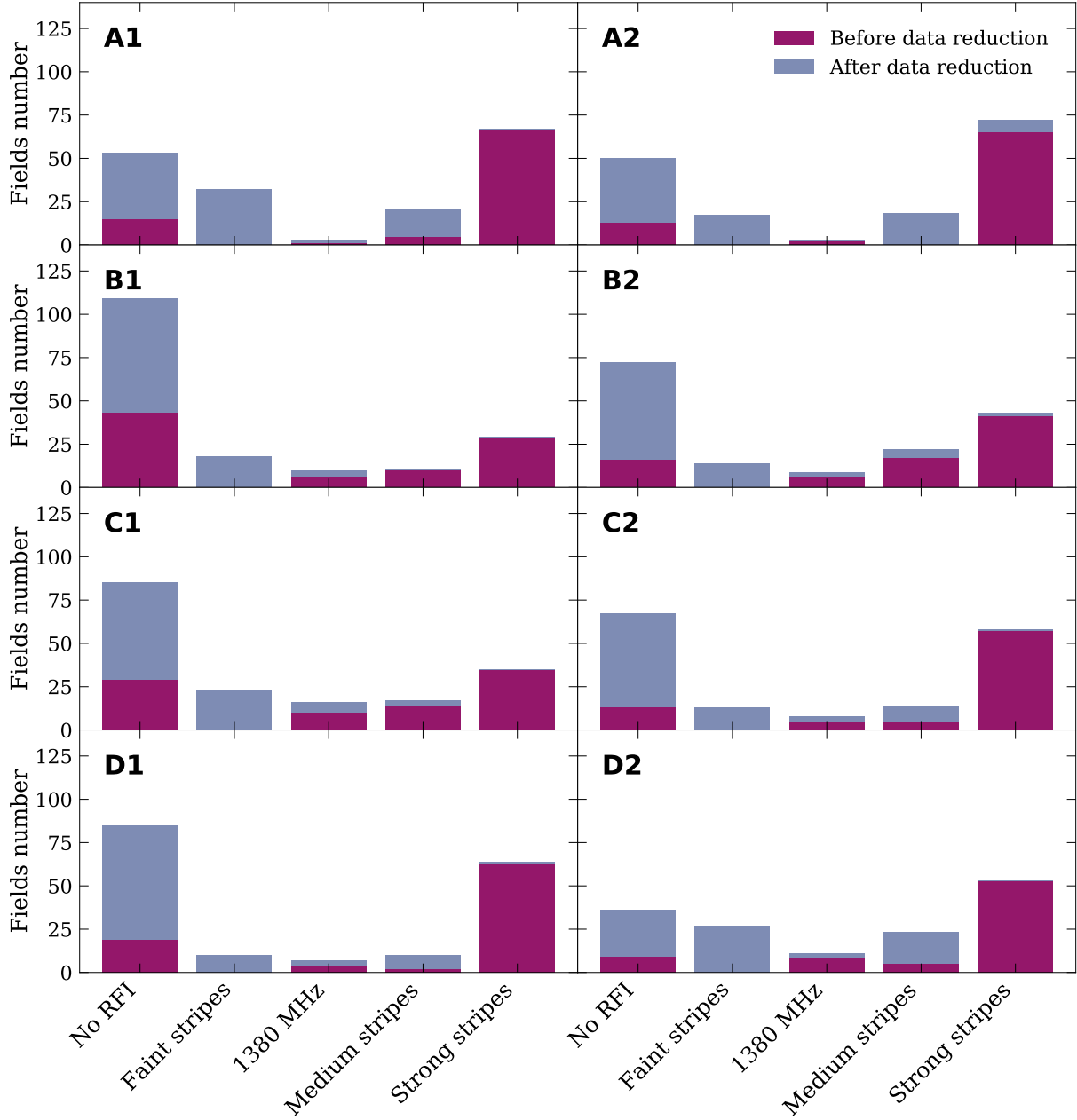


Figure A5. Histogram displaying the transition of fields from showing strong stripes affected by solar and 1380 MHz RFI to a state of no RFI in each Vela–H_I block, both before (light purple) and after (dark purple) data reduction

color and, hence, the same noise level in this figure.

Finally, an additional flagging step is performed after self-calibration and continuum subtraction, just before the imaging step. This step utilizes CASA tasks `TFCROP` and `RFLAG` to eliminate residual RFI sidelobes, primarily originating from Global Positioning System (GPS) satellites. While the telescope system automatically flags the strong peak at ~ 1380 MHz, further action is required if it persists in the spectral axis of the H_I cube. This scenario arises for blocks A2, B2, C1, and C2, so we applied time and frequency cutoffs of 4σ and 3σ in `TFCROP`, and 4σ in both time and frequency for `RFLAG`.

Prior to calibration and flagging, over half of the target fields in each block (greater than 50 fields) displayed some form of stripes (classified as either strong, medium, faint, or 1380 MHz spike) in their maps, impacting our observations. After solar RFI removal and data reduction, a significant improvement in data quality is observed. Now, the majority of fields are free from RFI or exhibit medium and faint stripes, as indicated by the light purple shading in Fig. A5. While a few instances persist, they are considered acceptable.

APPENDIX B: VELA-HI FULL CATALOG

The following Appendix provides a detailed description of the catalog parameters for Vela-HI, which are primarily sourced from the SoFiA output unless mentioned otherwise. The complete catalog is available in Table B1.

Column (1): Source Identifier (VSCL-HI Jhhmmss-ddmmss) representing rounded right ascension and declination in equatorial coordinates (J2000) of the centroid position.

Column (2): Indicates the name of the mosaic to which the source belongs. It is presented in the format of the block name along with the mosaic configuration (AXB), e.g., B1C [A1A to D2D].

Columns (3) and (4): Galactic Coordinates (ℓ and b) of the centroid position in degrees.

Column (5): Peak Flux density measured from the Global HI profile in Jy.

Columns (6) and (7): Integrated Flux along with its corresponding error ε_s in a unit of Jy km s $^{-1}$. This error value is the average standard deviation of the integrated fluxes, which are measured from four emission-free regions around the source.

Column (8): Mean Local rms in mJy beam $^{-1}$, averaged from four emission-free regions around the detection.

Column (9): Optical Heliocentric systemic velocity (V_{hel}) in km s $^{-1}$.

Columns (10) and (11): Linewidths (w_{20}, w_{50}) in km s $^{-1}$, corrected for instrumental resolution, and representing the widths at which the profile achieves 20% and 50% of its peak flux density.

Column (12): Logarithm of HI Mass [$\log(M_{\text{HI}}/\text{M}_\odot)$]. No corrections for Local Group barycenter or instrumental resolution were applied.

Column (13): Flags denoting the classification of detections. A flag of 1 indicates a solid detection, while 2 signifies a possible detection.

Additional notations include an asterisk (*) alongside the flag, indicating that the detection was also identified in the overlapping mosaic. A double asterisk (**) denotes that the detection was found in more than two adjacent mosaics, and an exclamation mark (!) indicates a common detection with Vela-SMGPS.

Column (14): Additional Notes and Multi-Wavelength Counterparts (if available). The notes cover various attributes:

- $B=40''$: The detection's moment maps have been smoothed to a specific angular resolution (e.g., 40'').
- BL : the Global HI profile shows a wiggly baseline
- e : detection located near the mosaic edge.
- i : with signs of interactions or mergers.
- r : the detection is located in (or close to) a noisy area due to the ripple caused by residual solar RFI.
- $w.\text{comp}(s)$: galaxy with one (or several) companion(s).
- $w_{20} \text{ unc.}$: w_{20} measurement unclear due to baseline behaviour.

Additionally, galaxies detected in major HI, OPT, and NIR catalogs are also indicated in the notes column. The methodology for identifying multi-wavelength counterparts is explained in Section 4.4. For galaxies found in HIZOA (Staveley-Smith et al. 2016) and/or Vela-OPT/NIR (KK2017, Kraan-Korteweg priv. comm), their object names (e.g., J0847-46, HyA0009, Vel0617) are provided. There are also other cases such as:

- H : counterpart from the southern region of the HIPASS catalog (Meyer et al. 2004).
- I : counterpart from the IRAS Point Source Catalog (Helou & Walker 1988).
- M : counterpart from 2MASX (Jarrett et al. 2000) and other 2MASS detections (Skrutskie et al. 2006, in the absence of 2MASX).
- W : counterpart from the Wide-field Infrared Survey Explorer catalog (WISE; Wright et al. 2010; Cutri et al. 2021).
- Z : counterpart from deep NIR follow-up observations conducted using IRSF (Williams et al. 2014; Said et al. 2016).

Table B1. Vela–H α full catalogue: H α data and derived properties.

Name J2000 (1)	Mosaic AXB (2)	l deg (3)	b deg (4)	S_{peak} Jy (5)	S_{int} Jy km s $^{-1}$ (6)	ε_s Jy km s $^{-1}$ (7)	RMS mJy beam $^{-1}$ (8)	V_{hel} km s $^{-1}$ (9)	w_{20} km s $^{-1}$ (10)	w_{50} km s $^{-1}$ (11)	M_{HI} $\log(M_{\text{HI}}/\text{M}_\odot)$ (12)	Flag 1/2 (13)	Note (14)
J081815-465710	A2D	263.291	-6.232	0.013	2.85	0.29	0.77	7804	251	211	9.93	1	w. comp (J081828-471025)
J081828-471025	A2D	263.497	-6.324	0.011	0.67	0.14	0.71	7822	153	105	9.30	1	B=40'', i, w.comp (J081815-465710)
J081845-473700	A2D	263.893	-6.531	0.017	4.49	0.26	0.71	7511	337	300	10.09	1	
J081859-483716	A2D	264.757	-7.055	0.013	0.64	0.12	0.98	18638	124	81	10.04	2	e
J082034-464906	A2D	263.401	-5.829	0.002	0.89	0.13	0.70	2148	67	50	8.30	1	
J082116-474921	A2D	264.305	-6.293	0.010	2.42	0.33	0.66	11824	405	363	10.22	1	i
J082148-463756	A2D	263.366	-5.549	0.011	1.27	0.21	0.72	9704	197	155	9.77	1	
J082210-473533	A2D	264.198	-6.040	0.011	1.86	0.19	0.67	7657	222	199	9.73	1	i, w.comp
J082259-493012	A2C	265.864	-7.005	0.024	1.44	0.30	1.14	7183	141	86	9.56	1*	e, i, M, W
J082307-484243	A2D	265.217	-6.542	0.010	0.40	0.08	0.64	10256	202	167	9.32	1	
J082323-483719	A2D	265.168	-6.454	0.006	0.36	0.09	0.58	19441	221	129	9.83	2	
J082328-474526	A2D	264.460	-5.951	0.011	0.89	0.15	0.65	7562	206	85	9.39	1	M, W
J082339-461120	A2D	263.180	-5.036	0.011	0.95	0.16	0.70	9605	257	114	9.63	1	BL
J082403-484045	A2D	265.279	-6.395	0.020	3.21	0.25	0.77	7950	160	106	10.00	1	w.comp, M, W
J082415-490116	A2D	265.581	-6.562	0.019	1.27	0.10	0.67	2230	112	75	8.48	1*	M, W
J082511-494217	A2C	266.234	-6.825	0.034	7.32	0.48	1.10	2219	262	219	9.24	1	e
J082525-465223	A2D	263.918	-5.177	0.010	1.76	0.24	0.65	11762	314	263	10.08	1	i?
J082600-495546	A2C	266.495	-6.845	0.016	1.12	0.18	1.27	8088	218	201	9.55	1	e, w.comp, M, W
J082640-481850	A2D	265.226	-5.831	0.012	0.81	0.24	0.66	4385	233	134	8.88	1	i
J082720-504023	A2C	267.233	-7.095	0.021	2.05	0.11	1.40	3942	114	73	9.19	1	B=40'', e
J082740-490308	A2C	265.929	-6.120	0.012	1.26	0.22	0.74	10745	212	175	9.85	1*	
J082833-475415	A2D	265.071	-5.338	0.010	0.59	0.13	0.64	8639	166	92	9.33	2	
J083055-464513	A2D	264.369	-4.341	0.011	0.34	0.07	0.75	10785	323	66	9.29	2	
J083153-485147	A2C	266.178	-5.448	0.009	0.30	0.06	0.66	18039	242	199	9.68	2	
J083216-481004	A2D	265.652	-4.986	0.011	1.27	0.23	0.64	14775	191	143	10.14	1*	i, w.comp
J083336-503002	A2C	267.674	-6.185	0.013	2.35	0.34	0.61	11487	440	412	10.18	1	M, W
J083428-445041	A2B	263.194	-2.712	0.014	1.38	0.18	1.39	18950	110	69	10.39	2	r
J083454-492228	A2C	266.885	-5.352	0.010	0.72	0.21	0.66	7746	164	91	9.32	1	
J083531-472125	A2D	265.321	-4.067	0.002	0.51	0.10	0.82	9318	244	178	9.33	2	BL
J083605-454046	A2B	264.034	-2.984	0.014	0.67	0.14	1.57	10989	181	151	9.60	2	r
J083649-521526	B2D	269.397	-6.823	0.011	1.12	0.25	0.73	7757	241	181	9.52	1	e
J083700-495429	A2C	267.520	-5.396	0.023	3.83	0.70	0.76	7782	282	209	10.05	1	BL, i, w.comps (one is J083709-495158), I, M, W
J083709-495158	A2C	267.500	-5.352	0.015	0.71	0.23	0.66	7535	76	56	9.29	1	w.comp (J083701-495424)
J083716-514442	B2D	269.024	-6.463	0.007	0.84	0.10	0.58	10552	171	155	9.66	1	
J083721-524428	B2D	269.838	-7.046	0.007	0.53	0.16	1.03	7710	109	62	9.19	2	e
J083840-474313	A2A	265.933	-3.859	0.009	0.41	0.10	0.62	4361	124	13	8.58	1	
J083855-502027	A2C	268.052	-5.412	0.017	1.41	0.33	0.72	7659	258	120	9.61	1	BL
J083908-512046	B2D	268.879	-5.990	0.006	0.53	0.15	0.63	10344	281	200	9.44	1	
J083931-485348	A2C	266.957	-4.460	0.010	0.41	0.08	0.72	7706	288	215	9.07	2	
J084027-504926	B2D	268.587	-5.510	0.011	2.87	0.28	0.88	7101	261	229	9.85	1	M
J084045-484718	A2C	266.994	-4.234	0.023	1.82	0.17	0.69	7684	66	43	9.72	1*	
J084057-510923	B2D	268.900	-5.650	0.008	0.30	0.06	0.68	23674	267	194	9.92	2	B=40''
J084058-482148	A2A	266.679	-3.946	0.007	0.37	0.10	0.67	7088	292	176	8.96	1	
J084059-482140	A2C	266.679	-3.942	0.006	0.44	0.08	0.81	7018	322	238	9.03	1	e
J084109-460955	A2B	264.956	-2.577	0.023	1.77	0.32	0.97	15054	167	133	10.30	1	
J084134-454513	A2B	264.674	-2.268	0.015	1.26	0.26	1.08	11629	514	485	9.92	1	i? M, W
J084137-525231	B2D	270.336	-6.612	0.006	0.28	0.06	0.72	22101	233	233	9.83	2	
J084148-512957	B2D	269.254	-5.753	0.010	1.40	0.17	0.74	10276	527	400	9.86	1	

* Detected by the overlapping region of the adjacent mosaic.

** Detected by the overlapping region of two or more adjacent mosaics.

! Detected by the overlapping region between Vela–H α and Vela–SMGPS.

Table ?? continued

Name J2000 (1)	Mosaic TXX (2)	l deg (3)	b deg (4)	S_{peak} Jy (5)	S_{int} Jy km s $^{-1}$ (6)	ε_s Jy km s $^{-1}$ (7)	RMS mJy beam $^{-1}$ (8)	V_{hel} km s $^{-1}$ (9)	w_{20} km s $^{-1}$ (10)	w_{50} km s $^{-1}$ (11)	M_{HI} $\log(M_{\text{HI}}/\text{M}_\odot)$ (12)	Flag 1/2 (13)	Note (14)
J084205-520158	B2D	269.707	-6.043	0.009	0.40	0.08	0.71	17589	420	325	9.79	1	BL
J084218-523509	B2D	270.168	-6.354	0.008	0.21	0.04	0.70	13890	334	174	9.31	2	BL, w_{20} unc.
J084240-520214	B2D	269.765	-5.975	0.010	0.62	0.09	0.61	6076	198	64	9.05	1	
J084413-511300	B2D	269.263	-5.282	0.015	4.29	0.35	0.77	7489	405	339	10.07	1	
J084426-470831	A2A	266.073	-2.736	0.008	0.23	0.06	0.58	9205	127	96	8.99	2	
J084437-470336	A2A	266.028	-2.660	0.019	1.18	0.24	0.74	7553	183	143	9.52	1	i
J084456-484457	A2A	267.389	-3.665	0.012	1.16	0.24	0.65	7101	210	166	9.45	1	i, M, W
J084457-522946	B2D	270.346	-5.980	0.011	0.88	0.22	0.66	8955	359	211	9.54	1	i, M
J084537-530512	B2D	270.875	-6.266	0.009	0.95	0.30	0.65	7688	176	89	9.44	1*	
J084602-514431	B2D	269.853	-5.384	0.009	0.97	0.16	0.59	18883	320	295	10.24	1	
J084608-533832	B2C	271.363	-6.548	0.004	0.15	0.05	0.58	16956	248	186	9.34	2	
J084617-465948	A2A	266.156	-2.397	0.008	0.31	0.09	0.64	7551	117	83	8.94	2	
J084756-481442	A2A	267.304	-2.963	0.015	2.63	0.49	0.73	8031	267	245	9.92	1	i
J084757-482429	A2A	267.432	-3.064	0.009	0.46	0.14	0.62	7957	103	48	9.15	2	
J084802-532009	B2C	271.298	-6.136	0.004	0.60	0.12	0.62	6659	222	212	9.11	1*	HyA0492, M
J084803-464727	A2A	266.185	-2.033	0.023	2.88	0.35	0.91	7899	268	210	9.94	1*	J0847-46
J084819-490900	A2A	268.049	-3.482	0.004	0.29	0.03	0.57	5442	304	163	8.62	2	i, w.comp
J084830-482325	A2A	267.477	-2.980	0.008	0.33	0.12	0.64	7626	168	153	8.97	1	
J084832-511634	B2D	269.730	-4.790	0.009	0.38	0.08	0.54	17404	123	84	9.75	1	
J084947-501715	B2B	269.085	-4.013	0.016	1.24	0.25	0.74	8298	208	175	9.62	1	i, w.comp? M, W
J085015-521726	B2D	270.690	-5.221	0.010	0.37	0.08	0.64	8796	132	62	9.15	1	
J085018-533452	B2C	271.702	-6.028	0.007	0.50	0.05	0.58	4027	117	97	8.60	1	
J085023-524635	B2C	271.082	-5.512	0.008	0.69	0.06	0.61	6820	125	102	9.19	1*	
J085122-491543	B2B	268.452	-3.166	0.011	0.40	0.08	0.78	19648	398	165	9.88	2	B=40'', e
J085133-425549	A1D	263.589	0.891	0.010	0.88	0.25	0.76	15958	347	294	10.04	1!	
J085154-502903	B2D	269.452	-3.877	0.008	0.80	0.21	0.79	7227	198	97	9.31	1*	i
J085235-494015	B2B	268.894	-3.274	0.029	2.69	0.09	0.66	2775	67	50	9.00	1	J0852-49
J085250-420600	A1D	263.100	1.603	0.021	3.38	0.27	0.66	3041	274	220	9.18	1	
J085342-434124	A1D	264.422	0.705	0.016	0.84	0.25	1.10	5429	108	60	9.08	1!	e
J085354-422241	A1D	263.441	1.577	0.018	1.76	0.29	0.62	5045	127	127	9.34	1	
J085410-431904	A1D	264.192	1.009	0.014	0.86	0.17	0.86	7071	356	117	9.32	1	i
J085431-544643	B2C	273.028	-6.309	0.014	1.68	0.13	0.86	2721	98	52	8.78	1	HyA0682
J085432-420511	A1D	263.292	1.853	0.009	0.47	0.09	0.55	17463	148	105	9.85	1	
J085450-420607	A1D	263.340	1.885	0.009	0.68	0.12	0.68	5034	375	126	8.92	2	B=45''
J085457-505011	B2D	270.032	-3.732	0.017	1.03	0.21	1.07	11461	133	24	9.82	2*	B=40'', e
J085457-501526	B2B	269.588	-3.359	0.004	0.19	0.05	0.52	11913	202	44	9.12	2	w.comp (J085529-501632)
J085458-545745	B2C	273.212	-6.377	0.010	1.55	0.16	0.76	3970	224	128	9.07	1	HyA0695, BL, W
J085505-423841	A1D	263.784	1.570	0.009	0.50	0.10	0.65	11475	498	302	9.51	1	
J085515-514628	B2D	270.783	-4.299	0.009	0.41	0.09	0.59	7449	68	50	9.04	1	
J085523-500345	B2B	269.484	-3.179	0.083	8.66	0.30	0.69	1605	96	58	9.03	1	J0855-50, H, Z
J085529-501632	B2B	269.658	-3.304	0.007	0.22	0.04	0.57	12000	54	30	9.19	1	w.comp (J085457-501526)
J085537-412353	A1D	262.897	2.452	0.014	2.39	0.22	0.67	5650	292	257	9.57	1	
J085539-513802	B2D	270.715	-4.161	0.008	0.32	0.09	0.72	7178	221	178	8.91	1	
J085539-415501	A1D	263.298	2.122	0.011	0.63	0.19	0.62	16126	238	184	9.91	1	i, M, W
J085546-540354	B2C	272.594	-5.712	0.008	0.50	0.10	0.64	12725	397	349	9.60	1	HyA0713, M, W
J085557-502526	B2B	269.819	-3.345	0.016	1.88	0.40	0.64	4187	210	178	9.20	1	
J085602-493555	B2B	269.197	-2.800	0.005	0.65	0.08	0.61	17182	485	110	9.98	1	BL
J085604-550359	B2C	273.393	-6.323	0.006	0.87	0.21	0.79	6357	221	180	9.23	2	HyA0718, M
J085638-414823	A1D	263.331	2.331	0.011	0.84	0.15	0.57	15373	209	148	9.99	1	

* Detected by the overlapping region of the adjacent mosaic.

** Detected by the overlapping region of two or more adjacent mosaics.

! Detected by the overlapping region between Vela-H i and Vela-SMGPS.

Table ?? continued

Name J2000 (1)	Mosaic TXX (2)	l deg (3)	b deg (4)	S_{peak} Jy (5)	S_{int} Jy km s $^{-1}$ (6)	ε_s Jy km s $^{-1}$ (7)	RMS mJy beam $^{-1}$ (8)	V_{hel} km s $^{-1}$ (9)	w_{20} km s $^{-1}$ (10)	w_{50} km s $^{-1}$ (11)	M_{HI} $\log(M_{\text{HI}}/\text{M}_\odot)$ (12)	Flag 1/2 (13)	Note (14)
J085638-483633	B2B	268.507	-2.083	0.024	6.37	0.32	0.86	2633	295	256	9.33	1	J0856-48, w.comp (J085659-483135), I, M, W, Z
J085648-513820	B2D	270.834	-4.029	0.019	3.11	0.58	0.79	7391	509	462	9.92	2*	i, M, W
J085649-535831	B2C	272.624	-5.537	0.008	0.66	0.07	0.53	12709	192	109	9.72	1	HyA0739, W
J085653-512553	B2D	270.684	-3.884	0.015	1.85	0.36	0.81	12450	346	303	10.15	1*	i, I
J085657-512123	B2B	270.633	-3.828	0.005	0.36	0.06	0.58	8345	158	113	9.09	1	
J085658-483215	B2B	268.488	-1.996	0.013	0.82	0.22	0.93	2881	360	97	8.52	2	i, w.comp (J085638-483633)
J085745-510932	B2B	270.564	-3.605	0.009	0.78	0.16	0.70	8465	285	237	9.44	1	w.comp (J085833-510958)
J085754-535234	B2C	272.652	-5.351	0.018	2.24	0.21	0.64	5992	175	129	9.59	1	HyA0764, M, W
J085758-432329	A1D	264.695	1.487	0.019	1.55	0.34	0.74	7882	371	296	9.67	2	BL
J085812-423228	A1D	264.078	2.074	0.008	0.32	0.07	0.54	2949	103	63	8.12	1	J0858-42, w.comp (J085838-423157), Z
J085816-443146	A1C	265.593	0.785	0.009	0.65	0.18	0.81	11153	292	180	9.60	1	e
J085826-554530	C2D	274.143	-6.512	0.005	0.16	0.09	0.56	17809	270	76	9.41	1	
J085829-554255	C2D	274.115	-6.479	0.010	0.48	0.08	0.54	10051	75	36	9.38	1	HyA0786, W
J085833-510958	B2B	270.651	-3.514	0.007	0.42	0.08	0.52	8291	223	127	9.15	1	w.comp (J085745-510936)
J085838-423157	A1D	264.124	2.141	0.014	3.45	0.33	0.66	2708	673	621	9.10	1	w.comps (one is J085812-423228), M, W
J085840-421627	A1D	263.932	2.314	0.008	0.24	0.06	0.54	2867	103	64	7.98	1	
J085840-421208	A1D	263.878	2.361	0.016	2.97	0.22	0.65	4665	253	222	9.50	1	M, W
J085842-503744	B2B	270.260	-3.145	0.008	0.57	0.11	0.59	8055	321	237	9.25	1	w.comp (J085900-503411)
J085849-552012	C2D	273.856	-6.198	0.006	0.78	0.13	0.65	6254	171	125	9.17	1	HyA0795, M, W
J085900-503411	B2B	270.247	-3.070	0.007	1.41	0.15	0.53	8206	316	261	9.67	1	w.comp (J085842-503744)
J085910-515620	B2A	271.302	-3.945	0.009	1.11	0.17	0.66	7544	348	316	9.49	1*	i, w.comp (J085925-515552), I, M, W
J085925-515552	B2A	271.320	-3.912	0.005	0.24	0.09	0.55	7316	139	92	8.79	1*	w.comp (J085910-515620)
J085929-525127	B2C	272.030	-4.509	0.012	3.17	0.23	0.61	4861	310	234	9.56	1*	J0859-52, HyA0808, w.comp (J085938-524534), I, M, W, Z
J085931-500000	B2B	269.869	-2.635	0.010	0.65	0.09	0.51	8031	269	231	9.31	1	i
J085934-422920	A1D	264.204	2.299	0.005	0.32	0.09	0.59	2734	112	64	8.07	1	
J085935-532320	B2C	272.445	-4.844	0.005	0.79	0.10	0.58	9434	252	121	9.54	1	HyA0815, w.comp (J090023-532350), M, W
J085938-524534	B2C	271.972	-4.427	0.014	1.42	0.11	0.62	4829	128	78	9.21	1*	J0859-52, w.comp (J085929-525127)
J085958-502144	B2B	270.190	-2.818	0.013	1.13	0.37	0.58	8150	314	229	9.56	1	
J090006-515835	B2A	271.424	-3.862	0.005	0.59	0.08	0.56	12736	367	354	9.67	1	M, W
J090013-433755	A1D	265.144	1.638	0.024	2.92	0.33	0.61	4977	249	218	9.55	1*	
J090020-495618	B2B	269.908	-2.496	0.007	0.15	0.03	0.67	22840	604	468	9.59	2	
J090023-532350	B2C	272.528	-4.760	0.015	1.94	0.15	0.63	9259	122	104	9.91	1	J0900-53, w.comp (J085935-532320)
J090051-523754	B2C	271.996	-4.204	0.010	1.02	0.30	0.71	10112	528	473	9.71	1*	
J090103-444214	A1C	266.050	1.045	0.010	0.60	0.07	0.60	10071	107	68	9.48	2	e
J090120-534343	B2C	272.873	-4.870	0.005	0.82	0.15	0.54	21938	425	404	10.30	2	HyA0857
J090143-453114	A1C	266.740	0.593	0.021	1.22	0.31	1.26	7662	157	127	9.54	1!	J0901-45, e
J090143-521908	B2A	271.846	-3.899	0.007	1.59	0.10	0.62	7342	320	251	9.62	1*	
J090145-411432	A1D	263.532	3.426	0.017	3.31	0.25	0.59	5112	267	233	9.62	1*	J0901-41, M, W, Z
J090151-415637	A1D	264.070	2.975	0.006	0.24	0.04	0.50	4809	304	173	8.43	2	i
J090159-443444	A1C	266.066	1.252	0.017	1.76	0.38	0.69	5040	200	166	9.33	1	i
J090201-400708	A1B	262.720	4.206	0.107	14.61	0.47	0.97	1636	112	80	9.28	1	J0902-40, H
J090213-560020	C2D	274.680	-6.272	0.007	0.28	0.06	0.51	13030	62	33	9.37	1	
J090220-413039	A1D	263.805	3.329	0.009	0.40	0.13	0.56	4901	305	41	8.67	1	w.comp (J090239-413505)
J090239-534419	B2C	273.009	-4.731	0.008	0.93	0.18	0.61	7170	254	233	9.37	1	J0902-53, HyA0895, M, Z
J090239-413505	A1D	263.902	3.327	0.011	1.35	0.64	0.64	5221	494	444	9.25	2*	Vel2067, w.comp (J090220-413038)
J090245-532626	B2C	272.794	-4.523	0.005	1.06	0.25	0.59	12615	249	215	9.92	1	
J090247-540548	B2C	273.292	-4.952	0.009	0.76	0.09	0.55	7152	139	71	9.28	1	
J090249-411213	A1B	263.636	3.602	0.014	0.78	0.16	0.61	5235	169	151	9.02	1*	i
J090258-540842	B2C	273.345	-4.965	0.007	1.91	0.29	0.66	9547	453	436	9.93	2	

* Detected by the overlapping region of the adjacent mosaic.

** Detected by the overlapping region of two or more adjacent mosaics.

! Detected by the overlapping region between Vela-H α and Vela-SMGPS.

Table ?? continued

Name J2000 (1)	Mosaic TXX (2)	l deg (3)	b deg (4)	S_{peak} Jy (5)	S_{int} Jy km s $^{-1}$ (6)	ε_s Jy km s $^{-1}$ (7)	RMS mJy beam $^{-1}$ (8)	V_{hel} km s $^{-1}$ (9)	w_{20} km s $^{-1}$ (10)	w_{50} km s $^{-1}$ (11)	M_{HI} $\log(M_{\text{HI}}/\text{M}_\odot)$ (12)	Flag 1/2 (13)	Note (14)
J090311-451400	A1C	266.697	0.978	0.035	6.60	0.49	0.76	2714	230	186	9.37	1!	J0903-45, Z
J090312-413525	A1D	263.974	3.400	0.010	0.53	0.14	0.66	4676	271	221	8.75	1	
J090313-411719	A1D	263.748	3.601	0.013	1.21	0.19	0.63	4578	128	109	9.09	1*	i, Part of J090323-411816 seen in the spectrum
J090314-523746	B2C	272.232	-3.932	0.018	3.71	0.40	0.84	7307	291	185	9.98	1*	J0903-52, i, M
J090320-561034	C2D	274.912	-6.268	0.006	0.48	0.10	0.62	13434	325	50	9.63	1	w_{20} unc.
J090323-411817	A1B	263.782	3.614	0.098	8.11	0.28	0.71	5460	110	77	10.07	1*	J0903-41, M, W, Z
J090346-532756	B2C	272.914	-4.426	0.011	1.14	0.08	0.56	7150	168	78	9.45	1*	J0903-53, i, w.comp (J090422-533654)
J090351-561754	C2D	275.053	-6.294	0.009	0.96	0.27	0.60	10044	317	280	9.67	1	HyA0936, M, W
J090405-425928	A1D	265.130	2.590	0.009	0.35	0.07	0.65	20809	345	155	9.88	2	w.comp?
J090408-425648	A1D	265.102	2.625	0.010	0.61	0.12	0.58	9621	467	421	9.44	1	
J090408-521830	B2A	272.084	-3.615	0.006	0.59	0.06	0.57	7433	176	62	9.20	1	
J090422-533654	B2C	273.084	-4.459	0.009	0.66	0.07	0.54	7134	135	88	9.21	1	w.comp (J090346-532756)
J090424-451733	A1C	266.882	1.096	0.038	2.60	0.12	0.70	7207	102	54	9.82	1	J0904-45
J090437-551119	C2D	274.289	-5.478	0.009	0.28	0.06	0.52	10754	67	36	9.21	1	
J090440-550150	C2D	274.176	-5.367	0.006	0.50	0.10	0.55	9868	504	479	9.38	2	HyA0953, W
J090442-440703	A1C	266.043	1.921	0.012	0.55	0.05	0.52	5370	87	22	8.89	1	w.comp
J090447-511456	B2A	271.359	-2.835	0.012	2.69	0.49	0.61	17506	561	501	10.61	1*	
J090448-444154	A1C	266.488	1.546	0.025	4.43	0.23	0.68	7097	321	272	10.04	1	J0905-44, M, W, Z
J090451-562927	C2D	275.289	-6.319	0.009	1.49	0.30	0.62	12723	300	259	10.07	1	HyA0956, M, W
J090456-571027	C2D	275.812	-6.763	0.013	1.07	0.14	0.69	4250	157	121	8.97	1	
J090504-394956	A1B	262.891	4.831	0.014	0.95	0.18	0.69	4885	280	135	9.04	1	i
J090536-520228	B2A	272.034	-3.270	0.006	0.39	0.06	0.55	6986	172	143	8.97	2	BL
J090551-523805	B2A	272.502	-3.639	0.005	0.95	0.19	0.63	7183	349	333	9.38	1	M, W
J090553-552251	C2D	274.553	-5.472	0.008	0.66	0.13	0.60	9772	517	467	9.49	1	HyA0986, w.comp? M, W
J090555-445136	A1C	266.740	1.584	0.007	0.57	0.18	0.58	8686	175	158	9.32	1	i
J090601-445045	A1C	266.743	1.609	0.006	0.20	0.05	0.53	7130	108	71	8.69	1	
J090608-414057	A1B	264.408	3.746	0.010	0.34	0.10	0.55	8420	69	41	9.07	1	
J090615-415314	A1B	264.575	3.625	0.019	2.45	0.33	0.65	5208	189	153	9.51	1*	
J090631-504656	B2A	271.195	-2.320	0.007	0.49	0.14	0.50	17440	267	240	9.86	2*	
J090635-453313	A1C	267.334	1.206	0.006	0.37	0.04	0.56	14369	288	167	9.58	1	i
J090642-574013	C2C	276.345	-6.915	0.010	0.53	0.11	0.73	10019	125	75	9.42	2*	
J090643-394353	A1B	263.029	5.134	0.005	0.36	0.02	0.53	6157	216	127	8.83	2	
J090649-462651	A1C	268.022	0.634	0.015	1.13	0.33	1.16	7474	487	302	9.49	2!	e
J090653-414654	A1D	264.575	3.782	0.018	1.39	0.28	0.83	4707	352	281	9.17	1*	
J090703-410401	A1B	264.065	4.285	0.009	0.69	0.24	0.58	11478	388	301	9.65	1	Vel2181, i, w.comp, W
J090713-455618	A1C	267.692	1.028	0.007	0.29	0.09	0.72	18764	344	158	9.70	1	
J090724-405907	A1B	264.050	4.390	0.006	0.28	0.06	0.56	11446	237	123	9.26	1	
J090724-553647	C2D	274.872	-5.467	0.011	3.13	0.41	0.63	9931	377	325	10.18	1	BL, i, w.comp
J090732-424854	A1C	265.423	3.177	0.015	2.06	0.42	0.59	5106	220	178	9.41	1**	i
J090734-422612	A1D	265.147	3.436	0.020	1.28	0.26	0.63	2307	175	101	8.52	1**	J0907-42, BL
J090755-514521	B2A	272.064	-2.813	0.005	0.13	0.03	0.63	13114	223	112	9.05	2	
J090801-512641	B2A	271.845	-2.591	0.004	0.19	0.06	0.51	22866	320	285	9.70	2	
J090806-512512	B2A	271.836	-2.565	0.005	2.01	0.11	0.65	1701	121	81	8.45	1	
J090818-421248	A1D	265.073	3.686	0.009	0.61	0.21	0.62	9927	104	63	9.47	1*	BL
J090901-410310	A1B	264.306	4.569	0.005	0.41	0.04	0.49	11530	134	107	9.43	2	
J090928-404835	A1B	264.185	4.798	0.014	1.00	0.22	0.62	5047	108	78	9.09	1	
J090933-555527	C2D	275.307	-5.453	0.015	1.07	0.13	0.58	9841	107	40	9.70	1	
J090942-465303	B1D	268.679	0.704	0.020	0.58	0.12	0.93	6580	61	15	9.09	2	e
J091023-440319	A1C	266.688	2.717	0.011	0.81	0.15	0.57	7019	174	129	9.29	1	i, I

* Detected by the overlapping region of the adjacent mosaic.

** Detected by the overlapping region of two or more adjacent mosaics.

! Detected by the overlapping region between Vela-H i and Vela-SMGPS.

Table ?? continued

Name J2000 (1)	Mosaic TXX (2)	l deg (3)	b deg (4)	S_{peak} Jy (5)	S_{int} Jy km s $^{-1}$ (6)	ε_s Jy km s $^{-1}$ (7)	RMS mJy beam $^{-1}$ (8)	V_{hel} km s $^{-1}$ (9)	w_{20} km s $^{-1}$ (10)	w_{50} km s $^{-1}$ (11)	M_{HI} $\log(M_{\text{HI}}/\text{M}_\odot)$ (12)	Flag 1/2 (13)	Note (14)
J091025-534748	C2D	273.824	-3.918	0.012	0.27	0.05	0.80	23482	159	55	9.87	1	
J091034-514825	B2A	272.380	-2.547	0.002	0.97	0.19	0.61	1802	180	80	8.18	1	
J091035-462614	B1D	268.454	1.118	0.012	0.56	0.11	0.72	11803	96	25	9.58	2	
J091036-442654	A1C	267.002	2.478	0.019	1.94	0.10	0.59	1868	116	79	8.51	1	J0910-44
J091039-560311	C2D	275.507	-5.428	0.010	0.80	0.10	0.59	4140	120	84	8.82	1	HyA1086, W
J091044-425723	A1A	265.926	3.513	0.011	0.81	0.06	0.59	2899	162	140	8.52	1*	
J091105-553331	C2D	275.185	-5.046	0.008	2.50	0.24	0.60	10013	318	251	10.09	1	M
J091110-524939	B2A	273.190	-3.175	0.008	0.51	0.15	0.58	10193	277	177	9.42	1	
J091121-545029	C2D	274.684	-4.530	0.007	0.34	0.07	0.63	23924	153	119	9.99	1	
J091130-400058	A1B	263.863	5.620	0.015	1.00	0.19	0.56	16474	124	67	10.13	1	
J091130-401814	A1B	264.076	5.425	0.008	0.53	0.11	0.61	11316	280	210	9.52	1	w.comp
J091142-435457	A1C	266.746	2.984	0.016	1.12	0.12	0.59	7551	131	87	9.49	1	
J091154-530540	B2A	273.460	-3.278	0.004	0.54	0.19	0.61	5924	201	168	8.97	1	
J091156-443434	A1C	267.257	2.563	0.009	0.72	0.08	0.54	9389	197	144	9.49	1	w.comps (one is J091157-443307)
J091157-443307	A1C	267.243	2.583	0.009	0.30	0.07	0.52	9664	125	108	9.14	2	w.comp (J091156-443434)
J091209-534148	C2B	273.926	-3.663	0.032	1.56	0.14	0.76	4027	83	31	9.09	1*	J0912-53
J091230-455323	B1D	268.283	1.735	0.019	2.36	0.37	0.71	4763	170	152	9.41	1	J0912-45, i, Z
J091236-393130	A1B	263.646	6.108	0.015	1.30	0.21	0.63	6017	108	75	9.36	1	Vel2398, W
J091238-585018	C2C	277.743	-7.127	0.021	2.64	0.23	1.26	2904	230	172	9.03	1	HyA1125, I, H, M, W
J091240-404258	A1B	264.531	5.305	0.006	0.07	0.02	0.48	7995	167	70	8.36	2	
J091248-535228	C2B	274.121	-3.715	0.005	0.33	0.07	0.55	21116	405	337	9.87	2	M, W
J091314-514448	B2A	272.618	-2.206	0.027	2.05	0.37	0.73	10636	248	192	10.06	1	J0913-51, i
J091317-560313	C2D	275.760	-5.159	0.007	0.34	0.07	0.55	10592	287	246	9.27	2	
J091330-423533	A1A	266.007	4.131	0.008	1.14	0.21	0.58	22544	495	458	10.46	1	BL, w.comp?
J091402-393736	A1B	263.911	6.240	0.009	0.98	0.09	0.65	11364	224	80	9.79	1	
J091404-412613	A1B	265.239	5.003	0.006	0.28	0.06	0.54	20683	164	81	9.77	2	
J091406-514653	B2A	272.736	-2.132	0.017	1.69	0.53	0.72	5300	370	117	9.36	1	BL, i
J091407-571425	C2D	276.706	-5.890	0.017	1.79	0.10	0.77	10105	206	163	9.95	1*	
J091413-441509	A1C	267.303	3.083	0.004	0.23	0.05	0.47	9929	280	220	9.04	2	
J091429-422550	A1A	266.014	4.373	0.014	1.28	0.11	0.60	2973	114	90	8.74	1	i, w.comp
J091435-464755	B1D	269.190	1.370	0.006	0.27	0.06	0.55	19943	231	144	9.73	2	BL
J091454-515445	B2A	272.917	-2.133	0.008	1.76	0.33	0.59	20865	331	252	10.58	1	i
J091502-410342	A1A	265.090	5.392	0.011	0.26	0.05	0.69	14045	167	130	9.40	2	BL, e
J091504-444828	A1C	267.810	2.808	0.013	0.71	0.15	0.65	3776	129	82	8.69	1	
J091505-394119	A1B	264.097	6.345	0.005	0.56	0.19	0.64	11548	385	354	9.56	2	
J091515-515209	B2A	272.922	-2.065	0.008	0.26	0.05	0.71	19172	392	77	9.68	2	w ₂₀ unc.
J091518-542441	C2D	274.764	-3.820	0.017	2.84	0.47	1.01	9490	506	443	10.10	1*	B=40'', e, w.comps (one is J091526-542427)
J091520-574530	C2C	277.197	-6.128	0.005	0.36	0.06	0.49	16258	198	139	9.68	2	
J091524-474200	B1D	269.935	0.845	0.009	0.50	0.09	0.91	7294	128	71	9.12	1!	J0915-47
J091526-542427	C2B	274.774	-3.804	0.006	0.60	0.06	0.61	9369	251	187	9.41	1	w.comp (J091516-542459)
J091538-533735	C2B	274.230	-3.241	0.009	1.16	0.35	0.68	19373	375	337	10.33	1	B=50'', i?
J091543-563508	C2D	276.380	-5.281	0.011	0.27	0.08	0.53	13256	68	22	9.37	1*	
J091543-520743	B2A	273.160	-2.192	0.017	2.12	0.60	0.68	10358	514	296	10.05	1	i
J091548-574007	C2C	277.175	-6.021	0.005	0.45	0.13	0.51	16279	236	183	9.77	1	
J091549-543529	C2B	274.946	-3.891	0.045	6.49	0.18	0.69	4020	139	97	9.71	1*	J0916-54A, I, M, W, Z
J091549-432929	A1A	266.952	3.817	0.010	1.48	0.22	0.59	6882	317	260	9.53	1*	M, W
J091629-563035	C2D	276.399	-5.152	0.008	0.80	0.16	0.56	12966	259	219	9.82	1*	HyA1178, i, W
J091635-420320	A1A	266.013	4.915	0.011	0.66	0.12	0.57	4968	191	141	8.90	1	w.comp
J091643-542114	C2B	274.866	-3.631	0.031	9.74	0.54	0.75	4092	340	220	9.90	1*	J0916-54B, i, I

* Detected by the overlapping region of the adjacent mosaic.
** Detected by the overlapping region of two or more adjacent mosaics.
! Detected by the overlapping region between Vela-H α and Vela-SMGPS.

Table ?? continued

Name J2000 (1)	Mosaic TXX (2)	<i>l</i> deg (3)	<i>b</i> deg (4)	<i>S</i> _{peak} Jy (5)	<i>S</i> _{int} Jy km s ⁻¹ (6)	ε_s Jy km s ⁻¹ (7)	RMS mJy beam ⁻¹ (8)	<i>V</i> _{hel} km s ⁻¹ (9)	<i>w</i> ₂₀ km s ⁻¹ (10)	<i>w</i> ₅₀ km s ⁻¹ (11)	<i>M</i> _{HI} $\log(M_{\text{HI}}/\text{M}_{\odot})$ (12)	Flag 1/2 (13)	Note (14)
J091649-561557	C2D	276.254	-4.950	0.007	0.30	0.10	0.54	15278	171	156	9.53	2	
J091714-465110	B1D	269.543	1.658	0.007	0.71	0.15	0.58	9711	298	264	9.51	1	i
J091717-570146	C2C	276.850	-5.435	0.006	0.50	0.09	0.56	10053	174	115	9.39	2	
J091719-513705	B2A	272.965	-1.659	0.015	0.93	0.27	0.91	19086	223	163	10.23	2	BL
J091730-445551	B1D	268.198	3.032	0.013	1.12	0.16	0.75	5460	164	100	9.21	1	
J091730-532315	C2B	274.252	-2.875	0.093	19.66	0.50	0.80	941	203	169	8.92	1	J0917-53, I, H, M, Z
J091743-552857	C2D	275.777	-4.315	0.009	2.25	0.34	0.69	6913	344	277	9.72	1*	I, M, W
J091746-480948	B1C	270.543	0.805	0.045	5.58	0.69	0.94	3337	233	180	9.48	1*	J0917-48
J091805-551921	C2D	275.699	-4.166	0.008	0.46	0.09	0.61	9210	129	76	9.28	1	
J091807-564421	C2C	276.721	-5.150	0.007	1.47	0.15	0.56	20800	400	356	10.50	1*	
J091810-461317	B1D	269.203	2.213	0.009	0.33	0.07	0.50	23283	228	38	9.95	1	
J091821-553322	C2D	275.894	-4.301	0.013	0.65	0.06	0.63	17455	503	419	9.99	1	i
J091827-552618	C2D	275.819	-4.209	0.009	0.25	0.05	0.55	18492	94	32	9.63	2	
J091835-445257	B1D	268.298	3.204	0.006	0.41	0.14	0.65	10146	135	87	9.31	1	<i>w</i> ₂₀ unc.
J091856-471811	B1D	270.067	1.549	0.006	0.51	0.10	0.64	14332	370	341	9.71	1	i
J091858-475712	B1C	270.536	1.098	0.007	0.44	0.32	0.74	7251	317	227	9.05	1*	w.comp
J091913-481238	B1D	270.747	0.946	0.007	0.25	0.13	0.81	18733	339	66	9.63	1*	
J091915-565617	C2C	276.972	-5.179	0.007	0.78	0.09	0.55	21121	329	299	10.24	1	
J091925-571735	C2C	277.243	-5.411	0.007	0.63	0.10	0.57	10200	253	224	9.50	1	
J091925-550307	C2B	275.640	-3.840	0.005	0.62	0.16	0.65	6891	195	167	9.16	2*	
J091932-523006	C2B	273.834	-2.036	0.009	0.96	0.19	0.92	6865	263	226	9.34	1	e
J091932-474732	B1D	270.487	1.278	0.009	0.33	0.08	0.54	4681	108	76	8.55	1	
J091944-415805	A1A	266.359	5.394	0.005	0.29	0.03	0.54	7205	119	104	8.86	1	
J092021-553757	C2D	276.147	-4.154	0.013	1.60	0.19	0.62	12750	180	112	10.11	1**	
J092032-442511	B1B	268.211	3.775	0.060	9.02	0.70	0.77	2674	207	175	9.49	1*	J0920-44, H, Z
J092038-464502	B1D	269.880	2.144	0.021	1.44	0.22	0.62	4135	110	78	9.08	1	i, w.comp?
J092041-582429	C2C	278.161	-6.073	0.004	0.22	0.04	0.46	15299	176	135	9.41	2	
J092055-443055	B1D	268.328	3.756	0.006	0.23	0.05	0.75	17499	194	144	9.53	2	
J092057-472649	B1D	270.410	1.690	0.012	1.28	0.15	0.64	9455	258	218	9.75	1	i
J092100-531131	C2B	274.481	-2.365	0.010	0.98	0.28	0.66	13941	204	148	9.97	1	
J092101-431742	A1A	267.473	4.629	0.010	1.07	0.10	0.61	5119	163	128	9.13	1	
J092112-480819	B1D	270.929	1.230	0.007	0.24	0.02	0.69	7132	86	31	8.78	2	e, w.comp (J092120-480629)
J092112-412859	A1A	266.206	5.930	0.008	0.38	0.06	0.53	7218	128	98	8.98	1	
J092117-480701	B1C	270.924	1.256	0.032	3.85	0.17	0.64	7214	187	150	9.99	1*	J0921-48, i, w.comps (one is J092112-480819)
J092125-451625	B1D	268.928	3.282	0.016	0.96	0.09	0.57	9684	117	63	9.64	1*	i, w.comp
J092128-483240	B1C	271.248	0.975	0.007	0.38	0.04	0.58	9354	141	79	9.21	1	
J092136-485240	B1C	271.499	0.755	0.011	1.47	0.34	0.87	11237	312	274	9.96	1!	e, i
J092151-542733	C2B	275.465	-3.174	0.015	1.07	0.08	0.58	12677	159	115	9.93	1	M, W
J092151-474557	B1D	270.744	1.572	0.008	0.68	0.18	0.63	7187	180	104	9.23	1*	
J092156-535248	C2B	275.065	-2.755	0.010	0.86	0.22	0.66	14387	466	268	9.94	1	
J092216-443510	B1B	268.549	3.877	0.006	0.50	0.13	0.53	10964	257	233	9.47	2	
J092224-551619	C2B	276.096	-3.694	0.005	0.34	0.06	0.57	12754	208	175	9.43	1	
J092229-415719	A1A	266.712	5.766	0.011	0.78	0.08	0.67	7378	69	38	9.32	1	
J092232-592017	C2C	278.994	-6.558	0.006	0.96	0.13	0.73	6613	245	77	9.31	1	
J092237-474722	B1D	270.851	1.645	0.007	0.18	0.05	0.60	8177	255	176	8.77	1	e, M
J092238-412110	A1A	266.304	6.213	0.015	3.14	0.71	0.74	4881	197	165	9.56	1	Vel2604, BL, M, W
J092251-473644	B1C	270.755	1.800	0.008	1.20	0.23	0.65	7497	262	241	9.52	1*	
J092256-570838	C2C	277.473	-4.969	0.011	3.07	0.16	0.64	6770	347	311	9.83	1	HyA1272, w.comp (J092313-570116), I, M, W
J092306-454420	B1D	269.466	3.161	0.006	0.37	0.09	0.47	23416	254	199	10.01	1	Face-on galaxy with hole at the centre?

* Detected by the overlapping region of the adjacent mosaic.

** Detected by the overlapping region of two or more adjacent mosaics.

! Detected by the overlapping region between Vela-H α and Vela-SMGPS.

Table ?? continued

Name J2000 (1)	Mosaic TXX (2)	l deg (3)	b deg (4)	S_{peak} Jy (5)	S_{int} Jy km s $^{-1}$ (6)	ε_s Jy km s $^{-1}$ (7)	RMS mJy beam $^{-1}$ (8)	V_{hel} km s $^{-1}$ (9)	w_{20} km s $^{-1}$ (10)	w_{50} km s $^{-1}$ (11)	M_{HI} $\log(M_{\text{HI}}/\text{M}_\odot)$ (12)	Flag 1/2 (13)	Note (14)
J092313-570116	C2C	277.414	-4.854	0.006	0.80	0.09	0.58	6736	212	103	9.24	1	w.comp (J092256-570838), I
J092323-555250	C2A	276.625	-4.028	0.005	0.26	0.08	0.61	9183	190	134	9.03	2	w.comp (J092329-555401)
J092328-555407	C2B	276.649	-4.034	0.009	0.52	0.09	0.67	9416	146	75	9.35	1*	i, w.comp (J092323-555250)
J092334-424542	A1A	267.426	5.336	0.022	5.66	0.34	0.70	2990	191	143	9.39	1	J0923-42, Vel2630, H, M, W, Z
J092335-442426	B1B	268.588	4.168	0.007	0.69	0.10	0.56	11037	208	170	9.62	2	
J092342-421632	A1A	267.100	5.699	0.005	0.37	0.08	0.55	10058	380	252	9.27	1	
J092343-415245	A1A	266.821	5.982	0.008	0.44	0.09	0.60	9805	215	161	9.31	2	Vel2637, i, M, W
J092434-585501	C2C	278.882	-6.075	0.005	0.42	0.07	0.64	6673	172	106	8.96	2	
J092438-475217	B1C	271.149	1.824	0.008	0.55	0.04	0.57	7119	119	80	9.13	1	
J092441-411533	A1A	266.512	6.551	0.013	2.18	0.15	0.91	4678	216	172	9.36	2	Vel2667, BL, e
J092443-542654	C2B	275.755	-2.873	0.007	0.34	0.08	0.54	4079	116	82	8.44	1	
J092455-582741	C2C	278.593	-5.719	0.006	0.53	0.14	0.57	15187	173	97	9.78	2	
J092459-452538	B1B	269.483	3.615	0.011	0.56	0.05	0.57	9727	169	132	9.42	1	
J092514-583640	C2C	278.728	-5.796	0.010	0.59	0.05	0.57	9886	110	76	9.45	1	
J092516-462723	B1D	270.239	2.914	0.013	0.90	0.21	0.61	21985	191	103	10.34	1	BL
J092517-593015	D2D	279.362	-6.429	0.004	2.04	0.24	0.83	2990	239	199	8.95	2	HyA1312, M, W
J092524-475223	B1C	271.244	1.913	0.005	0.62	0.13	0.60	11403	280	251	9.60	1	
J092524-455049	B1D	269.830	3.366	0.007	0.41	0.08	0.60	15241	165	76	9.67	1	
J092540-580342	C2C	278.383	-5.364	0.009	0.96	0.13	0.59	10428	175	137	9.71	1	w.comp (J092622-580706)
J092542-464455	B1D	270.496	2.755	0.012	0.51	0.20	0.63	6423	186	129	9.01	1	i
J092548-432724	B1B	268.207	5.126	0.010	1.15	0.26	0.77	5060	188	99	9.15	1	i
J092555-413108	A1A	266.861	6.527	0.017	2.61	0.84	1.07	5036	234	187	9.51	1	Vel2695, BL, e, M, W
J092605-415016	A1A	267.106	6.320	0.028	4.86	0.59	0.81	4687	161	136	9.71	1	H, M, W
J092607-572454	C2C	277.973	-4.859	0.012	1.20	0.15	0.59	6803	209	179	9.43	1	
J092620-603655	D2D	280.240	-7.130	0.014	6.71	0.27	1.54	2108	137	84	9.16	2	e
J092622-580706	C2C	278.488	-5.341	0.013	3.42	0.21	0.65	10218	622	494	10.24	1	HyA1326, Edge-on Sp, w.comp (J092540-580342), M, W
J092627-454534	B1B	269.900	3.556	0.009	0.50	0.10	0.59	15194	177	44	9.75	2	B=40"
J092628-570548	C2C	277.783	-4.599	0.007	0.34	0.08	0.51	12304	163	122	9.40	1	w.comp
J092638-552538	C2A	276.637	-3.382	0.008	0.72	0.19	0.61	9369	155	92	9.49	1*	i, w.comp
J092711-414646	A1A	267.214	6.506	0.011	1.96	0.34	0.89	2624	164	134	8.81	1	BL, e
J092715-495527	B1C	272.887	0.649	0.029	4.82	0.49	1.14	4537	229	196	9.68	1!	J0927-49, e, i
J092730-542319	C2B	276.004	-2.549	0.007	0.21	0.04	0.53	20851	80	59	9.66	1	
J092731-604613	D2D	280.453	-7.140	0.020	3.48	0.19	1.41	2139	463	390	8.88	1	HyA1353, e, I, M, W
J092737-433208	B1B	268.500	5.300	0.009	0.42	0.08	0.62	16410	278	157	9.74	1	w.comp
J092739-424854	A1A	268.001	5.822	0.012	1.58	0.21	0.81	5001	162	143	9.28	1	e
J092742-490255	B1C	272.335	1.332	0.004	0.26	0.05	0.59	11278	108	73	9.21	2	
J092746-555840	C2A	277.134	-3.669	0.156	32.77	0.19	0.67	1147	179	126	9.32	1*	J0927-55, H
J092751-474934	B1C	271.508	2.233	0.010	0.68	0.09	0.57	7070	165	148	9.22	1	
J092757-450531	B1B	269.625	4.219	0.006	0.32	0.03	0.47	19457	473	371	9.79	2	
J092759-565922	C2C	277.858	-4.378	0.010	3.00	0.14	0.58	12196	367	263	10.34	1*	i
J092805-563236	C2A	277.559	-4.046	0.024	4.55	0.22	0.68	4587	194	164	9.67	1*	J0928-56, M, W, Z
J092809-482541	B1C	271.960	1.832	0.028	1.57	0.11	0.63	7152	85	23	9.59	1	J0927-48, i, w.comp?
J092826-562601	C2A	277.518	-3.933	0.005	0.45	0.12	0.59	10670	178	178	9.40	2	
J092851-422821	A1A	267.923	6.222	0.009	0.66	0.13	0.67	16657	205	163	9.96	1	Vel2728, e, i, M
J092902-421808	A1A	267.828	6.368	0.017	5.54	1.01	0.98	6558	514	437	10.06	1	Vel2731, M, W
J092924-422309	A1A	267.937	6.355	0.019	4.51	1.35	0.97	6739	314	300	10.00	1	Vel2736, M, W
J092938-481954	B1C	272.072	2.071	0.016	3.15	0.46	0.68	7349	326	300	9.92	1	J0929-48, I, M, W, Z
J092953-440308	B1B	269.154	5.208	0.006	0.80	0.09	0.54	5307	263	224	9.04	1	
J093006-454649	B1D	270.374	3.979	0.012	0.40	0.08	0.90	8351	119	104	9.13	2	e

* Detected by the overlapping region of the adjacent mosaic.

** Detected by the overlapping region of two or more adjacent mosaics.

! Detected by the overlapping region between Vela-H α and Vela-SMGPS.

Table ?? continued

Name J2000 (1)	Mosaic TXX (2)	l deg (3)	b deg (4)	S_{peak} Jy (5)	S_{int} Jy km s $^{-1}$ (6)	ε_s Jy km s $^{-1}$ (7)	RMS mJy beam $^{-1}$ (8)	V_{hel} km s $^{-1}$ (9)	w_{20} km s $^{-1}$ (10)	w_{50} km s $^{-1}$ (11)	M_{HI} $\log(M_{\text{HI}}/\text{M}_\odot)$ (12)	Flag 1/2 (13)	Note (14)
J093007-432510	B1B	268.747	5.696	0.019	3.33	0.68	0.61	5088	316	274	9.62	1	Vel2740, M, W
J093019-545215	C2A	276.633	-2.617	0.012	1.63	0.06	0.61	3903	206	158	9.08	1*	
J093029-453759	B1B	270.323	4.134	0.011	2.04	0.24	0.60	11915	421	355	10.15	1	i
J093048-555515	C2A	277.403	-3.335	0.023	2.29	0.22	0.63	2740	139	79	8.92	1	J0930-55
J093052-580322	C2C	278.876	-4.885	0.013	1.74	0.31	0.72	10283	537	341	9.95	1	w.comp
J093100-423205	B1B	268.254	6.450	0.010	0.54	0.11	0.98	17121	399	242	9.89	2	e, i, w.comp
J093109-594757	D2D	280.105	-6.128	0.002	2.77	0.22	0.73	2958	227	173	9.07	1	HyA1419, w. comp (J093235-595336), M
J093111-435653	B1B	269.253	5.445	0.013	0.69	0.15	0.57	5099	128	73	8.94	1	J0931-43? i
J093116-590703	D2D	279.645	-5.622	0.007	0.79	0.14	0.64	2279	154	108	8.29	1	
J093116-434633	B1B	269.147	5.581	0.019	1.05	0.15	0.55	5134	101	57	9.13	1	J0931-43?
J093122-424532	B1B	268.458	6.333	0.006	0.37	0.08	0.68	14770	166	116	9.60	1	
J093131-542115	C2B	276.406	-2.122	0.008	0.37	0.09	0.63	9008	155	115	9.17	1	
J093202-473740	B1C	271.884	2.860	0.006	0.69	0.15	0.54	14420	208	164	9.85	1	HyA1426, I, M, W
J093212-432439	B1B	269.018	5.961	0.008	0.59	0.11	0.55	14819	272	232	9.80	2	
J093219-435317	B1B	269.362	5.628	0.014	1.20	0.14	0.55	4981	115	97	9.16	1	
J093234-572803	C2C	278.639	-4.299	0.009	0.88	0.10	0.65	9441	207	165	9.58	1*	
J093235-595336	D2D	280.301	-6.073	0.003	1.91	0.12	0.74	2992	231	186	8.92	2	w.comp (J093109-594757)
J093246-434859	B1B	269.372	5.736	0.011	1.09	0.16	0.52	5226	212	155	9.16	1	Vel2765, i, M, W \
J093255-545229	C2A	276.910	-2.364	0.019	0.66	0.07	0.63	1005	64	20	7.51	2	
J093301-551444	C2A	277.171	-2.628	0.007	0.44	0.13	0.61	13804	213	166	9.62	1	
J093308-484539	B1C	272.789	2.153	0.013	1.51	0.36	0.65	7369	186	119	9.60	1	
J093313-435642	B1B	269.519	5.696	0.013	1.98	0.53	0.62	5407	281	234	9.45	1	i
J093316-491347	B1C	273.122	1.822	0.007	0.43	0.09	0.80	7352	255	198	9.06	1	
J093322-434524	B1B	269.410	5.853	0.006	0.21	0.05	0.47	16351	141	109	9.44	1	
J093324-501758	C1D	273.862	1.049	0.010	1.32	0.27	0.69	7358	250	196	9.54	1	
J093346-441248	B1B	269.776	5.567	0.004	0.55	0.05	0.47	14636	297	253	9.77	1	
J093348-434324	B1B	269.446	5.931	0.012	0.57	0.11	0.55	5226	73	54	8.88	1	w.comp?
J093356-462737	B1A	271.326	3.935	0.009	1.03	0.33	0.61	11489	392	347	9.83	1	
J093356-552033	C2A	277.334	-2.610	0.012	1.32	0.10	0.62	11209	220	199	9.91	1	
J093413-611653	D2D	281.402	-6.952	0.007	2.96	0.52	1.18	2629	205	147	8.99	1*	HyA1464, e, w. comp, \hi{} LSB with a hole at the centre? I, H, M
J093420-541323	C2A	276.620	-1.746	0.011	0.23	0.05	0.94	16316	142	37	9.48	2	
J093424-481552	B1C	272.608	2.661	0.006	0.42	0.08	0.53	7322	128	74	9.04	1	i
J093428-442842	B1B	270.049	5.457	0.014	0.86	0.14	0.53	14631	134	62	9.96	1	i, w.comp
J093454-555439	C2A	277.819	-2.937	0.017	4.70	0.14	0.59	4020	232	202	9.57	1	J0934-55
J093458-564632	C2A	278.409	-3.571	0.016	3.22	0.15	0.65	9342	296	251	10.14	1	I, M, W
J093507-471453	B1A	272.010	3.493	0.006	0.43	0.09	0.59	11378	123	94	9.44	2*	e
J093516-483019	B1C	272.877	2.580	0.008	1.00	0.10	0.56	17676	219	162	10.19	1	BL, i
J093519-492903	C1D	273.541	1.860	0.009	0.58	0.15	0.79	7068	138	87	9.15	1	
J093522-434617	B1B	269.688	6.088	0.010	0.60	0.12	0.62	11617	385	239	9.60	1	i, w.comp
J093529-434939	B1B	269.743	6.061	0.010	0.85	0.17	0.53	19917	367	318	10.22	1	i, I
J093533-444840	B1B	270.418	5.343	0.008	0.40	0.08	0.49	13694	93	39	9.57	1	i
J093548-470259	B1A	271.962	3.717	0.006	0.28	0.05	0.52	14889	175	78	9.48	2	
J093606-453530	B1A	271.018	4.831	0.012	1.31	0.39	0.61	17529	301	261	10.30	1*	i
J093617-433619	B1B	269.698	6.321	0.012	0.80	0.16	0.60	11667	172	156	9.73	1	M, W
J093635-463105	B1A	271.704	4.201	0.008	0.39	0.08	0.50	6860	148	106	8.95	1	
J093639-543719	C2A	277.137	-1.815	0.080	9.43	0.38	0.94	2747	162	91	9.54	1!	J0936-54, i, I, M, W, Z
J093639-495935	C1D	274.042	1.627	0.011	0.42	0.06	0.59	6955	164	28	8.99	1	
J093659-605552	D2D	281.411	-6.468	-0.000	3.38	0.14	0.76	2811	297	279	9.11	1*	HyA1492, I, H, M, W
J093700-493802	C1D	273.844	1.932	0.007	0.33	0.07	0.57	20667	216	177	9.84	1	

* Detected by the overlapping region of the adjacent mosaic.

** Detected by the overlapping region of two or more adjacent mosaics.

! Detected by the overlapping region between Vela-H i and Vela-SMGPS.

Table ?? continued

Name J2000 (1)	Mosaic TXX (2)	l deg (3)	b deg (4)	S_{peak} Jy (5)	S_{int} Jy km s $^{-1}$ (6)	ε_s Jy km s $^{-1}$ (7)	RMS mJy beam $^{-1}$ (8)	V_{hel} km s $^{-1}$ (9)	w_{20} km s $^{-1}$ (10)	w_{50} km s $^{-1}$ (11)	M_{HI} $\log(M_{\text{HI}}/\text{M}_\odot)$ (12)	Flag 1/2 (13)	Note (14)
J093701-455420	B1A	271.348	4.705	0.009	1.69	0.22	0.63	6776	268	225	9.58	1	i? w.comp?
J093708-480214	B1C	272.792	3.134	0.009	0.58	0.06	0.58	3276	153	93	8.48	1	
J093708-452247	B1A	271.010	5.110	0.007	0.25	0.04	0.50	8019	78	57	8.89	1	
J093723-465844	B1A	272.115	3.949	0.008	0.24	0.07	0.54	3943	169	44	8.25	2	
J093730-601851	D2D	281.041	-5.969	0.009	2.78	0.14	0.65	3089	201	171	9.11	1	HyA1499, M, W
J093730-462733	B1A	271.782	4.350	0.006	0.44	0.09	0.55	18533	354	316	9.87	1	i, w.comps, M, W
J093730-563016	C2A	278.487	-3.135	0.007	0.39	0.08	0.61	2257	93	50	7.98	1	
J093732-452834	B1A	271.126	5.085	0.005	0.23	0.02	0.51	17605	100	45	9.55	2	
J093732-560516	C2A	278.211	-2.821	0.009	1.87	0.22	0.66	9181	235	212	9.89	1	
J093733-465720	B1A	272.121	3.986	0.009	0.75	0.21	0.53	17868	211	170	10.07	1	i, w.comp
J093739-503052	C1D	274.508	1.345	0.012	0.85	0.05	0.53	8367	167	132	9.47	1	
J093754-444942	B1B	270.740	5.610	0.005	0.12	0.03	0.63	11507	240	194	8.91	1	
J093827-614914	D2D	282.142	-7.011	0.018	1.54	0.14	1.96	2870	311	285	8.79	2	e
J093828-614951	D2C	282.151	-7.016	0.015	4.64	0.21	1.19	2921	309	267	9.28	1	HyA1517, e, I, M, W
J093838-453650	B1A	271.363	5.111	0.007	0.19	0.05	0.47	17347	67	34	9.45	1	
J093908-584728	D2D	280.176	-4.695	0.009	0.87	0.07	0.63	4263	240	60	8.88	1	
J093916-465115	B1A	270.740	5.610	0.005	0.12	0.03	0.63	11507	240	194	8.91	1	
J093923-504125	C1D	274.832	1.397	0.010	1.17	0.26	0.61	8396	246	206	9.61	1	w.comp (J093928-504343)
J093924-564737	C2A	278.874	-3.178	0.008	0.74	0.15	0.79	12153	548	490	9.73	1	M, W
J093928-504343	C1D	274.867	1.377	0.012	0.55	0.16	0.60	8298	101	38	9.26	1	w.comp (J093923-504125)
J093945-442406	B1A	270.701	6.148	0.007	0.26	0.04	0.55	17305	65	36	9.59	1	e
J093949-564551	C2A	278.896	-3.119	0.019	1.01	0.08	0.72	2964	114	52	8.63	1	J0939-56
J093956-451208	B1A	271.260	5.571	0.005	0.35	0.06	0.45	17903	214	171	9.75	1	
J094037-443236	B1A	270.912	6.144	0.007	0.43	0.09	0.57	21598	300	271	10.00	1	
J094040-593844	D2D	280.891	-5.206	0.018	1.03	0.15	0.68	2354	86	22	8.44	1	J0940-59, H, Z
J094044-493138	C1D	274.226	2.413	0.009	0.92	0.10	0.54	12073	175	123	9.82	1	
J094056-603008	D2D	281.486	-5.826	0.011	2.85	0.11	0.75	3108	120	38	9.12	1*	B=40''
J094059-473009	B1A	272.922	3.964	0.006	0.22	0.04	0.62	11234	475	434	9.13	2	
J094111-580103	D2D	279.864	-3.938	0.009	0.42	0.08	0.73	10227	111	72	9.33	2*	
J094123-485552	C1D	273.913	2.931	0.006	0.31	0.08	0.56	7859	129	110	8.97	1	i
J094142-612541	D2C	282.144	-6.484	0.005	0.87	0.11	0.62	11198	308	291	9.73	1	HyA1557, M, W
J094141-493309	C1D	274.358	2.494	0.011	0.57	0.12	0.55	11895	108	68	9.59	1	HyA1554, M, W
J094143-604756	D2C	281.754	-5.987	0.004	3.48	0.30	0.75	3128	265	261	9.22	1*	HyA1561, I, M, W
J094151-552939	C2A	278.274	-1.975	0.009	0.52	0.11	0.75	7828	272	113	9.19	2	B=40'', i, w.comp
J094202-560800	C2A	278.713	-2.441	0.006	0.15	0.05	0.55	2706	77	30	7.73	2	BL
J094211-603558	D2C	281.665	-5.799	0.006	1.68	0.05	0.64	3173	164	150	8.91	1*	HyA1568, W
J094233-480734	C1D	273.531	3.666	0.015	0.82	0.15	0.66	17771	206	156	10.11	2	
J094235-470412	B1A	272.841	4.467	0.016	1.55	0.42	0.62	16951	211	170	10.34	1	M, W
J094238-485409	C1D	274.050	3.088	0.011	1.27	0.42	0.62	7879	288	199	9.59	1	
J094252-601728	D2C	281.526	-5.511	0.011	0.59	0.18	0.65	4570	170	66	8.78	2*	Face-on?
J094300-601953	D2C	281.565	-5.530	0.011	2.48	0.18	0.75	2833	127	116	8.98	1*	
J094303-570732	D2B	279.467	-3.101	0.006	0.33	0.04	0.54	10708	79	41	9.27	1	
J094313-520204	C1C	276.165	0.775	0.009	0.31	0.06	0.84	13812	507	446	9.46	2	
J094317-452103	B1A	271.803	5.846	0.013	2.20	0.12	0.54	5348	247	216	9.49	1	Vel2962
J094326-453013	B1A	271.923	5.748	0.008	0.70	0.21	0.56	12073	247	181	9.70	1	Vel2966
J094333-452150	B1A	271.847	5.867	0.006	0.69	0.13	0.57	18079	497	457	10.05	1	Vel2969, B=40'', w.comp, M
J094338-583317	D2D	280.461	-4.133	0.012	0.94	0.17	0.75	20082	194	123	10.27	2	B=40''
J094357-490251	C1D	274.310	3.120	0.009	0.38	0.13	0.52	7839	77	57	9.05	1	
J094407-593134	D2D	281.143	-4.830	0.016	6.56	0.47	0.84	2414	197	151	9.27	1	J0944-59, H, Z

* Detected by the overlapping region of the adjacent mosaic.

** Detected by the overlapping region of two or more adjacent mosaics.

! Detected by the overlapping region between Vela-H α and Vela-SMGPS.

Table ?? continued

Name J2000 (1)	Mosaic TXX (2)	<i>l</i> deg (3)	<i>b</i> deg (4)	<i>S</i> _{peak} Jy (5)	<i>S</i> _{int} Jy km s ⁻¹ (6)	ε_s Jy km s ⁻¹ (7)	RMS mJy beam ⁻¹ (8)	<i>V</i> _{hel} km s ⁻¹ (9)	<i>w</i> ₂₀ km s ⁻¹ (10)	<i>w</i> ₅₀ km s ⁻¹ (11)	<i>M</i> _{HI} $\log(M_{\text{HI}}/\text{M}_{\odot})$ (12)	Flag 1/2 (13)	Note (14)
J094407-573532	D2B	279.882	-3.360	0.005	0.48	0.10	0.60	10852	198	160	9.45	1	
J094427-600410	D2D	281.531	-5.214	0.012	0.33	0.09	0.73	5780	135	82	8.73	2	
J094429-491943	C1D	274.558	2.962	0.007	0.36	0.07	0.54	12181	310	216	9.42	2	
J094435-510826	C1D	275.746	1.593	0.008	0.34	0.09	0.56	4624	72	54	8.55	1	
J094440-453801	B1A	272.174	5.791	0.005	0.25	0.06	0.47	11460	114	77	9.20	1	
J094449-513036	C1D	276.013	1.335	0.011	0.55	0.14	0.63	2751	94	34	8.30	1*	
J094450-463222	B1A	272.787	5.121	0.012	1.24	0.15	0.57	11414	230	149	9.90	1	w.comp
J094451-484728	C1B	274.254	3.409	0.025	1.04	0.13	0.73	2157	54	30	8.37	1*	
J094503-611942	D2C	282.410	-6.122	0.007	1.00	0.11	0.63	11203	338	293	9.79	1	
J094511-484803	C1D	274.303	3.438	0.006	0.52	0.14	0.50	7797	176	176	9.19	1	
J094516-604149	D2C	282.017	-5.625	0.011	1.33	0.17	0.70	3104	138	97	8.79	1*	
J094523-455452	B1A	272.452	5.658	0.005	0.57	0.06	0.49	21025	275	191	10.10	1	Vel3013
J094524-480829	C1B	273.903	3.964	0.099	8.59	0.12	0.57	863	100	39	8.49	1*	J0945-48, HyA1610, H
J094531-515720	C1C	276.384	1.065	0.014	2.58	0.49	0.74	5348	254	220	9.55	1*	i, M, W
J094534-462153	B1A	272.770	5.336	0.007	0.31	0.07	0.55	7477	99	65	8.93	2	i
J094541-494655	C1D	275.000	2.742	0.008	0.35	0.07	0.60	21136	335	196	9.90	2	i?
J094605-492115	C1D	274.774	3.112	0.006	0.78	0.19	0.56	21172	270	254	10.24	1	HyA1621, w.comp? M, W
J094622-463854	B1A	273.060	5.209	0.057	15.03	0.71	0.68	2697	333	298	9.72	1	J0946-46, Vel3035, H, M, W, Z
J094630-511251	C1D	276.024	1.731	0.008	0.66	0.08	0.67	1783	157	132	8.01	1*	
J094754-462958	B1A	273.165	5.492	0.010	0.70	0.19	0.68	2745	279	223	8.40	1	
J094801-572258	D2B	280.148	-2.863	0.018	1.70	0.28	0.61	9412	163	142	9.87	1	
J094814-464417	B1A	273.363	5.345	0.022	1.48	0.27	0.78	17459	257	211	10.35	1	Vel3072, e, i
J094823-562731	D2B	279.595	-2.120	0.044	9.24	0.88	0.70	1678	255	219	9.10	1	w.comp (J094953-563235), M
J094839-452958	B1A	272.623	6.344	0.012	1.28	0.33	0.70	13438	397	353	10.06	1	Vel3084
J094843-494107	C1D	275.316	3.132	0.017	1.23	0.20	0.57	7077	111	74	9.48	1	J0948-49
J094851-514331	C1C	276.631	1.571	0.008	0.65	0.20	0.72	6959	166	123	9.19	1	M
J094901-500310	C1D	275.587	2.879	0.015	1.41	0.06	0.57	11747	171	91	9.98	1	
J094906-492208	C1D	275.161	3.415	0.023	2.82	0.37	0.64	2687	187	137	8.99	1*	J0949-49
J094916-475535	C1B	274.261	4.544	0.057	8.96	0.27	0.66	1870	183	126	9.18	1	J0949-47A, HyA1664, i, w.comp (J094924-480028), I, H, M, W, Z
J094924-480028	C1B	274.330	4.495	0.066	8.02	0.29	0.71	1979	147	95	9.18	1	J0949-47A, HyA1666, vhi{} bridge, i, w.comp (J094916-475535), H, M, W, Z
J094924-454232	B1A	272.858	6.266	0.033	2.69	0.18	0.66	5320	141	71	9.57	1	Vel3106, M, W
J094926-490829	C1B	275.058	3.625	0.011	0.72	0.15	0.64	16968	283	201	10.01	1*	HyA1669, BL, M, W
J094930-570707	D2B	280.134	-2.532	0.006	0.58	0.12	0.57	10327	364	263	9.48	1	
J094932-513903	C1C	276.665	1.696	0.009	1.67	0.30	0.67	7046	259	233	9.61	1	J0949-51
J094940-454319	B1A	272.901	6.286	0.008	0.38	0.13	0.60	16409	408	370	9.71	1	Vel3118, I, H, M
J094944-471104	C1B	273.847	5.166	0.029	5.60	0.33	0.71	5366	214	176	9.89	1	J0949-47B, Vel3119, H, M, W, Z
J094953-563235	D2B	279.808	-2.054	0.140	39.52	6.38	0.78	1761	258	226	9.77	1	J0949-56, B=45'', i, w.comps (J095106, J094823), I, H, M, W, Z
J094954-571557	D2B	280.269	-2.611	0.010	0.59	0.14	0.53	16751	246	64	9.92	1	
J094954-504421	C1D	276.133	2.439	0.010	0.62	0.15	0.60	6975	156	64	9.17	1*	i
J094959-481711	C1B	274.583	4.342	0.008	1.02	0.21	0.68	5149	373	219	9.12	1	
J095002-522411	C1C	277.203	1.165	0.031	3.09	0.14	0.78	2225	135	75	8.87	1	J0950-52, i
J095019-452602	B1A	272.805	6.580	0.010	0.66	0.17	0.80	12164	188	132	9.68	1	Vel3139, e, M, W \
J095034-494246	C1D	275.563	3.300	0.020	3.51	0.24	0.61	3776	236	189	9.38	1*	J0950-49, I, Z
J095035-500912	C1D	275.845	2.960	0.007	0.38	0.06	0.52	6946	167	152	8.96	1	
J095051-522604	C1C	277.320	1.219	0.007	0.52	0.11	0.78	8673	396	285	9.28	2	i
J095058-580953	D2B	280.950	-3.216	0.005	0.16	0.03	0.61	19191	481	180	9.46	2	
J095106-564841	D2B	280.107	-2.156	0.015	0.73	0.28	0.68	1654	99	64	7.98	1	w.comp (J094953-563235)
J095113-614527	D2C	283.254	-5.980	0.007	0.58	0.10	0.56	10209	254	118	9.47	1	
J095115-491531	C1B	275.362	3.722	0.008	0.60	0.20	0.57	12144	298	257	9.64	1	

* Detected by the overlapping region of the adjacent mosaic.

** Detected by the overlapping region of two or more adjacent mosaics.

! Detected by the overlapping region between Vela-H α and Vela-SMGPS.

Table ?? continued

Name J2000 (1)	Mosaic TXX (2)	l deg (3)	b deg (4)	S_{peak} Jy (5)	S_{int} Jy km s $^{-1}$ (6)	ε_s Jy km s $^{-1}$ (7)	RMS mJy beam $^{-1}$ (8)	V_{hel} km s $^{-1}$ (9)	w_{20} km s $^{-1}$ (10)	w_{50} km s $^{-1}$ (11)	M_{HI} $\log(M_{\text{HI}}/\text{M}_\odot)$ (12)	Flag 1/2 (13)	Note (14)
J095123-524422	C1C	277.574	1.032	0.016	0.85	0.14	0.67	6692	105	55	9.27	1	
J095131-532201	C1C	277.984	0.557	0.049	5.80	0.65	1.45	2204	151	117	9.13	1!	J0951-53, H
J095144-591607	D2D	281.724	-4.011	0.013	4.42	0.32	0.89	4398	382	350	9.62	1**	J0951-59, M, W, Z
J095146-520334	C1C	277.192	1.598	0.023	2.60	0.22	0.70	4009	153	109	9.31	1	J0951-52, Z
J095207-485929	C1B	275.303	4.018	0.007	0.51	0.15	0.55	12217	201	157	9.58	1	HyA1713
J095207-570714	D2B	280.411	-2.309	0.013	0.97	0.17	0.60	4526	119	79	8.99	1	
J095211-464300	C1B	273.874	5.792	0.010	1.73	0.20	0.58	13583	258	231	10.20	1	Vel3189
J095240-470640	C1B	274.189	5.539	0.014	1.69	0.10	0.56	1808	175	49	8.43	1	w.comp
J095244-474729	C1B	274.626	5.016	0.008	0.44	0.15	0.55	5381	106	55	8.80	1	
J095254-491618	C1B	275.580	3.881	0.011	0.83	0.17	0.61	7782	164	144	9.39	1*	w.comp (J095310-491957)
J095258-491949	C1B	275.624	3.841	0.031	3.19	0.47	0.68	2259	129	88	8.89	1*	J0953-49, H
J095300-613136	D2C	283.272	-5.667	0.025	2.98	0.24	0.76	4454	96	59	9.46	1	J0952-61, I, H, Z
J095310-491957	C1B	275.653	3.861	0.009	1.54	0.19	0.60	7795	280	208	9.66	1*	w.comp (J095254-491618)
J095321-522850	C1C	277.644	1.421	0.008	0.58	0.15	0.61	11863	245	105	9.60	1	
J095321-515411	C1C	277.284	1.872	0.022	1.34	0.11	0.67	2736	71	44	8.69	1	J0953-51
J095341-495053	C1D	276.040	3.510	0.009	0.29	0.09	0.56	4014	117	82	8.35	2	
J095347-455802	C1B	273.618	6.550	0.014	1.49	0.30	1.48	7105	349	316	9.56	2	Vel3231, M, W
J095400-520930	C1C	277.521	1.735	0.010	0.67	0.09	0.59	14024	167	140	9.81	1	
J095417-512919	C1C	277.140	2.288	0.010	0.41	0.04	0.57	2682	107	75	8.16	1	J0954-51, w.comp (J095427-513059), Z
J095418-495236	C1B	276.136	3.550	0.005	0.15	0.15	0.70	7235	200	159	8.58	2	w.comp (J095420-495422)
J095420-495422	C1B	276.158	3.530	0.007	0.38	0.15	0.70	7205	141	79	8.98	1*	HyA1744, w.comp (J095418-495236)
J095427-513059	C1C	277.176	2.281	0.006	0.49	0.09	0.60	2736	136	86	8.25	2	J0954-51, w.comp (J095417-512919)
J095435-492233	C1B	275.861	3.971	0.010	0.47	0.07	0.53	3734	99	48	8.50	1*	
J095446-494549	C1B	276.125	3.686	0.014	2.25	0.42	0.67	7108	297	256	9.74	1**	HyA1749, M, W
J095456-480421	C1B	275.093	5.028	0.007	1.37	0.25	0.57	11548	384	252	9.95	1	M
J095503-483436	C1B	275.422	4.644	0.012	1.09	0.17	0.56	17116	191	144	10.20	1	HyA1754, i, w.comp, M
J095505-573058	D2B	280.971	-2.368	0.011	0.74	0.15	0.64	10480	253	209	9.60	1	
J095510-604012	D2C	282.940	-4.835	0.011	6.05	0.36	0.76	3281	258	204	9.50	2	J0955-60, HyA1766, BL, r, H, M, W, Z
J095600-593612	D2A	282.358	-3.934	0.006	1.17	0.16	0.78	14657	253	136	10.09	2	B=40"
J095619-514119	C1C	277.511	2.326	0.009	0.57	0.08	0.53	11455	114	82	9.57	1	
J095622-584631	D2A	281.883	-3.253	0.010	0.47	0.16	0.61	2541	106	72	8.17	1*	NaN
J095630-593234	D2A	282.371	-3.847	0.005	4.22	0.11	0.76	3436	265	243	9.38	2**	J0956-59, BL, r, M, W, Z
J095632-495045	C1B	276.401	3.797	0.010	1.14	0.20	0.75	6697	230	142	9.39	1**	HyA1792, W
J095642-513436	C1C	277.489	2.450	0.010	0.35	0.08	0.56	2687	64	40	8.09	1	
J095704-512912	C1C	277.479	2.556	0.017	1.80	0.33	0.68	11378	421	305	10.06	1	i
J095710-485625	C1B	275.923	4.575	0.074	6.72	0.84	0.68	3730	95	62	9.66	1*	J0957-48, H, Z
J095750-581159	D2A	281.681	-2.681	0.044	5.72	0.61	0.70	3304	202	168	9.48	1*	J0957-58
J095757-511233	C1C	277.418	2.861	0.008	0.37	0.09	0.57	14167	173	65	9.57	2	i, w.comp
J095809-472102	C1B	275.072	5.930	0.019	2.36	0.07	0.64	3639	117	84	9.18	1	
J095837-470458	C1B	274.969	6.189	0.012	1.03	0.11	0.63	3613	157	101	8.82	1	Vel3418, I, M
J095859-501154	C1A	276.929	3.760	0.008	0.99	0.21	0.58	6648	299	256	9.33	1	HyA1835, i, w.comp, M
J095901-480721	C1B	275.661	5.408	0.006	0.38	0.06	0.52	12549	226	58	9.47	2	
J095903-490321	C1B	276.239	4.673	0.012	1.51	0.36	0.68	14156	309	277	10.17	1*	M, W
J095922-503240	C1A	277.187	3.522	0.007	0.31	0.06	0.60	8548	206	135	9.05	1	HyA1841, W
J095926-480950	C1B	275.743	5.418	0.011	0.69	0.14	0.60	6613	302	64	9.17	2	Face-on?
J095936-501102	C1A	276.998	3.832	0.015	1.69	0.26	0.62	7128	184	125	9.62	1*	HyA1849, M
J095956-512026	C1C	277.743	2.944	0.006	0.66	0.15	0.58	14076	512	469	9.81	1	
J100019-583828	D2A	282.209	-2.833	0.115	10.92	1.15	0.75	2682	185	89	9.58	1*	J1000-58A, w.comp (J100130-584224), H
J100024-495843	C1A	276.976	4.073	0.005	0.30	0.06	0.65	19050	356	269	9.73	2	

* Detected by the overlapping region of the adjacent mosaic.

** Detected by the overlapping region of two or more adjacent mosaics.

! Detected by the overlapping region between Vela-H α and Vela-SMGPS.

Table ?? continued

Name J2000 (1)	Mosaic TXX (2)	<i>l</i> deg (3)	<i>b</i> deg (4)	<i>S</i> _{peak} Jy (5)	<i>S</i> _{int} Jy km s ⁻¹ (6)	ε_s Jy km s ⁻¹ (7)	RMS mJy beam ⁻¹ (8)	<i>V</i> _{hel} km s ⁻¹ (9)	<i>w</i> ₂₀ km s ⁻¹ (10)	<i>w</i> ₅₀ km s ⁻¹ (11)	<i>M</i> _{HI} $\log(M_{\text{HI}}/\text{M}_\odot)$ (12)	Flag 1/2 (13)	Note (14)
J100036-465941	C1B	275.184	6.465	0.027	1.87	0.11	0.89	3685	91	18	9.09	1	
J100038-482637	C1A	276.073	5.317	0.006	0.46	0.12	0.56	13878	265	149	9.64	1	
J100058-535750	D1D	279.455	0.949	0.008	0.97	0.19	0.68	19845	362	341	10.28	1!	e
J100103-481251	C1B	275.989	5.542	0.006	0.39	0.09	0.53	12686	170	133	9.49	2	
J100110-573755	D2B	281.687	-1.961	0.007	0.34	0.11	0.75	12904	127	76	9.44	1	i, w.comp
J100116-534553	D1D	279.371	1.135	0.012	0.49	0.11	0.65	11931	102	52	9.53	1	
J100130-584224	D2A	282.370	-2.793	0.038	5.24	0.54	0.70	2594	207	130	9.23	1*	J1000-58B, w.comp (J100019-583828), H
J100130-601021	D2A	283.255	-3.963	0.010	0.49	0.14	0.68	17652	169	79	9.88	1	
J100152-511724	C1C	277.954	3.167	0.013	1.81	0.12	0.66	6829	243	175	9.61	1	
J100159-581829	D2A	282.180	-2.437	0.011	0.84	0.05	0.60	2594	132	92	8.44	2	
J100203-575509	D2A	281.955	-2.120	0.024	4.10	0.66	0.87	11496	288	241	10.42	1*	w.comp
J100216-510243	C1A	277.856	3.400	0.009	0.40	0.06	0.65	2702	70	27	8.15	1*	
J100219-580122	D2A	282.044	-2.182	0.011	0.48	0.10	0.65	5541	112	79	8.85	2	
J100235-572714	D2A	281.734	-1.704	0.084	11.55	1.04	1.25	2648	284	248	9.59	1*	J1002-57, M, W, Z
J100246-500355	C1A	277.332	4.232	0.005	0.38	0.09	0.50	19014	163	123	9.84	1	
J100300-492855	C1A	277.012	4.722	0.067	7.94	0.77	0.67	2401	149	101	9.34	1	J1003-49, H, Z
J100307-493715	C1A	277.110	4.622	0.006	0.23	0.05	0.49	19267	252	122	9.63	2	
J100354-590436	D2A	282.841	-2.904	0.018	1.51	0.38	0.61	2407	159	114	8.63	1	
J100356-583904	D2A	282.591	-2.559	0.081	20.96	0.90	0.75	3717	335	280	10.15	1	w.comp (J100437-583134), M, W, Z
J100414-500640	C1A	277.549	4.336	0.012	1.34	0.14	0.56	5283	204	173	9.26	1	
J100426-490323	C1A	276.946	5.204	0.007	0.24	0.10	0.56	5788	171	148	8.59	1	HyA1911
J100433-585949	D2A	282.861	-2.790	0.028	1.02	0.19	0.64	3654	60	13	8.82	2	Face-on? w.comp (J100505-590811)
J100436-490335	C1A	276.970	5.217	0.026	4.82	0.16	0.66	3393	228	179	9.43	1	HyA1916, w.comp (J100446-485936), W
J100437-583134	D2A	282.589	-2.405	0.088	22.17	1.15	0.80	3713	337	288	10.17	1	J1004-58, w.comps (one is J100356-583904), H
J100446-485936	C1A	276.953	5.287	0.012	0.36	0.04	0.53	3438	43	27	8.31	2	w.comp (J100436-490335)
J100447-484426	C1A	276.803	5.491	0.006	1.22	0.17	0.67	6725	235	181	9.43	1	HyA1919, M, W
J100452-501212	C1A	277.686	4.323	0.012	1.19	0.10	0.58	6816	128	108	9.43	1	
J100502-533052	D1D	279.670	1.669	0.012	0.97	0.15	0.56	12219	144	90	9.85	1	Face-on? i
J100507-590752	D2A	282.999	-2.855	0.008	0.32	0.09	0.59	3650	206	32	8.31	2	w.comp (J100433-585949)
J100510-583817	D2A	282.712	-2.454	0.018	1.01	0.20	0.76	11674	148	93	9.83	1	
J100526-514220	C1C	278.649	3.164	0.010	0.85	0.17	0.71	7311	236	190	9.34	2	
J100527-581826	D2A	282.546	-2.165	0.016	1.01	0.23	0.73	2672	110	71	8.54	1	
J100528-525125	D1D	279.333	2.238	0.010	0.87	0.17	0.59	7506	207	156	9.38	1	i
J100542-480255	C1A	276.514	6.139	0.011	2.48	0.15	0.66	4018	294	266	9.29	1	
J100556-504525	C1A	278.152	3.977	0.009	0.58	0.12	0.67	8532	346	302	9.31	1	w.comp
J100606-503647	C1A	278.088	4.108	0.020	5.99	0.44	0.67	5320	340	300	9.92	1	J1006-50B, HyA1939, M, W, Z
J100616-492835	C1A	277.437	5.042	0.070	10.19	0.43	0.70	2397	163	131	9.45	1	J1006-49, H, Z
J100621-525428	D1D	279.471	2.275	0.008	0.34	0.07	0.61	15838	277	176	9.62	1	i, M, W
J100621-510431	C1A	278.392	3.758	0.006	0.64	0.19	0.65	14722	158	84	9.84	2	
J100629-501436	C1A	277.919	4.443	0.017	4.12	0.46	0.62	5283	296	263	9.75	1	J1006-50A, HyA1945, M, W, Z
J100642-500004	C1A	277.805	4.660	0.002	2.96	0.61	0.65	6741	299	149	9.82	1	J1006-50C
J100643-494436	C1A	277.655	4.870	0.010	0.82	0.15	0.59	21184	305	135	10.26	1	HyA1950, M, W
J100644-500822	C1A	277.889	4.550	0.011	0.73	0.21	0.57	6834	111	64	9.22	1	HyA1951, M, W
J100646-474148	C1A	276.449	6.528	0.010	1.47	0.16	0.93	4022	339	306	9.06	1	Vel3666, M
J100647-520619	D1D	279.053	2.964	0.041	2.10	0.12	0.67	6728	65	19	9.67	1	J1006-52, face-on
J100714-532653	D1D	279.895	1.915	0.008	0.44	0.10	0.55	14103	246	54	9.63	1	
J100725-494107	C1A	277.713	4.983	0.017	0.67	0.07	0.53	7004	59	9	9.21	1	
J100736-591142	D2A	283.294	-2.720	0.010	0.45	0.12	0.62	6265	145	99	8.94	1	w.comp (J100803-591855)
J100737-545527	D1D	280.803	0.750	0.015	0.92	0.32	0.97	9044	383	239	9.56	1!	e, M, W

* Detected by the overlapping region of the adjacent mosaic.

** Detected by the overlapping region of two or more adjacent mosaics.

! Detected by the overlapping region between Vela-H I and Vela-SMGPS.

Table ?? continued

Name J2000 (1)	Mosaic TXX (2)	l deg (3)	b deg (4)	S_{peak} Jy (5)	S_{int} Jy km s $^{-1}$ (6)	ε_s Jy km s $^{-1}$ (7)	RMS mJy beam $^{-1}$ (8)	V_{hel} km s $^{-1}$ (9)	w_{20} km s $^{-1}$ (10)	w_{50} km s $^{-1}$ (11)	M_{HI} $\log(M_{\text{HI}}/\text{M}_\odot)$ (12)	Flag 1/2 (13)	Note (14)
J100803-591855	D2A	283.412	-2.783	0.065	7.70	0.64	0.74	6252	190	143	10.16	1	J1007-59, w.comp (J100734-591147)
J100809-513236	D1B	278.895	3.543	0.010	0.82	0.15	0.76	8648	214	199	9.47	1*	
J100815-491249	C1A	277.545	5.445	0.007	0.65	0.12	0.64	18672	427	394	10.05	2	HyA1977, I, M, W
J100821-483759	C1A	277.217	5.925	0.012	1.40	0.10	0.57	2751	157	108	8.71	1	HyA1978, W
J100856-540828	D1D	280.504	1.499	0.022	1.77	0.36	0.72	4920	219	153	9.32	1	i
J100915-494323	C1A	277.975	5.125	0.012	1.31	0.41	0.60	6792	265	165	9.47	1	
J100920-500309	C1A	278.178	4.864	0.007	0.53	0.11	0.51	18988	145	64	9.97	1	HyA1998, W
J100925-485900	C1A	277.566	5.743	0.011	0.35	0.09	0.57	5659	74	26	8.74	2	
J100938-505610	C1A	278.732	4.173	0.009	1.15	0.26	0.73	11815	315	259	9.90	1	HyA2007, M, W
J100940-510431	D1B	278.817	4.062	0.024	3.77	0.23	0.98	2837	183	130	9.17	1	J1009-51, e
J101005-524202	D1D	279.810	2.773	0.026	3.19	0.90	0.69	7388	317	266	9.93	1	HyA2014, M, W
J101012-602256	D2A	284.250	-3.497	0.015	0.58	0.12	1.00	15824	200	135	9.86	1	e
J101026-544128	D1D	281.000	1.175	0.015	1.04	0.14	0.63	3596	121	105	8.81	1	
J101027-521222	D1D	279.570	3.209	0.006	0.46	0.10	0.53	12267	310	210	9.54	1	i
J101028-601135	D2A	284.170	-3.322	0.010	1.00	0.26	0.91	6278	268	252	9.28	2	e, i, M, W
J101031-490436	C1A	277.768	5.771	0.019	1.39	0.10	0.57	5368	109	79	9.29	1	
J101049-592041	D2A	283.716	-2.604	0.029	1.22	0.14	0.71	3281	102	41	8.80	2	Face-on? w.comp (J101136-591511)
J101106-490818	C1A	277.882	5.776	0.010	0.97	0.26	0.59	5782	219	162	9.20	1	i
J101122-492600	C1A	278.090	5.560	0.006	0.58	0.17	0.54	14098	221	197	9.76	2	
J101133-492752	C1A	278.132	5.552	0.011	0.51	0.13	0.53	5340	178	117	8.85	1	HyA2041
J101136-591511	D2A	283.746	-2.471	0.013	0.53	0.18	0.68	3294	117	50	8.45	1	w.comp (J101049-592041)
J101146-525950	D1D	280.188	2.675	0.011	0.58	0.23	0.61	2769	133	89	8.33	1	
J101155-514244	D1B	279.472	3.743	0.012	0.82	0.08	0.61	21700	92	42	10.28	2	Face-on?
J101207-512803	D1B	279.356	3.961	0.014	1.41	0.16	0.65	5272	143	107	9.28	1*	J1012-51, w.comp (J101231-513221)
J101208-551907	D1C	281.559	0.801	0.011	0.45	0.08	0.73	2663	111	74	8.19	1!	e
J101210-540416	D1D	280.852	1.828	0.017	1.12	0.12	0.61	7347	143	85	9.47	1	
J101231-513221	D1B	279.450	3.939	0.008	0.34	0.08	0.59	5252	92	40	8.66	1	w.comp (J101207-512803)
J101231-513717	D1B	279.497	3.871	0.005	0.45	0.05	0.58	8554	231	184	9.21	1	HyA2064, M
J101249-544917	D1D	281.356	1.265	0.011	1.78	0.36	0.67	8858	377	324	9.83	1*	i, M
J101250-591844	D2A	283.909	-2.431	0.021	2.89	0.42	0.91	5530	215	200	9.63	1	
J101300-531541	D1D	280.490	2.563	0.010	1.78	0.41	0.58	12192	433	389	10.11	1	
J101321-522704	D1D	280.075	3.261	0.028	1.81	0.23	0.66	8655	113	69	9.82	1*	J1013-52A, HyA2091, w.comp (J101324-523120)
J101324-523120	D1D	280.121	3.207	0.013	3.20	0.62	0.67	8584	337	325	10.06	1	HyA2095, w.comp (J101321-522704), I, M, W, Z
J101325-523117	D1B	280.122	3.208	0.012	1.09	0.18	1.08	8546	287	204	9.59	1	J0913-52A? HyA2095, e, i, w.comp (J101321-522704), I, M, W, Z
J101329-495259	C1A	278.630	5.387	0.010	0.66	0.11	0.66	2818	122	32	8.41	1	
J101331-523959	D1D	280.218	3.098	0.008	0.47	0.10	0.54	12082	204	95	9.53	1	w.comp (J101407-524456)
J101333-533454	D1D	280.740	2.346	0.008	0.47	0.10	0.66	19805	131	78	9.96	1	Face-on?
J101342-500318	C1A	278.756	5.265	0.010	1.00	0.22	0.67	6734	200	147	9.34	1	HyA2103, M, W
J101346-521708	D1D	280.032	3.433	0.046	14.82	1.06	0.76	2732	272	250	9.73	1*	J1013-52B, HyA2109, I, H, M, W, Z
J101347-504608	D1B	279.174	4.685	0.007	0.51	0.13	0.63	8760	249	58	9.28	1	
J101351-494018	C1A	278.557	5.594	0.016	0.65	0.13	0.77	5741	224	142	9.01	1	HyA2111, M, W
J101359-514544	D1B	279.764	3.884	0.011	2.11	0.12	0.60	2964	240	191	8.95	1*	HyA2114, M, W
J101405-524443	D1D	280.332	3.081	0.008	0.50	0.10	0.64	12070	132	105	9.55	1	w.comp (J101331-523959)
J101407-494026	C1A	278.594	5.616	0.013	0.68	0.17	0.64	7364	68	51	9.25	1	HyA2119, W
J101424-490836	C1A	278.330	6.080	0.017	3.36	0.57	0.72	2730	332	147	9.08	2	B=90°, BL
J101426-510412	D1B	279.430	4.495	0.010	0.84	0.16	0.62	11676	349	34	9.75	1	HyA2127, M, W
J101436-530539	D1D	280.595	2.838	0.011	1.79	0.22	0.59	12228	254	222	10.12	1	i
J101453-545418	D1C	281.648	1.363	0.033	2.51	0.31	0.70	1230	136	83	8.26	1*	J1014-54
J101502-531031	D1D	280.694	2.807	0.012	0.58	0.10	0.51	18819	110	35	10.01	1	Face-on?

* Detected by the overlapping region of the adjacent mosaic.

** Detected by the overlapping region of two or more adjacent mosaics.

! Detected by the overlapping region between Vela-H α and Vela-SMGPS.

Table ?? continued

Name J2000 (1)	Mosaic TXX (2)	l deg (3)	b deg (4)	S_{peak} Jy (5)	S_{int} Jy km s $^{-1}$ (6)	ε_s Jy km s $^{-1}$ (7)	RMS mJy beam $^{-1}$ (8)	V_{hel} km s $^{-1}$ (9)	w_{20} km s $^{-1}$ (10)	w_{50} km s $^{-1}$ (11)	M_{HI} $\log(M_{\text{HI}}/\text{M}_{\odot})$ (12)	Flag 1/2 (13)	Note (14)
J101549-523950	D1D	280.504	3.296	0.008	0.35	0.07	0.65	18753	317	242	9.78	1	BL
J101606-521023	D1D	280.265	3.727	0.007	0.38	0.08	0.75	14086	170	122	9.57	1*	
J101645-533057	D1D	281.098	2.668	0.007	0.80	0.22	0.57	10017	306	261	9.59	2	HyA2198, M, W
J101646-523459	D1D	280.579	3.444	0.006	0.40	0.07	0.58	19406	443	323	9.88	2	M, W
J101650-545827	D1C	281.919	1.462	0.010	0.26	0.08	0.60	6461	179	121	8.72	2	i
J101655-485241	C1A	278.524	6.532	0.034	27.93	0.67	1.19	2738	414	366	10.00	1	HyA2200, B=60'', I, H, M, W, Z
J101706-552227	D1C	282.174	1.152	0.013	1.56	0.34	0.69	14490	341	281	10.21	1	
J101714-493903	D1B	279.001	5.920	0.009	0.72	0.12	0.65	12810	206	103	9.76	1	e
J101721-525702	D1D	280.858	3.188	0.011	0.59	0.12	0.62	6324	105	44	9.06	1	
J101753-521505	D1B	280.536	3.814	0.009	1.45	0.11	0.63	2996	213	179	8.80	1*	
J101756-534932	D1D	281.415	2.507	0.006	0.28	0.06	0.52	18357	208	170	9.67	2	
J101810-524517	D1D	280.851	3.419	0.007	0.40	0.07	0.61	12150	162	127	9.47	2	
J101822-515505	D1B	280.413	4.133	0.010	1.65	0.17	0.62	8289	478	416	9.74	2	NaN
J101831-510332	D1B	279.957	4.862	0.022	5.13	0.29	0.75	4068	245	214	9.61	1	J1018-51, H, Z
J101848-500949	D1B	279.497	5.633	0.010	0.62	0.07	0.55	6827	79	77	9.14	1	
J101857-495405	D1B	279.372	5.865	0.009	0.57	0.16	0.54	22369	359	313	10.15	1	HyA2277, M, W
J101857-531016	D1D	281.181	3.137	0.007	0.41	0.08	0.52	20020	204	159	9.91	2	
J101917-531048	D1D	281.226	3.156	0.007	0.41	0.11	0.63	4096	126	103	8.52	1*	
J101924-545130	D1C	282.163	1.763	0.008	0.26	0.07	0.54	10078	69	51	9.11	1	
J101939-560131	D1C	282.832	0.806	0.014	0.84	0.17	0.93	8911	287	221	9.51	1!	e, i
J101939-513339	D1B	280.383	4.541	0.004	0.37	0.12	0.59	17702	303	230	9.76	2	HyA2308, M, W
J101941-540331	D1C	281.759	2.454	0.028	2.53	0.41	0.63	6208	131	85	9.67	1*	J1019-54, M, W, Z
J101949-495554	D1B	279.506	5.916	0.007	0.88	0.21	0.57	12560	251	104	9.83	1	HyA2316, M, W
J101955-501310	D1B	279.679	5.685	0.011	0.50	0.10	0.65	8546	405	268	9.25	1	HyA2320, i, w.comp, M, W
J102032-533149	D1C	281.575	2.965	0.008	0.60	0.12	0.54	10173	163	141	9.49	1	
J102052-495218	D1B	279.616	6.060	0.007	1.24	0.34	0.65	19842	369	347	10.39	1	
J102132-534039	D1C	281.780	2.923	0.014	0.72	0.15	0.60	6512	105	59	9.17	1	
J102209-541413	D1C	282.159	2.501	0.011	0.52	0.17	0.58	10439	101	44	9.44	1	i
J102232-533111	D1C	281.819	3.135	0.006	0.28	0.05	0.48	22399	136	50	9.84	2	w_{20} unc.
J102250-503849	D1B	280.305	5.580	0.011	0.64	0.09	0.56	21184	119	79	10.15	1	
J102311-533051	D1C	281.898	3.192	0.005	0.30	0.04	0.57	6001	262	80	8.72	2	HyA2431, M, W
J102321-495927	D1B	280.017	6.176	0.005	0.50	0.17	0.55	12720	218	195	9.60	1	HyA2433
J102325-501118	D1B	280.133	6.015	0.012	1.09	0.15	0.69	7362	161	120	9.46	1	HyA2435
J102344-513156	D1B	280.901	4.909	0.010	1.15	0.15	0.65	7966	332	24	9.55	2	HyA2443, M, W
J102347-535523	D1C	282.193	2.895	0.026	5.98	1.36	0.67	6175	436	395	10.04	1	J1023-53, M, W, Z
J102410-515910	D1B	281.204	4.563	0.017	2.89	0.53	0.78	9232	284	225	10.08	1*	J1024-52
J102415-543922	D1C	282.643	2.312	0.009	0.31	0.06	0.57	1111	108	76	7.27	1	w.comp (J102445-544757)
J102424-533526	D1C	282.091	3.224	0.006	0.36	0.02	0.56	6599	261	156	8.88	1	M, W
J102425-502647	D1B	280.409	5.884	0.004	0.19	0.04	0.62	20935	215	163	9.62	2	B=35''
J102445-544757	D1C	282.779	2.228	0.110	14.65	0.27	0.74	1084	150	119	8.92	1	J1024-54, HyA2469, w.comp (J102445-544757), H, W, Z
J102450-502301	D1B	280.432	5.973	0.007	0.57	0.12	0.67	7526	98	55	9.20	2	B=40''
J102454-535204	D1C	282.303	3.030	0.006	0.30	0.11	0.52	5626	78	56	8.67	1	
J102510-533120	D1C	282.152	3.343	0.007	0.93	0.19	0.63	6421	237	207	9.27	2	i, I, M, W
J102525-550555	D1C	283.020	2.026	0.033	6.63	0.47	0.66	6984	383	345	10.20	1	
J102540-535121	D1C	282.391	3.099	0.015	1.33	0.28	0.58	7035	168	89	9.51	1	i
J102552-513243	D1B	281.190	5.075	0.011	1.69	0.18	0.68	7750	213	198	9.69	1*	HyA2502, i, H, M, W
J102559-535202	D1C	282.437	3.114	0.062	5.69	0.37	0.65	6792	128	74	10.11	1	J1026-53, face-on, H
J102606-543417	D1C	282.824	2.525	0.007	0.38	0.05	0.48	11813	187	138	9.42	1	
J102609-543532	D1C	282.841	2.511	0.015	2.04	0.41	0.63	6362	270	218	9.60	1	i

* Detected by the overlapping region of the adjacent mosaic.

** Detected by the overlapping region of two or more adjacent mosaics.

! Detected by the overlapping region between Vela-H i and Vela-SMGPS.

Table ?? continued

Name J2000 (1)	Mosaic TXX (2)	<i>l</i> deg (3)	<i>b</i> deg (4)	<i>S</i> _{peak} Jy (5)	<i>S</i> _{int} Jy km s ⁻¹ (6)	ε_s Jy km s ⁻¹ (7)	RMS mJy beam ⁻¹ (8)	<i>V</i> _{hel} km s ⁻¹ (9)	<i>w</i> ₂₀ km s ⁻¹ (10)	<i>w</i> ₅₀ km s ⁻¹ (11)	<i>M</i> _{HI} $\log(M_{\text{HI}}/\text{M}_{\odot})$ (12)	Flag 1/2 (13)	Note (14)
J102611-534650	D1C	282.416	3.203	0.014	1.11	0.26	0.61	7207	137	106	9.45	1	HyA2512, M, W, Z
J102630-523510	D1A	281.825	4.243	0.004	0.50	0.14	0.67	6340	116	79	8.99	1	
J102632-503259	D1B	280.750	5.975	0.017	0.71	0.15	0.82	7183	190	21	9.25	2	Face-on?
J102638-512334	D1A	281.212	5.268	0.010	0.75	0.07	0.72	7811	128	72	9.35	1*	
J102640-510355	D1B	281.042	5.548	0.015	2.23	0.11	0.64	3001	203	168	8.99	1	HyA2521, W
J102705-512248	D1A	281.265	5.316	0.006	0.31	0.11	0.70	14389	381	346	9.50	1	B=40'', i
J102721-542945	D1C	282.939	2.685	0.014	1.49	0.28	0.60	12157	245	192	10.04	1	i
J102723-502836	D1B	280.826	6.108	0.008	0.39	0.08	0.72	15979	215	151	9.70	2	HyA2549, B=35'', M, W
J102815-503103	D1B	280.967	6.146	0.016	2.45	0.30	0.72	6019	338	283	9.63	1	HyA2579, i, M, W
J102820-512220	D1B	281.426	5.424	0.012	0.62	0.15	0.61	7604	79	66	9.24	1	
J102825-504757	D1B	281.137	5.920	0.017	1.83	0.15	0.64	7121	130	84	9.65	1	w.comp (J102825-504127)
J102825-533634	D1A	282.609	3.523	0.050	4.94	0.41	0.69	2725	123	78	9.25	1*	J1028-53, Z
J102825-504121	D1B	281.080	6.014	0.010	1.31	0.29	0.62	6980	405	345	9.49	1	HyA2585, w.comp (J102825-504757), I, M, W
J102840-552911	D1C	283.618	1.939	0.007	0.40	0.12	0.55	15105	129	88	9.66	1	
J102844-505816	D1B	281.270	5.799	0.013	5.23	0.25	0.66	6083	453	405	9.97	1*	HyA2595, I, M, W
J102859-502533	D1B	281.018	6.285	0.015	3.30	0.17	0.83	6752	362	338	9.86	1	HyA2602, M
J103031-532941	D1C	282.817	3.782	0.007	0.56	0.10	0.65	6549	164	116	9.07	1	B=42'', e
J103042-524148	D1A	282.430	4.481	0.004	0.38	0.07	0.58	12785	226	162	9.48	2	HyA2641, M, W
J103124-512240	D1A	281.841	5.667	0.009	2.34	0.30	0.69	6371	289	249	9.67	1	HyA2659, BL, i, M, W
J103219-504230	D1A	281.622	6.317	0.007	0.78	0.12	0.68	6252	161	138	9.17	1*	HyA2687, e, M, W
J103322-523534	D1A	282.724	4.776	0.007	0.24	0.05	0.81	9842	108	61	9.06	1	BL
J103329-524545	D1A	282.826	4.639	0.005	0.39	0.12	0.58	13295	180	126	9.54	2	i
J103403-534306	D1A	283.384	3.857	0.021	1.32	0.22	0.71	6474	113	72	9.43	1*	e
J103423-542813	D1C	283.804	3.231	0.006	0.30	0.05	0.54	12936	252	205	9.40	1	
J103444-535837	D1C	283.601	3.684	0.010	0.72	0.19	0.69	6366	113	90	9.15	1*	e, i, w.comp
J103520-535641	D1C	283.662	3.756	0.014	1.41	0.23	0.79	8264	169	135	9.67	1*	e, i
J103553-540615	D1C	283.810	3.657	0.015	1.99	0.40	0.88	6283	450	411	9.58	1*	J1035-54, HyA2740, e, i, w.comp? I, M, W, Z
J103703-530108	D1A	283.423	4.686	0.009	0.76	0.15	0.68	15194	401	196	9.94	1	
J103844-524728	D1A	283.531	5.009	0.008	0.40	0.10	0.61	6085	166	57	8.85	2	
J103925-525452	D1A	283.683	4.952	0.015	1.04	0.10	0.64	17630	215	21	10.21	1	
J103931-520525	D1A	283.294	5.679	0.008	0.67	0.18	0.63	12333	320	279	9.70	1	i, w.comp
J104004-524010	D1A	283.649	5.213	0.006	0.39	0.07	0.58	9848	129	127	9.26	1	
J104109-521004	D1A	283.550	5.732	0.010	0.54	0.11	0.61	15088	204	171	9.78	2	BL, i?
J104131-513250	D1A	283.302	6.304	0.005	0.49	0.05	0.62	14901	245	181	9.73	2	

This paper has been typeset from a $\text{\TeX}/\text{\LaTeX}$ file prepared by the author.